LIVER FIBROSIS SURFACE ASSESSMENT BASED ON NON-LINEAR OPTICAL MICROSCOPY

HE YUTING

(B.S. WUHAN UNIVERSITY)

A THESIS SUBMITTED

FOR THE DEGREE OF DOCTOR OF PHILOSOPHY

IN COMPUTATIONAL AND SYSTEMS BIOLOGY

(CSB)

SINGAPORE-MIT ALLIANCE

NATIONAL UNIVERSITY OF SINGAPORE

2010

ACKNOWLEDGEMENT

The four years of Ph.D study has been the most rewarding and memorable time in my life. Living and studying in this dynamic environment of Singapore, I am exposed to all kinds of great opportunities, both academically and in general. The scientific interaction with MIT and the intense yet pleasant 5 months study in MIT also opened up my mind for future opportunities. I truly thank SMA for offering us this unique experience for the Ph.D study. Overseas for four years, I couldn't spend as much time as I should with my beloved parents and grandparents. However, they are strongly supportive of my study in Singapore, and always a phone call away whenever I need them. I thank them for all their support and encouragements during all the years. I am grateful to my supervisors, Prof. Hanry Yu, and Prof. Peter So for their patience and guidance during my Ph.D study. Prof. Hanry Yu has greatly shaped my scientific way of thinking, and has offered various precious advices during the years that would benefit me greatly in my future career. Many thanks to all my colleagues in Hanry Yu's group. It has been great fun to work with everyone and to learn and get support from each member of the group. I truthfully thank Dr. Lou Yan-Ru for being especially patient teaching me all the biological assays, and great encouragement while I was in difficulty situations with my research. I thank Dr. Xia Wuzheng, Dr. Tuo Xiaoye, Dr. Xiao guangfa for their surgical expertise and tremendous help in my animal model work. I own my thanks to Mr. Xu Shuoyu and Mr. Alvin Kang Chiang Huen for their support and immediate response whenever I encounter any technical problems during my research. I thank my seniors and friends in the lab Dr. Xia Lei, Dr. Zhang Chi, Dr. Zhang Shufang, Dr. Ong Siew Min for their guidance and support for

my study. I thank all my friends from SMA family Ms. Zhang Wei, Ms. Peng Qiwen, Ms. Merlin Veronika, Mr. Naveen Kumar Balla for all the help and support for my study and research. And Last but not least, I want to thank SMA, NUS, IBN and BMRC for generous financial supports and SMA for my scholarship.

Table of Contents

SUMMARY

This thesis documented the study of liver fibrosis using non-linear optics microscopy. Rat fibrosis models were established as an animal platform, and tissue level imaging was applied. To use non-linear optics methods to study liver fibrosis, images of unstained liver tissues taken were compared to conventional histological stained slice tissues. Four morphological features from digitized Second Harmonic Generation (SHG) / Two Photon Excitation Fluorescence (TPEF) images were extracted from tissues, and a standardized quantification system in liver fibrosis assessment was developed based on those features. After comparing with the conventional 'gold standard' histopathological scoring system, we demonstrated the feasibility of SHG/TPEF microscopes in monitoring liver fibrosis progression by the quantitative assessment we developed. The quantitative and standardization nature of the SHG/TPEF imaging modalities allows for future application in diagnosis and prognostication of disease complications and to assist biopsy reading by minimizing the intra- and interobserver discrepancies through standardized features quantification for staging. The non-staining requirement of such imaging methods also gave the potential for *in vivo* fibrosis assessment given its ability to extract cellular level features.

To achieve the goal of *in vivo* fibrosis assessment, we focused on the liver surface, where the imaging scanning would be performed. Due to the limited intrinsic penetration depth of SHG/TPEF imaging modalities in opaque liver tissue, liver surface features were studies and compared to the general features we extracted in interior liver. We discovered a strong correlation between liver

fibrosis progression on the anterior surface and the interior based on quantitative analysis of morphological features in both regions. By comparing with the conventional histopathological scoring system, we demonstrated the feasibility of monitoring liver fibrosis progression on the anterior liver surface. A uniform distribution of quantitative liver fibrotic features, such as total collagen distribution, bile duct proliferation and collagen in bile duct areas, was also discovered across two main lobes of the anterior liver surface, which gave us confidence to quantitatively monitor the progress of liver fibrosis on different lobe surfaces.

Following the discovery that fibrosis distribution on liver surface is similar to that of the liver interior, application of such discovery was explored in live imaging. An intravital imaging-based liver chamber was designed and developed for the purpose of live rat imaging, and has been applied on both normal and fibrotic rats for *in vivo* liver fibrosis monitoring. A toxicity induced liver fibrosis model was developed as opposed to the previously used Bile Duct Ligation model, for the ease of chamber installation and imaging quality control. In live imaging of rat liver through a window chamber, we discovered similar fibrosis features to those we observed in both transmission and reflective tissue imaging, including increase of capsule collagen distribution on liver surface, increase of sub-capsule fibril collagen deposition within the liver tissue and disruption of tissue structure with the fibrosis progression. With these features present in animal fibrosis models and the ability of detection of features in live imaging, we are currently able to monitor fibrosis based on this window animal model.

LIST OF TABLES

LIST OF FIGURES

LIST OF SYMBOLS AND ABBREVATIONS

extracellular matrix	ECM
Second harmonic generation	SHG
two-photon excited fluorescence	TPEF
Hepatitis C Virus	HCV
nonalcoholic steatohepatitis	NASH
Primary Biliary Cirrhosis	PBC
hepatic stellate cells	HSC
Epithelial-Mesenchymal Transition	ETM
Magnetic resonance elastography	MRE
Magnetic resonance spectroscopy	MRS
Bile Duct Ligation	BDL
Thioacetamide	TAA
Two-dimensional	2D
Three-dimensional	3D
Mesenchymal stem cells	MSCs
Biliary atresia	BA
N-ethyl-N-nitrosourea	ENU
Targeting Induced Local Lesions in Genomes	TILLING
Hepatocyte nuclear factor	HNF
Hepatocyte Growth Factor	HGF
Biliary epithelial cells	BECs
Polyethylene terephthalate	PET
Magnetic Resonance Imaging	MRI
Apparent Diffusion Coefficient	ADCs
endoplasmic reticulum	ER

Chapter 1 Introduction

Liver fibrosis is a wound healing process occurring in response to almost all causes of chronic liver injury, and consists of an accumulation of fibrillar extracellular matrix (ECM) components [1, 2]. This process may lead to cirrhosis with its consequences of portal hypertension, hepatocellular carcinoma, and liver failure. The diagnosis and quantification of liver fibrosis, therefore, is critical for the treatment of the disease. Currently, percutaneous liver biopsy still represents the gold standard for the diagnosis and assessment of liver fibrosis [3]. However, besides the potential complications following liver biopsy, there are inherent drawbacks, such as invasive nature of the procedure, sampling error and inter- and intraobserver variability in the interpretation of the needle biopsy results [4, 5]. Intrinsic limited sensitivity and operator-dependent variations also existed in the post procession of the extracted liver tissues. Meanwhile, histological examination does not predict disease progression [6].

Over recent years, Second harmonic generation (SHG) has emerged as a powerful tool for imaging structural proteins in tissues [7]. Fibrillar collagen, being highly noncentrosymmetric, possesses a tremendous nonlinear susceptibility, therefore, SHG microscopy of collagen provide an invaluable tool for imaging tissue structure with submicron resolution [8]. Since its introduction by Denk et. al. [9], two-photon excited fluorescence (TPEF) has been widely used for imaging structure and dynamic interactions in biological tissues [10, 11]. Since the major determinant of progressive fibrosis is the failure to degrade the increased fibril-forming scar matrix, especially the type I collagen

[12], the principal collagen in fibrotic liver, SHG microscopy can be applied for targeting type I collagen as a metric to indicate liver fibrosis. Combined SHG/TPEF images permit the location of SHG signals from collagen fibers within the liver, whose morphology is revealed by endogenous TPEF signals. Simultaneous three-dimensional visualization of collagen can be achieved and can be used to quantify fibrosis in fibrotic liver [13].

Based on these findings, in this thesis project, we aim to develop a fully automated liver fibrosis assessment system to quantify liver fibrosis based on the information extracted from images taken from unstained tissue slices. Second Harmonic Generation and Two Photon Excitation Fluorescence imaging modalities were employed to acquire those images, and computer-based imaging processing methods were explored for feature recognition and extraction. The assessment system was also compared with well-recognized histopathological scoring systems to reveal its validity and accuracy. A complete and extensive animal model study was presented in this thesis to demonstrate the ability of the SHG/TPEF imaging modality to extract useful information for accurate fibrosis assessment.

With the potential of SHG/TPEF imaging modality's intrinsic sectioning and ability to extract tissue information from unstained tissue samples, we later proposed using this imaging modality for high-resolution fibrosis scanning on intact tissue. Due to the opaque nature of the liver organ, such scanning was restricted to the surface of the organ. Therefore, the relationship between the liver surface and the whole liver organ was studied to explore the possibility of assessing liver fibrosis based on liver surface information extracted. As the

qualitative indication of capsule thickening in rats was suggested before [14], the features of both capsule and sub-capsule regions were investigated. Quantitative comparison between these features in liver surface and liver interior were shown and further compared with histopathological findings.

With the discovery of strong correlation between fibrosis distribution on liver surface and in liver interior in a later chapter, we envisioned surface quantification of liver fibrosis progression through laparoscopy application. To test the feasibility of such approach on animal models without the currently available SHG/TPEF laparoscopy device, we proposed establishing an animal model for *in vivo* imaging through installing an intravital window chamber on the rat abdomen. This lead to the discovery and refinement of materials and designs for the intravital chamber device as well as the imaging stage that accommodates the live animal imaging on the current microscope setup. Live imaging of rat liver was successfully performed on such a stage. A different animal model was also explored in this study to adapt to the intravital window chamber for better imaging quality.

To provide a background and rationale for the thesis studies, a literature review is presented in the following chapter. The cause of liver fibrosis and its pathogenesis is briefly introduced, followed by the current diagnostic methods and problems in diagnosing of the disease. Imaging methods that would be employed in the thesis studies are also described and explained in the chapter. The chapter ends with the potential application of the imaging modalities in the biological study, especially in the liver fibrosis investigation, which leads to the three specific aims of this thesis, presented in Chapter 3. Chapter 4 de-

scribed the establishment of a quantification system for liver fibrosis that based on the imaging modalities, which lays out the foundation for future liver fibrosis surface assessment in Chapter 5 and the intravital window model for live imaging and live fibrosis surface exploration in Chapter 6. Chapter 7 concludes all the major findings of the studies and the implications. Chapter 8 ends the thesis with recommendation for future studies.

Chapter 2 Background and Significance

This chapter presents background information that defines the rationale for the thesis research. Section 2.1 is the brief review of liver fibrosis disease, which we break down into three parts. Part 1 is the introduction of liver as a functional organ and the disease in liver that we are going to focus on studying, which is liver fibrosis. Part 2 continues on the detailed description of the cause and pathogenesis of liver fibrosis, which leads to part 3, the diagnosis and the current problems we face in diagnosing liver fibrosis. To help solving the diagnostic difficulties in liver fibrosis, we introduce imaging based methods, which we describe in detail in Section 2.2. This section is also broken down into two parts, with first part describing the theory and advantages of SHG and TPEF two imaging modalities we are going to use, and second part focusing on the application of these two imaging modalities in biological studies.

2.1 Pathogenesis and diagnosis of liver fibrosis

2.1.1 Liver and liver fibrosis

Liver is one of the largest organs in the adult body and mainly consists of two lobes. It is a vital organ with a wide range of functions, such as detoxification, protein synthesis, and production of biochemicals necessary for digestion. This organ plays a vital role in metabolism and has a number of functions in the body, including glycogen storage, decomposition of red blood cells, plasma protein synthesis, hormone production, and detoxification. It produces bile, an alkaline compound which aids in digestion. It also performs and regulates a wide variety of high-volume biochemical reactions requiring highly specialized tissues, including the synthesis and breakdown of small and complex molecules, which are necessary for normal vital functions [15].

To look at the architecture of the liver, it lies in the abdominal cavity, in contact with diaphragm. The mass is divided into several lobes, of which the number and size vary among species. The image below (Figure 1(a)) is of a liver from a fibrotic rat, and shows that aspect of the liver that faces the contents of the abdominal cavity. Liver is covered with a connective tissue capsule that branches and extends throughout the substance of the liver. The connective tissue tree provides a scaffolding of support and helps with the blood vessels, lymphatic vessels and bile ducts traverse the liver. The sheets of connective tissue also divide the parenchyma of the liver into very small units called lobules (Figure 1(b)), the structural unit of the liver. It consists of roughly hexagonal arrangement of plates of hepatocytes radiating outward

from a central vein in the center. Portal triads are distributed at the vertices of the lobule [16].

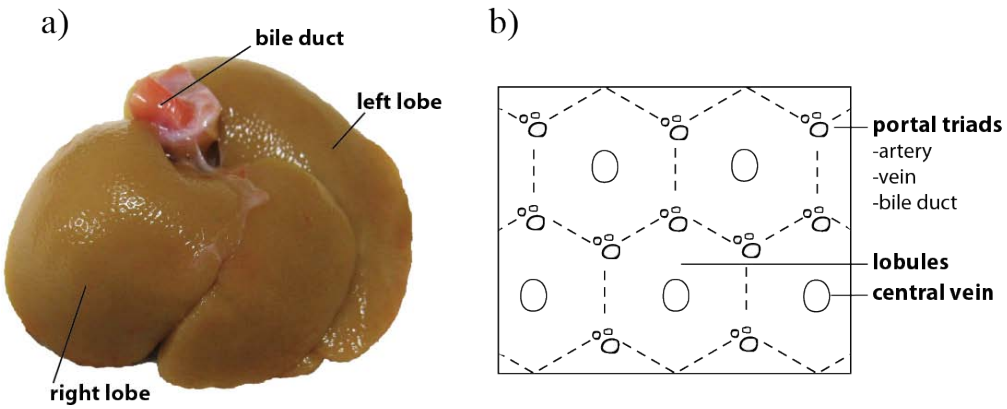

Figure 1. Liver anatomy and the structure of the hepatic parenchyma. (a) Formalin fixed liver from a fibrotic rat. (b) Tissue structure of standard liver tissue, with lobules as the structure unit of the liver.

Liver fibrosis is the growth of scar tissue due to infection, inflammation, injury, or even healing. It results from chronic damage to the liver in conjunction with accumulated deposition of ECM proteins, a characteristic of most types of chronic liver diseases. Accumulation of ECM proteins distorts the hepatic architecture by forming a fibrous scar. Subsequent development of nodules of regenerating hepatocytes defines cirrhosis, which produces hepatocellular dysfunction and increased intrahepatic resistance to blood flow. These result in hepatic insufficiency and portal hypertension, respectively [17].

The onset of liver fibrosis is usually insidious, and most of the related morbidity and mortality occur after the development of the disease into late stage, which is cirrhosis [18]. Progression to cirrhosis normally occurs after an interval of 15-20 years for majority of patients. Clinical complications of cirrhosis include ascites, renal failure, hepatic encephalopathy, and variceal bleeding.

For most patients, cirrhosis is associated with short survival, and liver transplantation is often indicated as the only effective therapy [19]. Patients with cirrhosis are also at much higher risk of developing hepatocellular carcinoma. Currently, cirrhosis and hepatocellular carcinoma are among the top ten causes of death worldwide, and in many developed countries liver disease is now one of the top five causes of death in middle-age group [20, 21]. Liver fibrosis can progress rapidly to cirrhosis in several clinical settings, such as repeated episodes of severe acute alcoholic hepatitis, subfulminant hepatitis, and fibrosing cholestasis with Hepatitis C Virus (HCV) reinfection after liver transplantation [22]. The causal and natural history of liver fibrosis is influenced by genetic as well as environmental factors [23] (Table 1).

Table 1. Genetic and nongenetic factors associated with fibrosis progression in different types of chronic liver diseases

Type of liver disease	Candidate genes	Nongenetic factors
Chronic HCV infection	Hereditary hemochromatosis gene	Alcohol intake
	Angiotensinogen	Coinfection HIV and/or hepatitis B virus
	Transforming growth factor β1	Age at time of acute infection
	Tumor necrosis factor α	Liver transplantation
	Apolipoprotein E	Diabetes mellitus
	Microsomal epoxide hydroxylase	No response to therapy
	Monocyte chemotactic protein type 1 and type 2	
	Factor V (Leiden)	
Alcohol induced	Interleukin 10	Alcohol intake
	Interleukin 1β	Episodes of alcoholic hepatitis
	Alcohol dehydrogenase	
	Aldehype dehydrogenase	
	Tumor necrosis factor α	
	Transport-associated antigen-processing type 2	
NASH	Hereditary hemachromatosis gene	Age
	Angiotensinogen	Severity of obesity
	Transforming growth factor β1	Diabetes mellitus
		Hypertriglyceridemia
PBC	Interleukin 1β	
	Tumor necrosis factor α	
	Apolipoprotein E	
Autoimmune hepatitis	Human leukocyte antigen type II hyptotypes	Type II autoimmune hepatitis
		No response to therapy

2.1.2 Pathogenesis of liver fibrosis

Liver fibrosis results from wound-healing response to repeated liver injury [24]. Once acute liver injury occurs, parenchymal cells regenerate and replace the necrotic or apoptotic cells. Inflammatory response comes with this process, together with limited deposition of ECM. If the hepatic injury persists,

eventually the liver's regeneration function would fail, and hepatocytes are substituted with abundant ECM, especially fibrillar collagen. Distribution of such fibrous material is dependant on the location of the onset of the liver injury. For chronic viral infection and chronic cholestatic disorders, fibrotic tissue is initially located around portal tracts, while in alcohol and drug-induced liver disease, it locates in pericentral and perisinusoidal areas [25]. With the progression of the fibrotic liver disease, the collagen forms bridging fibrosis and frank cirrhosis occurs.

Development of liver fibrosis features in major alterations in both quantity and deposition of hepatic ECM. Activated hepatic stellate cells (HSC) are believed to be the major producers of the fibrotic neomatrix [12, 26]. In normal liver, hepatic stellate cells reside in the space of Disse and are the major storage sites of vitamin A, stored in the cytoplasm as retinyl esters. Following chronic liver injury, HSCs undergo morphological and functional changes, proliferate and activate or transdifferentiate into smooth muscle α–actin positive myofibroblast-like cells (activated HSC), acquiring contractile, proinflammatory and fibrogenic properties, meanwhile lose their vitamin A storage [27, 28]. Another endogenous liver cell type that is implicated in hepatic fibrogenesis is the portal fibroblast, which is derived from small portal vessels [29]. However, they proliferate more slowly than activated HSCs and would only be activated during portal injury [30]. Therefore, they have smaller contribution to liver fibrosis than HSCs. Circulating fibrocytes [31], bone marrow [32] and Epithelial-Mesenchymal Transition (EMT) [33] would also contribute to the myofibroblasts formation and fibrosis progression. However, the relative contribution of each source varies among different etiologies (Figure 2).

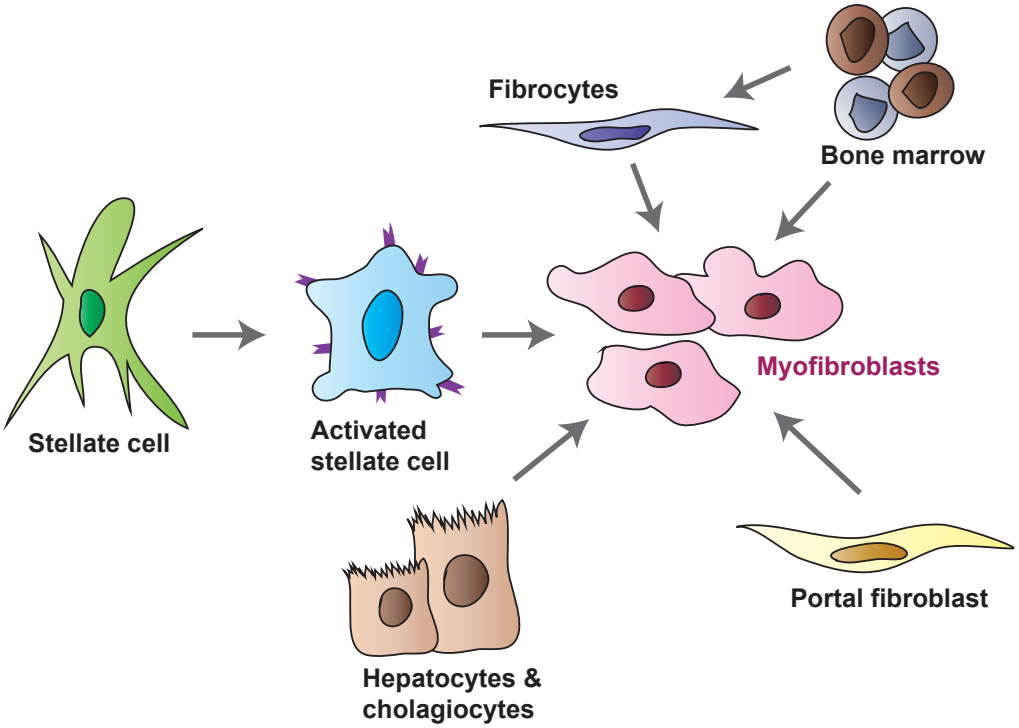

Figure 2. Contributions of activated stellate cells and other fibrogenic cell types to hepatic fibrosis. Quiescent stellate cell activation is initiated initially by a range of soluble mediators, and further by key cytokines into myofibroblasts (which contain contractile filaments). Over time, however, other sources also contribute to fibrogenic populations in liver, including bone marrow (which likely gives rise to circulating fibrocytes), portal fibroblasts, and epithelial mesenchymal transition from hepatocytes and cholangiocytes. Relative contributions and the stages at which these cell types add to the myofibroblast population is likely to differ among various etiologies of liver injury.

Activated HSCs migrate and accumulate at the tissue reparing sites, produce a wide variety of collagenous and non-collagenous ECM proteins and regulate ECM degradation. Collagen synthesis in HSCs in fibrotic liver tissue is regulated at both transcriptional and posttranscriptional levels [34]. Over time, subendothelial matrix composition changes into one rich in fibril-forming collagens. These progressive changes in matrix composition due to fibrosis accumulation also trigger several positive feedback pathways that further amplify fibrosis. These include the stellate cell activation and migration by membrane receptors signaling [35], release of growth factors to stimulate fibrogenesis through activation of cellular matrix metalloproteases [36, 37], and stimu-

lus to stellate cell activation by matrix stifferning due to the enhanced density of ECM [38]. Due to these factors, in advanced stages, liver contains approximately six times more ECM overall than normal liver, and there is increasing deposition of collagen types I and IV, undulin, elastin and laminin. Although collagen types I, III and IV are all increased, type I increases most and its ratio to types III and IV also increases [39-42]. Also, as the prototype constituent of the fibril-forming matrix in fibrotic liver, collagen type I degradation is being particularly important for recovery of normal liver histology [43].

2.1.3 Diagnosis of liver fibrosis

The stage of liver fibrosis is a measure of how far it has progressed in its natural history, with end stage resulting in cirrhosis with clinical decompensation or liver organ failure. The grade of liver fibrosis is meant to reflect how quickly fibrosis is progressing to the end stage. Evaluation of fibrosis stage over time can determine the disease progression, response to therapy and optimization of treatment. Ability to identify the occult advanced fibrosis may also direct further management [44].

Currently, liver biopsy is still considered the gold-standard method for the diagnosis and assessment of liver fibrosis. Histological examination is performed to identify the underlying cause of liver disease and assessing grade and stage of fibrosis, usually scaled as Metavir (stage 0-4) [45] and Ishak score (stage 0-6) [46], with progression in stage advances from none to fibrous portal expansion to bridging fibrosis to incomplete cirrhosis and finally to established cirrhosis. Numerical numbers are assigned to correspond to these

stages (Table 2). Specific staining of ECM proteins (with Sirius red or Masson's trichrome) is used for such histological grading. As an invasive procedure, liver biopsy comes with pain and major complications occurring in 40% and 0.5% of patients, respectively [47]. Since needle liver biopsy only removes 1/50000 of the total organ, sampling error can occur, and it will affect the extent to which grading and staging can be accurately performed. Study has shown that cirrhosis is missed on single blind liver biopsy in between 10% and 30% of cases [48-50]. Studies have suggested that an adequate biopsy sample should be 15mm long at least and have more than 5 portal tracts [51, 52]. When many good quality biopsies are evaluated, however, as in laboratory study or in clinical trial, a great degree of accuracy can be achieved [46]. Also, inter- and interaobserver variability in the interpretation of the needle biopsy results is well know to occur, and histological examination does not predict disease progression [6].

Table 2. Grading and staging systems for chronic liver fibrosis using different scoring systems.

stage	Metavir	Ishak score
0	No fibrosis	No fibrosis
1	Fibrous portal expansion	Fibrous expansion of some portal areas, with or without short fibrous septa
2	Few bridges or septa	Fibrous expansion of most portal areas, with or without short fibrous septa
3	Numerous bridges or septa	Fibrous expansion of most portal areas with occasional portal to portal bridging
4	Cirrhosis	Fibrous expansion of most portal areas with marked bridging (portal to portal as well as portal to central)
5		Marked bridging (portal-portal and/or portal-central) with occasional nodules (incomplete cirrhosis)
6		Cirrhosis, probable or definite

Besides liver needle biopsy, a large number of putative serum markers are also evaluated for the assessment of hepatic fibrosis. Scores that include routine laboratory tests, such as platelet count, aminotransferase serum levels, prothrombin time, and acute phase proteins serum levels are proposed [53, 54]. Other serum levels of proteins that directly related to hepatic fibrogenic process are also used [55]. These scores are useful for detecting advanced fibrosis as well as no fibrosis, however, when it comes to intermediate grades, these scores are not very accurate. Meanwhile, all the fibrosis-specific markers in the blood may reflect fibrogenesis in other organs and would be affected by changes in their metabolism. Therefore, unless ideal features [56] (Table 3) of fibrosis markers can be met, biopsy still lies in as the best way for diagnosis.

Table 3. Ideal features of a fibrosis biomarker

Liver specific
Independent of metabolic alterations in liver, renal, or reticuloendothelial function
Easy to perform
Minimally altered by urinary or biliary excretion
Reflective of fibrosis from any chronic liver injury
Sensitive to discriminate between different stages of fibrosis
Ability to correlate with dynamic changes in fibrosis progression or regression
Ability to predict clinical outcomes including liver failure and mortality

Other non-invasive diagnostic tools include ultrasonographic and tomographic evaluation of the liver. Transient elastography (FibroScan) is rapid bedside method for assessing liver fibrosis by measuring liver stiffness, and recent studies suggest that it has the potential to detect significant fibrosis [57]. However, inherent limitation of this technique is that it may not give accurate results in obese patients, as the depth of the signal penetration is limited. Also, stiffness of liver is changing with age, so better standardization will be re-

quired for large scale application. Other study also shows that transient elastography is biased when patients is undergoing acute liver damage [58]. Magnetic resonance spectroscopy (MRS) has drawn growing interest in potential role for detecting fibrosis, however, currently most studies used small number of samples, and therefore needs to be confirmed in larger studies with standardized methods [59]. Magnetic resonance elastography (MRE) is currently being evaluated for diagnosis purpose, however, albeit with the encouraging initial data, high negative predictive value may only allow it to be used for patients who are under consideration for biopsy to assess possible hepatic fibrosis [60]. MRS and MRE also both need special room to perform the procedure and highly dependent on operator expertise. In all, although current non-invasive imaging methods have less sampling errors as biopsy, these methods still have their drawbacks, and therefore, cannot be used routinely and obviate the need for liver biopsy.

Since liver biopsy still remains the only reliable method for assessment of fibrosis, most therapeutic approaches discovered in rodents [61] to prevent fibrosis progression have not been proven in human due to the need to perform serial liver biopsies to accurately determine the changes in fibrosis, and the necessity of long-term follow-up studies. Therefore, in the long run, the availability of reliable non-invasive or minimum-invasive markers of liver fibrosis should have a remarkable impact on the design of clinical trials as well as live animal studies, and that would also benefit patients with chronic liver disease who need long term follow up.

2.2 Imaging modality SHG and TPEF

2.2.1 Theory and advantages of SHG and TPEF

There are a number of notable nonlinear optical techniques, including multi-photon excited fluorescence [62], higher harmonic generation [63, 64] and Raman scattering [65]. All of them are nonlinear responses of the material to high power light excitations. Even though the physical origin of each phenomenon is starkly different, comparison of these techniques are derived according to their sensitivity and selectivity.

In terms of sensitivity, multi-photon excited fluorescence has the potential for single molecule detection whereas higher harmonics require 10^4 to 10^6 molecules for their detection. This limits higher harmonics applications in the detection of one or a small number of molecules. On the other hand, coherent anti-stokes and stimulated Raman scattering [66] provide an unprecedented means of chemical selectivity which is intrinsic to the molecules within cells and tissues as the vibrational bands of each kind of molecule serves as a spectral signature which can be utilized as a contrast mechanism for imaging. In addition to vibrational spectroscopic methods, higher harmonics can differentiate molecular orientation and show specificity for membranes.

The macroscopic polarization is proportional to the electric field strength in the regime of linear optics. $\mathbf{P} = \chi^{(1)} \varepsilon_0 \mathbf{E}$ where ε_0 is the relative permittivity of free space and $\chi^{(1)}$ is the linear susceptibility of the medium independent of the field. As the electric field strength becomes comparable to the intra-atomic

electric field, as in the case of laser radiation, the response becomes nonlinear. Since nonlinear response usually manifests itself as small deviations from linear response, a power series expansion in the field is used, $\mathbf{P} = \chi^{(1)}\mathbf{E} + \chi^{(2)}\mathbf{EE} + \chi^{(3)}\mathbf{EEE} + \ldots$ where the susceptibilities $\chi^{(1)}$,$\chi^{(2)}$ and $\chi^{(3)}$ are tensors of second, third and fourth ranks respectively.

Almost all optical phenomena are described by the first three terms in the equation. The linear term involving $\chi^{(1)}$ gives rise to the index of refraction, absorption, dispersion and birefringence of the medium. Most of the interesting nonlinear optical effects arise from the terms of electric polarization, which are quadratic or cubic in the electric field. The quadratic polarization gives rise to the phenomena of second harmonic generation, sum- and difference- frequency mixing, and parametric generation, while the cubic term is responsible for third-harmonic generation, two-photon absorption, stimulated Raman scattering, optical bistability and phase conjugation.

Fluorescence is the optical relaxation phenomenon whereby light emission occurs in the time scale of nanoseconds after excitation from singlet ground state to singlet excited state. The energy of the emitted photon on relaxation corresponds to the difference in energy of the lowest vibrational level of the excited state and the vibrational level of the singlet ground state. Maria Göppert-Mayer made the first prediction of the possibility of multiphoton excitation in her doctoral thesis in 1931 [67] which was not experimentally realized until 1961 by Kaiser and Garret [68] following the development of lasers. In conventional one-photon absorption, excitation occurs when the photon energy absorbed matches the energy difference between the ground and excited

states. Two less energetic photons can be simultaneously absorbed for the same transition. The basic principle of TPEF is shown schematically in Figure 3.

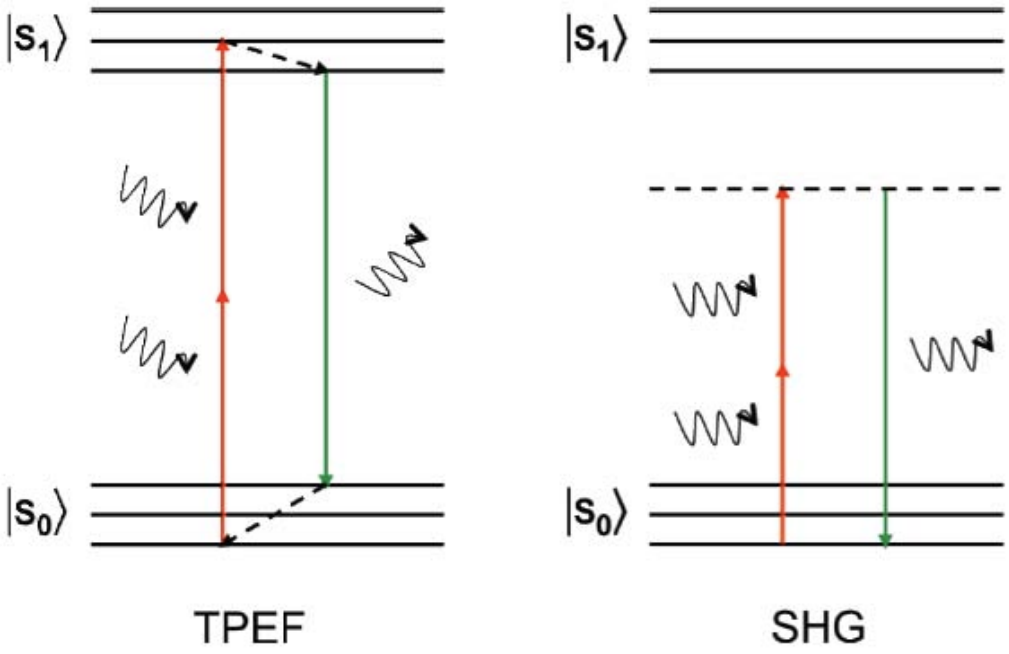

Figure 3. Jablonski diagram of the Two Photon Excitation Fluorescence (TPEF) and Second Harmonic Generation (SHG) process.

The interaction between the fluorophore and excitation electromagnetic field are solutions to time-dependent Schrödinger equation through perturbation theory where the Hamiltonian contains an electric dipole interaction term: $\boldsymbol{E}_\gamma \cdot \boldsymbol{r}$ where $\boldsymbol{E}_\gamma$ is the electric field vector of the photons and **r** is the position operator. The nth-order solution corresponds to n-photon excitation with transition probability, P and, for the two-photon excitation process, $P^{(2)}$ is given by [69]

$$P^{(2)} \approx \left| \sum_m \frac{\langle f | E_\gamma \cdot r | m \rangle \langle m | E_\gamma \cdot r | i \rangle}{\varepsilon_\gamma - \varepsilon_m} \right|^2$$

where ε_γ is the photonic energy associated to the electric field E_γ, f, i and m are the final initial and intermediate states respectively, and the summation is over all intermediate states m with energy ε_m.

The transition rate, $R^{(2)}$ is the time derivative of the transition probability as $R^{(2)} = \frac{d}{dt} P^{(2)} = \sigma^{(2)} I^2$ where $\sigma^{(2)}$ is the cross-section for the two-photon absorption process and I the intensity of the electromagnetic field. This two-photon absorption rate is proportional to the imaginary part of the third-order nonlinear optical susceptibility. The selection rules for transitions between final and excited states are symmetry and parity dependent which is the result of group theoretic and spin considerations of the system respectively. In two-photon processes, a transition between states of the same parity is allowed as a result of two dipole terms in $P^{(2)}$, unlike the case for one-photon transitions where it is forbidden.

We next divert our discussion towards the theory of second harmonic generation (SHG). We begin from Maxwell's wave equation for a non-absorbing, non-conducting dielectric medium containing no free charges [70], the diagram of SHG process is shown in Figure 2. $\nabla^2 E - \frac{n^2}{c^2} \frac{\partial^2 E}{\partial P^{NL} t^2} = \mu_0 \frac{\partial^2 P^{NL}}{\partial t^2}$ where $\boldsymbol{E}$ is the electric field vector of the electromagnetic field and $\boldsymbol{P}^{NL}$ is the polarization vector containing higher order susceptibilities of the medium. Since we are interested in second order nonlinear effects, we can ignore higher order terms than χ^2 and assume that the electromagnetic waves are plane waves propagating in the z direction. We simplify our analysis by considering a total field E consisting of three infinite uniform plane waves ignoring the effects of double refraction and focusing. The total instantaneous field is therefore of the form $E_i(z,t) = E_i(z) e^{-i\omega_j t} + c.c. = A_i(z) e^{i(k_j z - \omega_j t)} + c.c$ where j = 1, 2, with $\omega_1 = \omega$ and $\omega_2 = 2\omega$, E_j is the complex amplitude of field j, A_j

represents the spatially slowly varying field amplitude and c.c. means complex conjugate. $P_2(z,t) = P_2(z)e^{2\pi(k_1 z - w)} + c.c.$ where P_2 represents the complex amplitude of the nonlinear polarization. If these expressions are introduced to the above wave equation and utilizing the slowly varying amplitude approximation, we obtain $\frac{dA_2}{dz} = \frac{2i\omega}{n_2 c}\chi^{(2)}A_1^2 e^{i(2k_1 - k_2)z}$ Upon direct integration, assuming A_1 to be constant, we find the amplitude of the second harmonic field after propagation through a distance L to be given by $A_2(L) = \frac{2i\omega\chi^{(2)}A_1^2}{n_2 c}\frac{e^{i\triangle k} - 1}{i\triangle kL}$ where $\triangle k = 2k_1 - k_2$. The intensity of the generated radiation is thus $I_2(L) = \sqrt{\frac{\mu_0}{\varepsilon_0}}\frac{2\omega^2}{n_1^2 n_2 c^2}\left[\chi^{(2)}\right]^2 I_1^2 L^2\left[\sin c^2\left(\frac{\Delta kL}{2}\right)\right]$ Only those interactions for which Δk = 0 will undergo macroscopic amplification as they propagate through the medium. Nevertheless, even though the second order nonlinear susceptibility, $\chi^{(2)}$, is non-zero in non-centrosymmetric media, nonlinear emission dipoles aligned in an anti-parallel arrangement which produce SHG exactly out of phase, may result in the cancellation of the signals due to destructive interference.

2.2.2 Application of SHG and TPEF in biological study

Nonlinear microscopy with its distinct advantages for 3D imaging is considered to be an alternative to conventional confocal microscopy for the imaging of biological samples. Two-photon excitation fluorescence (TPEF) microscopy can provide optical sectioning without absorption above and below the plane of focus, thus greatly reducing photobleaching and phototoxicity, com-

pared to confocal microscopy. In addition, the penetration depth is increased many times up to a few hundreds microns [71]. Nowadays, this technique is used for imaging electrical activity in deep tissue, such as mapping network organization of neuronal electrical activity [72, 73] and the 3D blood flow architecture in the brain [74]; Quantitative imaging of immune-cell motility and morphology, such as the *in vivo* interaction of T cells and dendritic cells (DCs) dynamics in lymph nodes [75], in cranial bone marrow [76] and in tumors [77]; imaging structure and function of cancer, such as studying gene expression and physiological function in the deep internal regions of tumors [78].

Another important nonlinear microscopy recently widely used in life science research is second harmonic generation microscopy (SHG). Compared to conventional fluorescence imaging, SHG exhibits intrinsic advantages, as the process requires no fluorophore presence in tissue; thus, signals are unaffected by dye concentration and photobleaching. Besides, the excitation source can be in the infrared range, resulting in less scattering in tissues than that in the visible wavelength range and deeper tissue penetration for imaging purposes. Two main areas of research in SHG imaging over the past few years have been measuring neurons and collagen, which have special structural properties [79, 80]. In particular, SHG can be used for quantitative measurement of collagen in various organs as an indication of fibrosis development [13, 79, 81], especially for detect fibrosis in livers [82].

2.2.3 Image processing techniques in extracting SHG/TPEF signals

To extract useful information from digitized SHG/TPEF images, and to further study and quantify such information, image processing techniques are employed after images are acquired. Current state-of-the-art image processing techniques include: Histogram thresholding, region based approaches, edge detection, Fuzzy techniques and Neural Network approaches.

Histogram thresholding is one of the most commonly used techniques in image processing. It can be done based on global information, the gray level histogram of the entire image, or, it can be done using local information, gray levels of the sub-regions that are partitioned from the whole image. This is also known as adaptive thresholding [83-85]. Thresholding can also be classified into bilevel and multi-thresholding. In bilevel thresholding, the image is partitioned into two regions: object (black) and background (white), whilst in multithresholding, the image is separated into several objects based on surface characteristics with multiple thresholds for segmentation. If the image is composed of regions with different gray level ranges, the histogram of the image usually shows different peaks, with each corresponding to one region and adjacent peaks separated by a valley. There are various thresholding methods available for this. Commonly used ones include Otsu, which maximizes the ratio of the between class variance (or minimize the intra-class variance) to the local variance to obtain thresholds [86].

Region based approaches attempt to group pixels into homogeneous regions, and include region growing, region splitting, region merging and their combi-

nations [87, 88]. It works best on images with an obvious homogeneity criterion and tend to be less sensitive to noise. In general, it is preferred for color image segmentation. In region growing approach, a seed region is selected and then expanded to include all the homogeneous neighbors until all pixels in the image are classified. Problem with this approach is the inherent dependence on the seed region selection as well as the order in which pixels and regions are examined. In region slitting approach, the whole image is regarded as initial seed region. If seed region is not homogenous, it is then divided into four squared sub-regions as the new seed regions. The process is repeated until all sub-regions are homogenous. The disadvantage of this approach is the tendency of the results mimicking the data structure, the square shape. The region merging approach is frequently combined with region growing and region splitting approach to merge the similar regions into larger homogeneous regions. It suffers the same drawbacks as the previous two methods.

Edge detection is based on detection of discontinuity in gray level, which locates points of abrupt changes in gray level intensity values. Techniques in edge detection are usually classified into two categories: sequential and parallel [89, 90]. Sequential edge detection means the decision whether a pixel is an edge pixel or not is dependent on the result of the previously examined pixels. The performance of a sequential edge detection method is dependent on the choice of an appropriate starting point and how the results of the previous points affect the choice and result of the next point. The existing techniques mainly utilize heuristic search and dynamic programming. Parallel edge detection means the decision whether a point is an edge is made based on the point under consideration and its neighboring points. Therefore, this method can be

applied to every point in the image simultaneously. One technique in performing parallel edge detection is high-emphasis spatial frequency filtering. Since high spatial frequencies are associated with sharp changes in intensity, Fourier operator can be used to perform high-pass filtering to extract edges. The question lies in how to design a relevant filter.

The image processing techniques mentioned above are all based on crisp decisions about regions. However, regions in an image are not always crisply defined, and uncertainty occurs at each level of image analysis and pattern recognition. Fuzzy techniques provide a mechanism to represent and manipulate uncertainty and ambiguity [89, 91]. In fuzzy subsets, each pixel in an image has a degree to which it belongs to a region, characterized by a membership value. By doing so, information can be kept through the higher processing levels. Fuzzy-C means (FCM) clustering algorithm [92] has been widely used in image segmentation. It is an iterative optimization method, which calculates the memberships of a data point in each of the clusters based on the distances between the point and the cluster centers. The cluster centers are then updated to reflect the resulting clusters. An objective criterion function is used in the iteration to minimize the distance between data point in a cluster and the cluster center, and to maximize the distance tween between cluster centers. The cluster centers are then updated to reflect the resulting clusters. An objective criterion function is used in the iteration to minimize the distance between data point in a cluster and the cluster center, and to maximize the distance tween between cluster centers. The algorithm minimizes intra-cluster variance as well, but the minimum is a local minimum, and the results depend on the initial choice of weights.

Neural networks based approaches [93, 94] are attempted to achieve the goal of robust segmentation of the system with respect to random noises, able to emulate some aspects of the human information processing system and have output in real time. Neural networks are composed of many computational elements connected by links with variable weights. The massive connectionist architecture makes the system robust while the parallel processing enables the system to produce output in a real time fashion. The complete network represents a very complex set of interdependencies, which allow very general functions to be modeled. Training time is usually very long, but after training, the classification using neural network is rapid. Overtraining should also be avoided and the initialization of the training set may also affect the results.

In general, the selection of an appropriate image processing method or algorithm mainly depends on the type of images and application areas. In this thesis, we have explored a few methods for our fibrosis quantification purpose.

2.3 Significance of using SHG/TPEF in liver fibrosis study

Since percutaneous liver biopsy still represents the gold standard in liver fibrosis diagnosis and assessment, to specifically and accurately monitors liver fibrosis in a quantitative manner, information extracted has to be directly compared to morphological features recognized by the histological examination of the liver biopsy samples. So far, putative serum markers have been tested to detect such changes, however, due to the nonspecificity nature of the markers, changes in them cannot be exclusively attributed to liver fibrosis. Non-invasive imaging methods have also been employed to explore the liver

changes, such as ultrasonography, transient elastography, and magnetic resonance elastography; however, they are based on liver stiffness measurement (LSM) rather than the histological changes. Thus, their sensitivity is less satisfactory and comparability to gold standard liver biopsy is low.

In light of the current limitations to liver fibrosis assessment and the advances of the state-of-art imaging modality SHG/TPEF, we are proposing in this thesis to use SHG/TPEF as an imaging tool to study liver fibrosis. Since the morphological features of hepatocytes can be detected by TPEF signals while collagen deposition, the vital indicator of liver fibrosis, can be monitored by the increase of SHG signals, images generated by SHG/TPEF can be used as a direct comparison to histopathological examinations with the advantage of not using dyes in imaging and less time required for data collection. With the right techniques in image processing, data collected from SHG/TPEF can be used for quantitative assessment of liver fibrosis.

Chapter 3 Objective and Specific Aims

This thesis aims to develop a novel detection and diagnostic method for liver fibrosis progression based on non-linear optical microscopy. To achieve this goal, three steps were taken, which formed the three specific aims in this thesis. Each aim solves a single scientific problem and constitutes a single chapter following Chapter 3 in this thesis to elaborate the studies and findings respectively.

Specific Aim One: To establish and modify a quantification system for liver fibrosis.

Hypothesis 1: Type I Collagen, which can be detected by SHG, as the most abundant collagen of mature scar tissue present in portal fields and fibrous septa, can be used as a quantitative measurement of liver fibrosis. Liver tissue morphology extracted by autofluorescence of liver cells can be quantified to reveal the important indication of fibrosis progression.

Specific Aim Two: To quantify liver fibrosis based on the information on and near liver surface

Hypothesis 2: The degree of liver fibrosis across the liver surface can be used as an indication of the fibrosis within the whole organ. Extracted information through SHG and TPEF imaging modalities within certain depth from liver surface alone will be enough to stage liver fibrosis progression.

Specific Aim Three: To modify and stabilize an intravital window based imaging chamber in live animal for investigation of fibrogenesis and detection of liver fibrosis in vivo.

Hypothesis 3: Fibrogenesis in liver can be better studied by visually detecting the fibrosis progression pattern in live animals. By live imaging the liver surface through a window based chamber with enough penetration depth, the fibrosis across the whole liver can be understood accurately.

Chapter 4 Establish and Modify a Quantification System for Liver Fibrosis

4.1 Introduction

Liver fibrosis, as a common pathway leading to cirrhosis, the end result of injury of the liver, is becoming an increasing concern worldwide, with most occurrences in Asia Pacific as a consequence of acquiring hepatitis viruses. Accurate assessment of the degree of fibrosis is important for both clinical treatment and laboratory studies. With the evolvement of current fibrosis treatment, which aims at reversing fibrosis, such precise assessment is becoming more demanded for therapeutic efficacy evaluation [45, 95, 96]. Liver biopsy is considering the "gold standard" to assess fibrosis, however, its semi-quantitative analysis based on histological staining suffers many drawbacks, such as limited sensitivity, accuracy and operator-dependent variations [46, 97]. Also, such results are highly subjected to interpretations by the observers [98-102]. It is reported that the intra- and interobserver discrepancy is as high as 35% in the assessment of liver fibrosis [98, 103-106] despite efforts to improve diagnostic accuracy for qualitative scoring systems [46, 95]. Other morphometric quantification systems such as FibroXact, FibroQuant, Bioquant Nova Prime have been reported to achieve a continuum in fibrosis quantification based on automated color segmentation [101, 107-110]. However, the common difficulty faced by those procedures is the variation in the staining process resulting from different batches of stains, protocols, time-dependent fading and photobleaching.

Over the past decades, second harmonic generation (SHG) microscopy and two-photon excitation fluorescence (TPEF) have been increasingly used in biological science research. Since SHG is a nonlinear optical process, it exhibits its intrinsic advantages over conventional fluorescence imaging by requiring no fluorescent molecules in the tissue to generate signals and minimum photobleaching. Longer wavelength excitation sources such as infrared range are often used for SHG, therefore, deeper tissue penetration and less scattering in tissues can be achieved [111-117]. Since SHG microscopy is sensitive to highly ordered structures without central symmetry in tissue, such as type I collagen [13, 81], it has been used for quantitative measurement of collagen in various organs as an indication of fibrosis development [13, 118]. The feasibility of using SHG microscopy in observing fibrosis in liver has also been demonstrated [82, 119]. Our group has developed a SHG based imaging system for highly sensitive collagen detection. The signals detected are standardized and highly reproducible.

In this study, we first developed a comprehensive animal liver fibrosis model of different severity level. After unsuccessful screening of mutant Zebrafish that are susceptible to liver damage, we established a rat fibrotic model that is comparable to human Primary Biliary Cirrhosis (PBC) and Biliary atresia (BA) using Bile Duct Ligation (BDL) surgery. Then combining TPEF and SHG microscopes, we systematically developed an automated morphology-based quantification system to assess the fibrosis progression. We extracted and validated such morphological features during fibrogenesis by comparing the images from SHG/TPEF with images from Masson's trichrome-stained images, with the help from a pathologist. Such quantification results are also

validated by comparing scores with the existing gold standard for liver fibrosis diagnosis: qualitative morphological staging performed by pathologists. Our results confirm that our quantification system can sensitively identify morphological features from liver tissues, and the general trend of all the features we identified are consistent with the pathogenesis of liver fibrosis. Using our imaging modality for quantification of liver fibrosis therefore can automate the diagnosis of liver fibrosis with high accuracy and also significantly reduce the time required for diagnosis by removing the tissue staining process and eliminating inter- and intraobserver discrepancies.

4.2 Materials and Methods

4.2.1 Zebrafish housing and mutagenesis

Male Zebrafish were mutagenized by treatments with 3.0mM N-ethyl-N-nitrosourea (ENU) as described by literature [120]. Surviving and fertile fish were outcrossed with heterozygous *albino* (*alb*/+) females to generate F1 progeny for the library. To generate a library of 1056 mutagenized fish, healthy looking F1 males and females were finclipped (tail) and grouped into 12 fish per tank of 88 pools. To later recover the fish carrying a specific mutation, all 12 fish from apositive pool were finclipped again, housed separately, and genotyped.

4.2.2 Genome DNA isolation and DNA library Construction

Genomic cDNA for the library was isolated from finclips in 96-well plates for the library and single tubes for the genotyping. Freshly cut finclips were transferred directly to plates/tubes that are kept on dry ice. Fins were lysed by overnight incubation at 55°C in 400 µL pre-warmed lysis buffer (100 mM Tris-HCl at pH 8–8.5, 200 mM NaCl, 0.2% SDS, 5 mM EDTA, and 100 µg/mL proteinase K). DNA was precipitated by adding 300 µL of isopropanol and centrifugation at >6000*g*, and washed using 70% ethanol. Pellets later were dissolved in 1mL of water. For the DNA library, 5-µL aliquots were arrayed in 96-well PCR plates, covered with aluminum foil tape and stored at -20°C.

4.2.3 Polymerase Chain Reaction (PCR) of mutant gene

Target gene *hepatocyte growth factor-like* (*hgf-like*) is amplied by a nested PCR approach. In the first PCR with three gene specific primers, a touchdown cycling program was used (94°C for 60 sec; 30 cycles of 94°C for 20 sec, 65°C for 30 sec with a decrement of 0.5°C per cycle, and 72°C for 60 sec; followed by 10 cycles of 94°C for 20 sec, 58°C for 30 sec, and 72°C for 60 sec, and an additional extension step of 72°C for 180 sec). PCR samples contained 5 μL of genomic DNA isolated from finclips, 0.2 μM forward (f1) and 0.2 μM reverse (r1) primer, 200 μM of each dNTP, 25 mM Tricine, 7.0% Glycerol (m/v), 1.6% DMSO (m/v), 2 mM MgCl2, 85 mM NH4Acetate (pH8.7), and 0.2 U Taq DNA polymerase in a total volume of 10 μL.

After the first PCR reactions, the samples were diluted with 20 μL of water, and 1 μL was used as template for the second, nested PCR reaction. This reaction contained a mixture of gene specific forward (0.08 μM) and reverse (0.04 μM) primers that contain universal M13 adaptor sequences at their 5' end, and the two corresponding universal M13F (0.1 μM) and M13R (0.1 μM) primers labeled with fluorescent dyes for detection. In addition, the PCR samples contained 200 μM of each dNTP, 20 mM Tris-Hcl (pH8.4), 50 mM KCl, 1.5 mM MgCl2, and 0.1 U Taq DNA polymerase in a total volume of 5 μL. Standard cycling conditions were used for the nested PCR reactions (30 cycles of 94°C for 20 sec, 58°C for 30 sec, and 72°C for 60 sec, followed by an additional extension step of 72°C for 180 sec).

4.2.4 Mutant Zebrafish screening

Following the nested PCR, PCR products were diluted with 30 μL of water, and 1 μL was used as template for the sequencing reactions. Sequencing reactions contained 0.5 μL of DYEnamic ET Terminator, 3.5 μL of ET Terminator dilution buffer, and 0.5 μM of M13F or M13R primer in a total volume of 10 μL. Cycling conditions were as recommended by the manufacturer. Sequencing products were purified using Sephadex G50 (superfine coarse) minicolumns, and analyzed on a 96-capillary 3730xl DNA analyzer from Applied Biosystems.

4.2.5 Rat Bile Duct Ligation (BDL) model establishment

Male Wistar rats at an average weight of 200g were housed two per cage. Sixteen rats were randomly separated as four groups, representing 4 time points, without BDL, and 2, 4, 6 weeks after BDL surgery. Under sterile surgical conditions, rats were sedated. Rats are weighted and injected with Ketamine (100mg/kg body weight). We allow 10-15 minutes for anesthesia to occur, indicated by the loss of sensory/ reflex response, i.e. non-response to tail pinching. The abdomen was shaved later. A transverse incision was made on the abdomen, exposing the liver. The liver and intestines were gently displaced to expose the bile duct, which were ligated at two areas near the porta with non-absorbable sutures (silk 3.0) and then transected between the two ligation points. Abdominal contents then were gently rearranged and the wound closed with double layered tissue closure with absorbable sutures (PDS 4.0). Tetracycline HCL was applied on the closure wound and plastered with a water proof-

ing protection. Four animals were sham operated. The operation was performed on the heating operation table with surgical lamps to prevent heat loss during the operation. All animal-related experiments were approved by the Institutional Animal Care and Use Committee (IACUC).

4.2.6 Liver sample extraction from BDL model

Two, four, six weeks later after BDL surgery, the animals were sacrificed. Rats are weighted and injected with Ketamine (100mg/kg body weight). Allow 10-15 minutes for anesthesia to occur, indicated by the loss of sensory/ reflex response, i.e. non-response to tail pinching, same as when performing the BDL surgery. The livers were perfused through portal vein, with perfusion pressure controlled by constant gravity. We flushed the rats livers with 1×PBS of 200mls per rat, followed by perfusion of fixative containing 4% formaldehyde freshly prepared of 300mul per rat. After the perfusion, whole liver organ was harvested and placed in buffered fixative for further slice sample preparation.

4.2.7 Sample preparation

4.2.7.a Cryosection

After fixation, liver tissues were rinsed with 1×PBS, and then cryoprotected with 20% sucrose in phosphate at 4°C overnight. Transfered the tissue to an embedding mold and filled the mold with Optimum Cutting Temperate (OCT) compound. Rapidly submerged the mold into isopentane cooled with liquid

nitrogen for the material to freeze. After frozen, the whole block was wrapped in aluminum foil and stored at -80°C. We cooled the crystat to -20°C before moving the tissue block into place, and cut the sections to 50μm thickness. We picked each slice up by pressing a glass slide on the tissue, so that it melts and adheres.

4.2.7.b Paraffin embedded section

After the fixation, liver tissues were dehydrated by first using graded ethanol solutions, then graded xylene solutions, then finally liquid paraffin. The graded solutions gradually expose the sample to changes in hydrophobicity, minimizing damage to cells. After a short time in the liquid paraffin, the tissue was placed into a mold with more paraffin. Embedded samples were cut into 50μm thick sections using a microtome. After several slices of the paraffin-embedded tissue have been sectioned, the slices were removed from the blade and floated atop a warm water bath to smooth out the sample. The slices were teased apart and floated onto a slide. After the slides have dried, they were placed in an oven at 40°C to bake overnight. Before imaging, slices were deparaffinized in 2-3 changes of xylene, and hydrate in increasing graded ethanol solutions. Then rinsed in distilled water.

4.2.7.c Masson's Trichrome staining

After deparaffin of embedding sections, tissue slices were stained first in Weigert's iron hematoxylin solution for 10 minutes, flowered by rinsing in distilled water. Then they were stained in Biebrich scarlet-acid fuchsin solution for 15 minutes, followed by rinsing. Differentiated the slices later in phos-

phomolybdic-phosphotungstic acid solution for 10-15 minutes to check whether collagen is not red. Counterstain in blue aniline solution was performed for 5 to 10 minutes, followed by differentiating in 1% acetic water for 3 to 5 minutes. Last, we dehydrated and cleared the stain through 95% ethyl alcohol, absolute ethyl alcohol, and xylene, 2 changes each, 2 minutes each. Mounted with resinous medium. After the staining, nuclei were stained black, muscle, cytoplasm, keratins were stained red and collagens were stained blue [121].

4.2.7.d Sirius red staining

After deparaffin and hydrate sections, nuclei were stained with Weigert's haematoxylin for 8 minutes, followed by 10 minutes wash in running tap water. We stained the slices later in picro-sirius red for one hour, followed by washing in two changes of acidified water. We then physically removed most of the water from the slides by vigorous shaking and dehydrated in three changes of 100% ethanol. Finally, we cleared the slices in xylene and mount in a resinous medium. In bright-field microscopy collagen is red on a pale yellow background [122, 123].

4.2.8 Histopathological scoring of fibrosis samples

After Masson's Trichrome and Sirius red staining of each sample, stained tissues were imaged under optical microscope, and each sample was given a numerical score stating the severity of the liver damage. (Both staining were provided for each sample to minimize the variation of staging caused by stain-

ing process.) All animal tissue scoring was performed by a pathologist according to Ruwart et al as there was extensive bile duct proliferation noted [124], making it the better scoring system compared with others conventionally used.

4.2.9 Non-linear microscopy

The non-linear optical microscope was developed based on a confocal imaging system (LSM 510, Carl Zeiss, Heidelberg, Germany) using an external tunable mode-locked Ti:Sapphire laser (Mai-Tai broadband, Spectra-Physics). The system is shown in Fig. 1, where laser bean was passed through a pulse compressor (Femtocontrol, APE GmbH, Berlin, Germany) and an acousto-optic modulator (AOM) for group velocity dispersion compensation and power attenuation respectively. The Laser bean was then routed by a dichroic mirror (reflect >700nm, transmit <543nm), through an objective lens (plan-neofluar, 20X, NA=0.5, Carl Zeiss, Heidelberg, Germany), to the tissue sample. The average power at the objective lens is ~80mW. TPEF in the epi-direction generated in tissue was collected by the same objective lens and recorded by a photo-multiplier tube (PMT, Hamamatsu R6357, Tokyo, Japan), after passing through the dichroic mirror (reflect <490nm, transmit >490nm) and a 500-550nm band-pass (BP) filter. SHG signal was collected in the forward direction using a condenser (NA=0.55) and filtered by a diaphragm and a 440-460nm band-pass filter before entering PMT for detection. With the intrinsic optical sectioning characteristics for non-linear optical process, the pinhole function of the confocal microscope was not used.

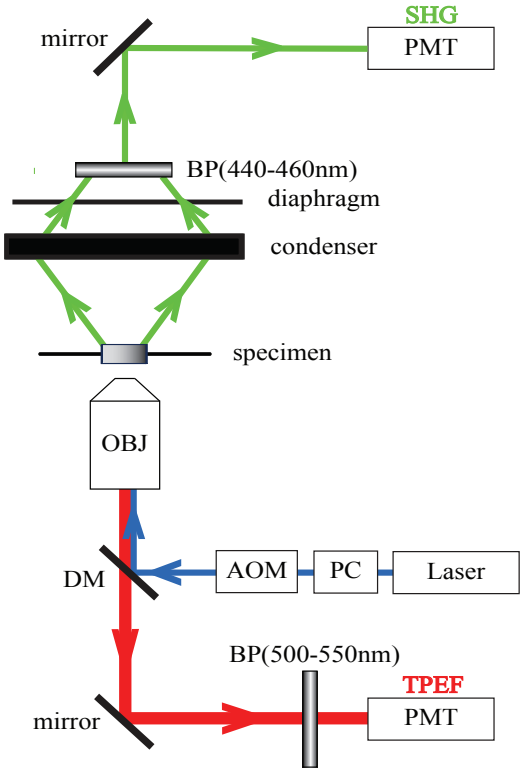

Figure 4. Schematic illustration of the optical configuration. Excitation laser was a tunable mode-locked laser (710 to 990nm set at 900nm) with a pulse compressor (PC) and an acousto-optic modulator (AOM) for power control. The laser went through a dichroic mirror , an objective lens (20X, NA=0.5), and reached tissue specimen. Second harmonic generation (SHG) signal was collected at the opposite side the laser source, in the transmitted mode, by a condenser (NA=0.55), through a field diaphragm, and a 440-460nm bandpass (BP) filter, before being recorded by a photomultiplier tube (PMT). Two-photon excited fluorescence (TPEF) was collected by the objective lens, filtered by a 500-550nm band-pass filter, before being recorded by another PMT.

4.2.10 Image acquisition

Based on the nonlinear optical microscope setup, unstained samples from two different preparation methods were imaged to compare the image quality. After the comparison, the better preparation method was chosen, and total of three tile scan images (4096×4096 pixels, ~2mm×2mm each) were taken from each tissue specimen, and two specimens were extracted from each animal (from both left and right lobe of the liver).

4.2.11 Image segmentation

For all images, image segmentation algorithms based on Otsu method [86], K-means clustering [125], Fuzzy-C means clustering [92] and Gaussian Mixture Model [126] were performed to identify collagen areas in SHG channel images.

In Otsu method, the threshold that minimizes the intra-class variance is exhaustively searched for. It is defined as $\sigma_\omega^2(t) = \omega_1(t)\sigma_1^2(t) + \omega_2(t)\sigma_2^2(t)$, in which weights ω_i are probabilities of the two classes separated by a threshold *t* and σ_i^2 are variances of these classes.

In K-means clustering, k cluster centers are first randomly picked (In collagen segmentation, k is 2 as one is for background, the other is for the collagen signal). Then each pixel in the image is assigned to the cluster that minimizes the distance between the pixel and the cluster center. Re-compute the cluster centers by averaging all the pixels in the cluster, and repeat the process until convergence is attained.

In Fuzzy-C means clustering, each point has a degree of belonging to clusters rather than belonging completely to just one cluster like in K-means. It is based on minimization of the objective function: $J_m = \sum_{i=1}^{N}\sum_{j=1}^{C} u_{ij}^m \left\|x_i - c_j\right\|^2, 1 \le m < \infty$, where *m* is any number greater than 1, u_{ij} is the degree of membership of x_i in the cluster *j*, x_i is the *i*th of d-dimensional measured data, c_j is the d-dimension center of the cluster, and $\|*\|$ is any norm expressing the similarity between any measured data and the center. Fuzzy parti-

tioning is carried out through an iterative optimization of the objective function shown, with the update of membership u_{ij} and the cluster centers c_j by: $u_{ij} = \frac{1}{\sum_{k=1}^{c}\left(\frac{\|x_i - c_j\|}{\|x_i - c_k\|}\right)^{\frac{2}{m-1}}}$, $c_j = \frac{\sum_{i=1}^{N} u_{ij}^m * x_i}{\sum_{i=1}^{N} u_{ij}^m}$. The iteration will stop when $max_{ij}\left\{\left|u_{ij}^{(k+1)} - u_{ij}^k\right|\right\} < \varepsilon$, where ε is a termination criterion between 0 and 1, whereas k are the iteration steps. The procedure converges to a local minimum of J_m.

In Gaussian Mixture Model, it is assumed that the histogram of intensity of pixels in the image can be modeled as the mixture of two Gaussian distributions, one representing pixels belonging to collagen area with strong SHG signals and the other representing the rest of the pixels belonging to non-collagen area. Using the Expectation-Maximization (EM) algorithm [126], the parameters of the Gaussian distributions were estimated. For all image segmentation algorithms used, a binary image was generated by applying value 1 to all the pixels having intensity that belongs to collagen area and value 0 to the rest of the pixels.

For TEPF channel images, pixels in the images were clustered into 3 different groups depending on pixel intensity: completely dark, dim, and bright which represent areas of the vessel or outside-tissue-space, bile duct proliferation area, and hepatocytes respectively. The clustering was performed by a Fuzzy-C means clustering method [127], in which each pixel was clustered into one of three clusters based on pixel intensity level. A binary image was generated by

applying value 1 to all the pixels belonging to the cluster that represents bile duct cell areas and value 0 to the rest of the pixels.

4.2.12 Features extraction and quantification

Four features were quantified, namely total collagen area percentage, bile duct proliferation area percentage, collagen in bile duct area percentage, and remnant hepatocytes area percentage as shown in Figure 5 and elaborated below.

Collagen area percentage is defined as the numbers of pixels that belong to collagen in the region divided by the total area.

Bile duct proliferation area percentage is defined as the numbers of pixels that belong to bile duct cells in the region divided by the total area.

The collagen in bile duct area percentage is defined as the number of pixels that are collagen and also in bile duct cells area divided by the total area of the sub-capsular region. The binary image of collagen in the bile duct area is generated by multiplying the binary images of the collagen area and the bile duct cell area.

Remnant hepatocytes are defined as those hepatocytes that are surrounded by bile duct cells. Morphological operations such as erosion, dilation and filling holes are performed on the binary image of bile duct cell to identify areas surrounded by bile duct cells. If these areas belong to the cluster that represents hepatocytes, they are recognized as the remnant hepatocytes area. The rem-

nant hepatocytes area percentage is defined as the numbers of pixels that belong to the remnant hepatocytes area divided by total area.

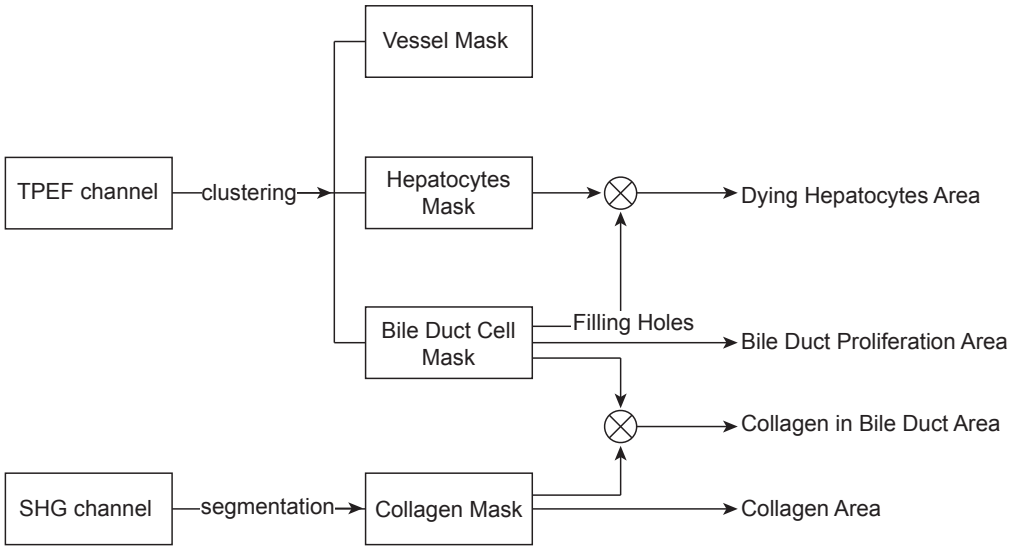

Figure 5. Flow chart of the feature extraction algorithms. TPEF and SHG two image channels were separated from the same imaging samples. The TPEF channel was then clustered into three separate masks by intensity difference, namely bright, dim and dark. The bright intensity area in the TPEF channel was classified as hepatocytes mask, the dim area was classified as bile duct cell mask and the dark area was classified as vessel mask including outside-tissue-space. Collagen mask in the SHG channel was obtained after segmentation performed on the images. The feature of total collagen area was then referred to collagen mask, and bile duct proliferation area to bile duct cell mask. Multiplying collagen mask and bile duct cell mask yielded the collagen in bile duct area feature. The remnant hepatocytes area feature was defined as clusters of hepatocytes that were surrounded by bile duct cells, therefore, we obtained it by filing holes of the bile duct cell mask, and then multiplying it by hepatocytes mask.

All image processing and algorithm computations were carried out in MATLAB (The Math Works, Inc, Natick). Image processing algorithm code is available for readers upon request.

4.3 Results and Discussions

4.3.1 Zebrafish liver specific gene identification

Zebrafish (*Denrio rerio*) has proven to be excellent vertebrate model organism for studying human biology and disease. The adult Zebrafish liver, similar to human, consists of two lobes and is surrounded by blood vessels. Besides the structural similarity, database mining results revealed that the majority of liver-enriched genes in Zebrafish share high homology with their mammalian counterparts, suggesting that the profile of liver-enriched genes in an adult Zebrafish liver is similar to that identified in mammals and other vertebrates [128, 129]. Due to its unique advantage of being fast in reproduction with large offspring in each generation, reverse genetics TILLING (Targeting Induced Local Lesions in Genomes) [130] is performed on Zebrafish in this study to identify a specific liver enriched mutant fish. Later, a mutant Zebrafish line can be constructed, and fibrogenesis model can be established by chemically treating the fibrosis-prone fish, also fibrogenesis in different stages of the life cycle of Zebrafish can be studied.

Out of the 129 genuine liver-enriched genes recently identified in Zebrafish that is regulated by Hepatocyte nuclear factor (HNF) factors [131], *hgf-like* gene (accession number NM_152980 in GenBank), which is co-regulated by HNF3, HNF4, HNF6 is chosen as the target gene for mutant screening in Zebrafish mutant library we constructed. This gene is chosen as it is closely related to Hepatocyte Growth Factor (HGF), which has a major role in embryonic liver development, in adult liver regeneration (reverse of fibrosis) and in

wound healing [132]. Deficiency in this gene is therefore expected to make Zebrafish more prone to fibrogenesis and hard for liver regeneration, an ideal fibrosis model for our study.

4.3.2 Mutant Zebrafish screening

For construction the cDNA Zebrafish mutant library, founder animals were mutagenized with ENU and 1056 healthy F1 male and female fish were raised and used to construct the library (Figure 6). Instead of conventional practice to generate a permanent resource by cryopreservation of sperm or testis samples, we maintained the library as a living resource that can be used for a limited time. The advantage of having a living resource is that, firstly, the cryopreservation of testis or sperm samples is labor intensive, taking several months to complete, whereas the construction of a living library only took weeks. Secondly, the success-rate for the recovery of fish carrying mutations from frozen testis samples by in vitro fertilization (IVF) turned out to be highly variable, in some cases resulting in loss of alleles.

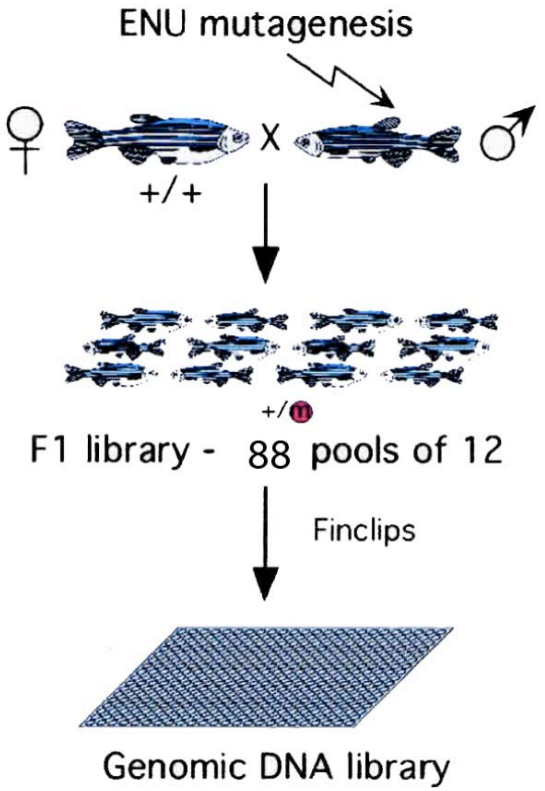

Figure 6. Male Zebrafish were mutagenized with ENU and outcrossed with wild-type females to generate a library of 1056 mutagenized F1 fish. Both males and females were finclipped and grouped in 88 pools of 12 fish per fish tank. DNA was isolated from the finclips and arrayed in eleven 96-well PCR plates.

PCR amplicons for *hgf-like* gene are designed from cDNA sequence. This sequence is used as input for GENOTRACE [133] to determine the genomic organization and retrieve noncoding sequences flanking the exons. As a result, three exons exsit for *hgf-like* gene, position of 4853-5621, 15743-17081, 24312-25603 from the genome DNA (Figure 7). Noncoding introns were used for primer design to amplify the coding exons. First and nested primers were designed accordingly for these cDNA fragments, however one amplicon is unable to amplify the cDNA. Failure of one amplicon is mostly likely due to the repetitive nature of the Zebrafish genome and the large amounts of single nucleotide polymorphisms.

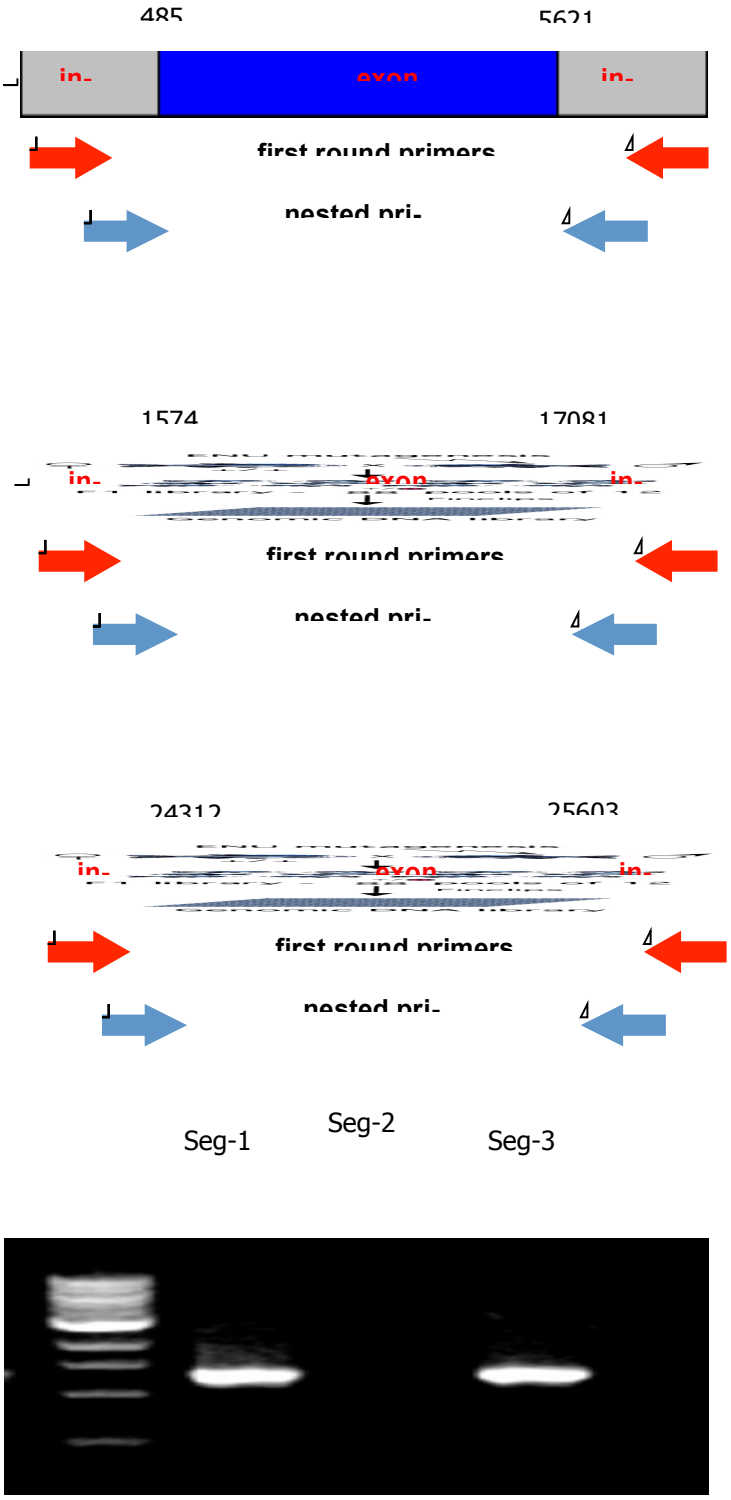

Figure 7. Amplicons design of *hgf-like* gene on genome DNA (gDNA) of Zebrafish. Three cDNA fragments were identified in gDNA, six pairs of primers (one pair of first round primers and one pair of nested primers for each exon) for exons were designed accordingly. Two exons can be amplified, while one exon cannot be amplied by the primers designed.

The four pairs of successfully designed primers are used for cDNA amplication and sequencing of the two exon fragments. Sequencing results are collected in e-form, with request to mark the base "N" when the lower peak is over 30% of the higher peak on the same base point position, which is a suspicious candidate of the mutation. After aligning all sequencing results together with standard gDNA in the database, dissimilarities are identified manually in the exons region. As demonstrated in Figure 8, suspicious point mutations are identified by the sequencing results. However, after redoing the first and nested PCR by tracing back the original gDNA samples and sequenceing the PCR products, it confirmed that all the suspicious mutations screened earlier on were not real mutation.

Figure 8. cDNA sequencing results from *hgf-like gene* of mutant Zebrafish against normal genome DNA. Suspicious point mutant is marked with N in the sequencing results, as shown by red arrow.

It is expected that ENU mutagenesis is random for coding and noncoding sequences. With coding region is much smaller than the noncoding region, the chance that the coding exons are mutanted is quite small. In general, the success rate of both forward and reverse mutagenesis screens is mainly dependent on two factors, mutagenesis efficiency and the number of individuals screened. To find loss-of-function mutations in target genes, both factors should be as high as possible. In our experiment design, only 1056 Zebrafish were used to construct the library, which is insufficient compared with other groups [134, 135]. That would account for the unsuccessful screening of the desired gene in the experiment.

After the unsuccessful screening of *hgf-like* mutant Zebrafish, we stopped the direction of building a liver fibrosis model on fish. Since our Zebrafish library is not big enough for mutant screening and drug induced fibrosis in fish is not very obvious (proved by previous labmates, data not shown), the feasibility of building a fibrotic model on Zebrafish is low in the short period. Therefore, we move on to build the fibrotic model on rats, a common mammal model.

4.3.3 Rat BDL model fibrosis staging

Hepatic fibrosis induced by Bile Duct Ligation (BDL) is the primary pathological lesions occur surrounding the bile duct epithelium. The maneuver of BDL introduces biomechanical stress to biliary epithelium and initially triggers the compensatory proliferation and expansion of biliary epithelial cells (BECs) [136, 137]. Following this epithelial mitogenic phase, chronic obstruction of bile duct causes massive activation of myofibroblasts in the periductal region

and ultimately results in biliary fibrosis/cirrhosis. It is an established animal model that simulates the progression of Primary Biliary Cirrhosis (PBC) [138], which is characterized by destruction of interlobular and septal bile ducts leading to chronic cholestasis, cirrhosis and hepatic failure [139]. The disease progression is also similar to Biliary Atresia (BA), the most serious digestive disease affecting infants, caused by obstruction of bile flow [140, 141]. Considering the surgical difficulties in operation on small animals, we established the BDL surgical model on rats to induce liver fibrosis. As shown in Figure 9, liver of BDL rat is distinguishable from normal liver, as BDL livers are larger in size after surgery and appear to have less blood flow within the organ. The surface of the BDL liver is rough compared with the smooth liver surface from the normal rat, a clear indicator of presence of liver fibrosis. The bile duct is easily identifiable in the BDL rat, indicating the success of inducing fibrosis through bile duct ligation.

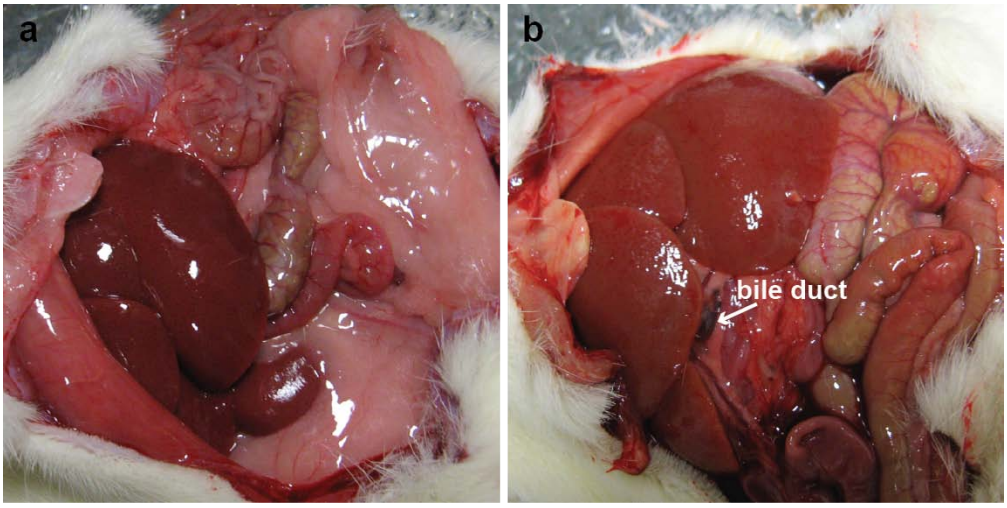

Figure 9. Normal rat liver and rat liver after Bile Duct Ligation (BDL). 4 weeks after bile duct ligation, rat liver (b) is larger than normal liver (a), caused by hyper pressure from bile flow within the liver and the proliferation of biliary epithelial cells (BECs). Less blood flow is also present is the BDL liver evident by lighter liver color (b) compared with normal liver (a). Due to pressure caused by ligation, bile duct thick-

ens, making it easily identifiable after BDL (b). Liver surface also roughens after BDL.

After extracting the liver samples, tissue blocks from both left and right lobes were prepared. Two successive slices cut from the same tissue block were separately stained with Masson's Trichrom and Sirius red. Comparing different staining results from the same sample can therefore help with identification of morphological changes based on feature extraction and reduce variations of fibrosis staging. Figure 10 shows the same sample with two different stainings. With both Sirius red and Masson's Trichrome, we can clearly identify hepatocytes and collagen near the blood vessels and ECM (arrows in Figure 10 a and b).

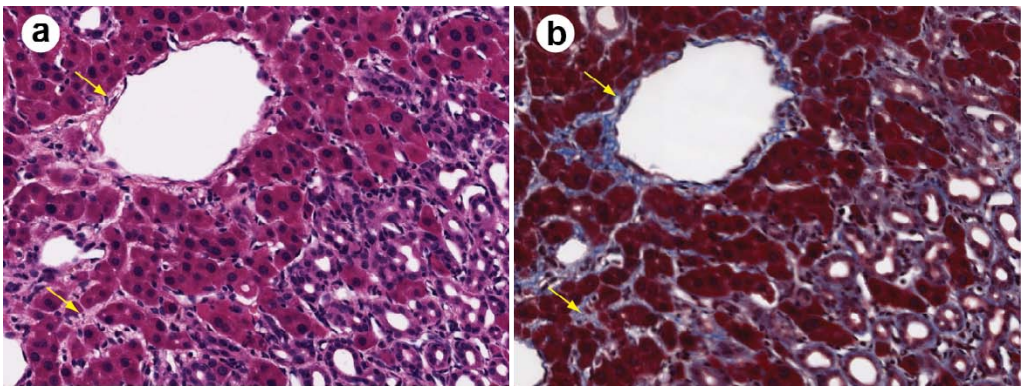

Figure 10. Sirius red staining (a) and Masson's Trichrome staining (b) of the same fibrotic BDL liver tissue. In Sirius red staining (a), hepatocytes were stained dark red, and collagen of light red in pale yellow background. In corresponding Masson's Trichrome staining, hepatocytes were stained dark red with nuclei black, and collagen of blue. Collagen near blood vessel and in ECM can both be observed in the two staining indicated by yellow arrows.

After staining all the liver samples, samples were sent to pathologists for reading and staging based on modified Ruwart scoring [124, 142]. Figure 11 shows changes in collagen using Masson's Trichrome staining of different stages in our samples. In normal livers, hepatocytes were healthy and presence

of collagen was minimal, mainly around blood vessels [Figure 11(a)]. As liver progressed in the animal models, stage 1 fibrosis with an increase in pericellular collagen without formation of septa was evidenced [Figure 11(b)]. With the continuous progression of liver fibrosis after BDL, disuse loss of hepatocytes and significant bile duct proliferation was observed. Stage 2 collagen aggregations also formed incomplete septa from the portal tract to the central vein [Figure 11(c)]. Stage 3 moderate liver fibrosis was characterized by bile duct proliferation, biliary ductular hyperplasia, diffuse loss of hepatocytes and occasional small foci of mature collagen. In Figure 11(d), complete but thin collagen septa interconnected with each other to divide the parenchyma into separate fragments in stage 3 fibrosis. Stage 4 severe fibrosis was mostly evidenced by massive hepatocytes loss, substantial biliary ductular hyperplasia and severe diffuse fibrosis. Thick collagen septa were observed, forming complete cirrhotic nodules in Figure 11(e). Here unique to BDL model was the amount of bile duct proliferation and collagen aggregation around the bile ducts, the dimmer red regions in Masson's Trichrome staining. Although Masson' Trichrome staining is regarded as the gold standard in a typical pathology laboratory for clinical diagnosis of liver fibrosis [143], the color of the staining is not uniform across all the samples as shown in the figure, therefore making it lack of objectivity for quantifications.

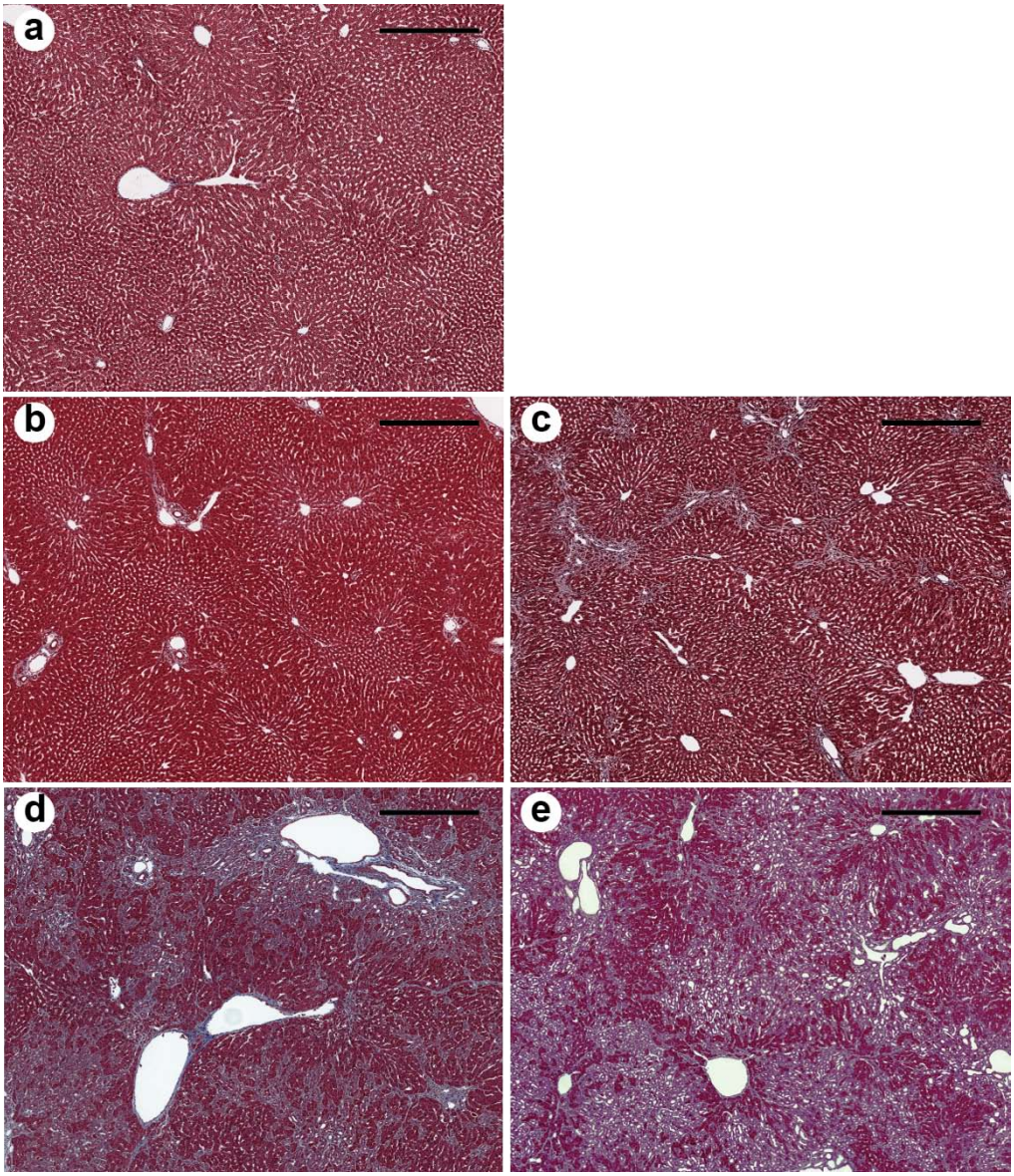

Figure 11. Morphological changes at different stages (b-e) of liver fibrosis compared with normal liver (a) recorded with conventional Masson's Trichrome staining. Normal liver (a) has minimal presence of collagen in the tissue, and mainly around blood vessels. In stage 1 liver fibrosis, there was presence of pericellular collagen without the septa formation in (b). In livers with stage 2 fibrosis (c), collagen aggregations formed incomplete septa from the portal tract to central vein, the bile duct proliferation was seen as dim red regions in the image. For stage 3 liver fibrosis (d), profuse bile duct proliferation was observed all over the tissue sample, where complete but thin collagen septa interconnected with each other. In stage 4 fibrosis (e), thick collagen septa were observed, forming complete cirrhosis. All scale bars are 500 μm.

4.3.4 Image acquisition from prepared samples

Two sample preparation methods for SHG/TPEF imaging were tried out to compare the image qualities. As shown in Figure 12, images scanned based on SHG/TPEF imaging were presented, with red color in both images representing the cells in the liver tissue, mainly hepatocytes, green color representing collagen type I. Different red color represents different cell types in the liver, as the auto-fluorescence from different cells types have different excitation wavelength. Areas containing nucleus, lipid droplets and vacuoles formed by degenerated hepatocytes appear dark as they are lacking of fluorescent molecules in such areas. Comparing Cryosection prepared samples with paraffin embedded section prepared samples [Figure 12(b)], we can see that although even finer collagen (green) can be both picked up in these two images, cell morphology is much clearer in the image with paraffin embedded section [Figure 12(b)], while in Cryosection samples [Figure 12(a)], cells are lacking of clear boundary, also there appear to be more small black holes in the sample. We suspect, during Cryosection, the freezing step made water in the cells expand in volume, therefore when defreezing, pressure from within the cells expanded the cells, and finally broke them. That caused the changing of morphology and the big holes in the samples. After the comparison, we have decided to only include the paraffin embedded sections for imaging and for late image analysis.

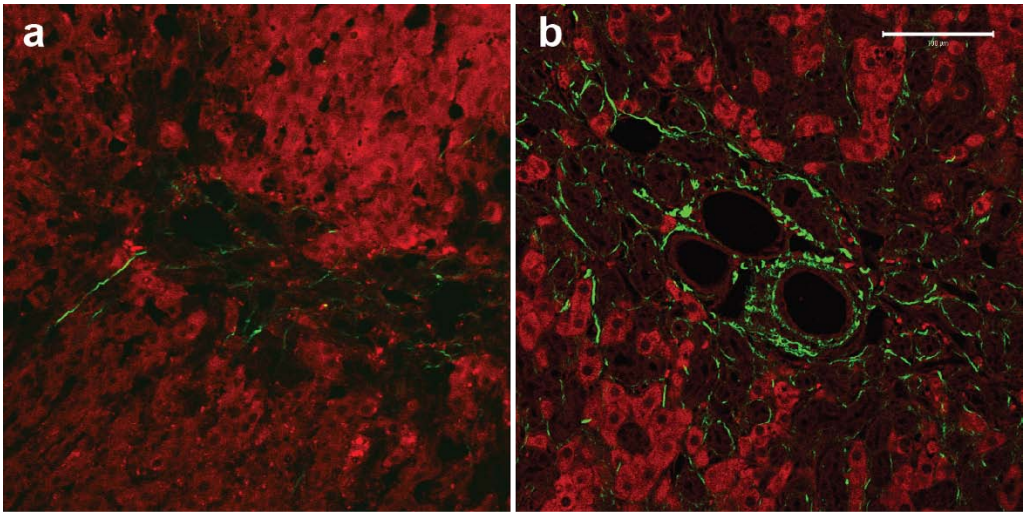

Figure 12. Comparison of SHG/TPEF images from Cryosection (a) and paraffin embedded section (b) preparation. In both 20x images, SHG is shown in green, representing type I collagen and TPEF is shown in red, representing liver cells. In Cryosection prepared sample (a), the cell morphology is less clear than the paraffin embedded section (b), also there are small black holes in the tissue sample which are not visible in paraffin embedded one. In both images, SHG signals are very strong, being able to pick up fine collagen fibers in the tissue samples. Scale bar is 500μm.

After confirming to use only paraffin embedded section samples for SHG/TPEF imaging, three tile scan images (4096×4096 pixels, ~2mm×2mm each) were taken from each tissue specimen, and two specimens were extracted from each animal (from both left and right lobe of the liver). In the tile scan image [Figure 13(a)] from fibrotic liver tissue, larger area of the tissue block as covered, and more structures such as portal tracts and central veins were revealed. The detailed image [Figure 13(b)] showed that the morphology of the liver tissue is clearly visible, with hepatocytes shown in light red color and black dots in the cells representing nuclei. Separating the overlay image into TPEF [Figure 13(c)] and SHG [Figure 13(d)] channels, we can identify that thick collagens (in green color) in the center of the figure are around the blood vessels, matching the standard morphology structure of the liver tissue. Also, thin collagens along hepatocytes were clearly visible, making this image mo-

dality sensitive to abnormal collagen during fibrogenesis. The dark red regions in the images where clear hepatocytes morphology was not indentified were suspected to be filled with Biliary epithelial cells (BECs), as our BDL model is likely to cause profuse proliferation of bile ducts. This will be proved further when comparing with gold standard stained liver tissues.

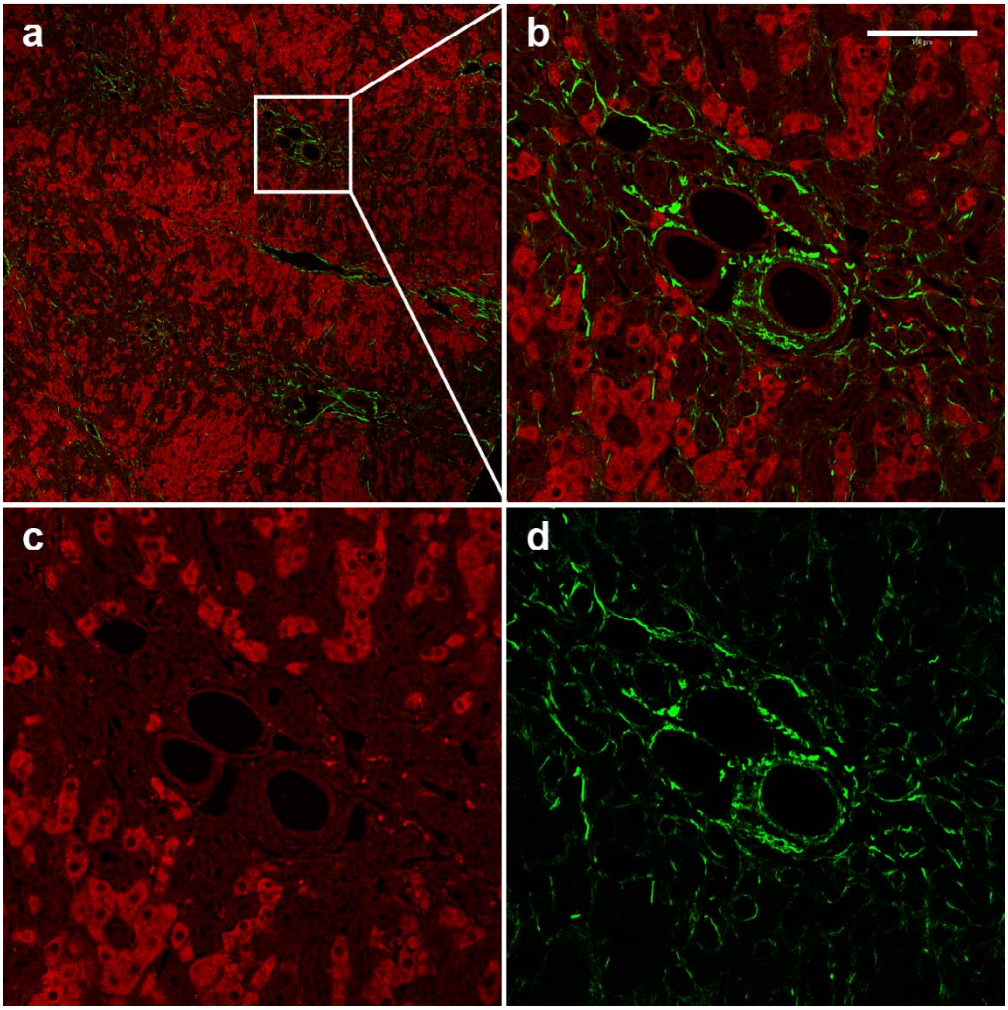

Figure 13. Images of liver tissue from SHG/TPEF image modality. Tile scan image (a) (4096×4096 pixels, ~2mm×2mm) was taken from paraffin embedded section tissue slice. Detailed overlay image (b) showed that liver morphology is clearly identifiable, and signals from both TPEF channel (c) and SHG channel (d) overlay perfectly to reveal the liver structure. Thick collagen around blood vessel and thin collagen along hepatocytes match the standard structure of a BDL fibrotic liver. TPEF signal is in red, and SHG signal is in green, scale bar is 100μm.

4.3.5 Comparison between SHG/TPEF and conventional histological images

To compare SHG/TPEF imaging modality with the conventional stained tissue imaged under wide filed, images from the same location taken from two different image modalities were compared as shown in Figure 14. Both images revealed the same morphology in the tissue, with collagen shown in blue and hepatocytes in red in Masson's Trichrome image and collagen shown in green and hepatocytes in red in SHG/TPEF image. The pink color stain in Masson's Trichrome image represented biliary epithelial cells, correspondingly, in SHG/TPEF image, they were shown in dark red color. Both images also clearly demonstrated collagen aggregation around vessel walls and inside the sinusoids. In Figure 14, however, there seem to be more blue color in Figure 14(a) than green color in Figure 14(b). That is because SHG signal can only show type I collagen fibers, while in the stained tissue, all types of collagens were stained in blue. However, to use stained samples for quantification, there lies a particular challenge, as it is difficult to produce uniform interbatch shares of the three colors involved in Masson's Trichrome staining. In addition, in Masson's Trichrome staining, both green and blue colors can be used to stain collagen in the tissue, causing nonreproducible results when used as a quantitative measures of fibrosis progression. Therefore, using SHG/TPEF image modality can truthfully reveal the morphology of the liver tissue structure and the collagen distribution, making it a sound methods for quantitative measures of fibrosis progression.

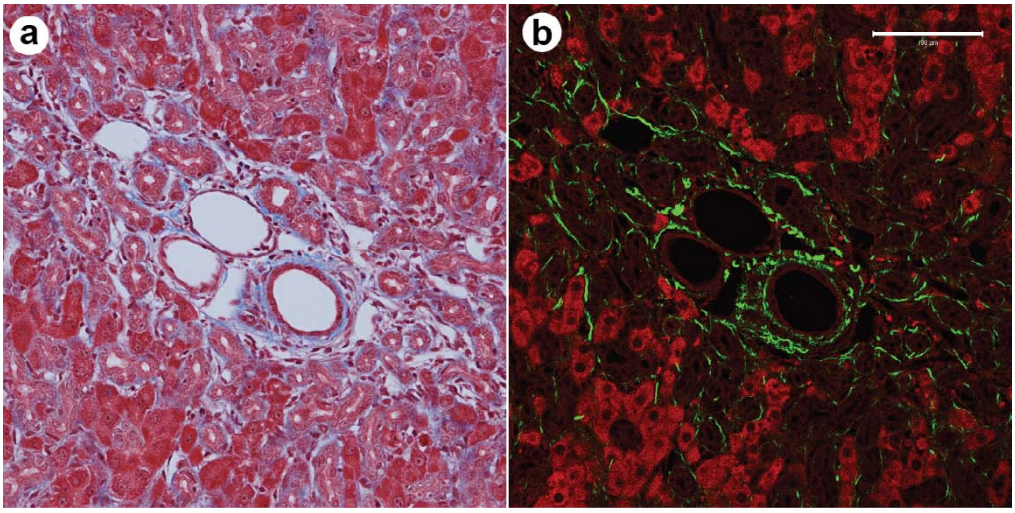

Figure 14. Comparison between Masson's Trichrome stained tissue image and SHG/TPEF image. White field transmission image of a fibrotic tissue sample stained with Masson's Trichrome (a) and SHG/TPEF image (b) of the same sample before staining were compared. The overlay of the image confirmed that SHG/TPEF image can present the liver tissue morphology and collagen distribution faithfully. The light red color in both (a) and (b) images represents hepatocytes, and pink in (a) and dark red in (b) represent biliary epithelial cells, and green in (b) represents collagen corresponding to blue in (a). Both collagens around the vessel wall and in sinusoids can be detected in (b), making SHG/TPEF a comparable imaging modality to reveal tissue structure.

4.3.6 Comparison among different image segmentation methods

To truthfully extract information from SHG/TPEF images, especially the vital features, such as the presence of collagen in the liver organ, different image segmentation methods were employed.

In our search for the optimal method to segment fibril collagen from the background, four different methods were employed, namely Otsu thresholding, K-means clustering, Fuzzy-C means clustering (FCM) and expectation maximization (EM) algorithm based on Gaussian mixture model (GMM). They each represent a typical image segmentation method group. Otsu method is a classic global thresholding algorithm, which aims to find the best threshold to minimize intra-class variance and maximize the between-class variance. The

K-means clustering is one of the most popular and iterative clustering methods for image classification. The Fuzzy-C means clustering method works similar to K-means clustering while assigning each pixel in the image a degree of belongingness (membership) to clusters rather than strictly assigning to one cluster. It handles the uncertainty in the data. The Gaussian Mixture Model (GMM) method assumes that the distribution of intensities is a mixture of several Gaussian distributions, each corresponding to a separate tissue class. Using Expectation Maximization (EM) algorithm, it is assumed that the intensity of pixels in the SHG image can be modeled as the mixture of two Gaussian distributions, one representing collagen area with strong SHG signals and the other representing the background.

The segmentation results using different segmentation methods are shown in Figure 15. Figure 15(a) is the original SHG image as captured by microscope, Figure 15(b-e) represents the segmentation results from Otsu, K-means, Fuzzy-C means and GMM respectively. As shown in the results, Otsu, K-means and Fuzzy-C means can segment most of the thick collagen from the images, however, the dim and finer collagen fibers cannot be picked up by the three methods. Using Gaussian Mixture Model (GMM), on the other hand, can achieve better segmentation results compared to the other methods by capturing finer collagen while incurring minimal noise in the image. Based on the results we have obtained, we concluded that GMM is a better segmentation method for the purpose of extracting collagen fibers in the SHG images. Therefore, we continued to use this method on all the SHG image segmentation.

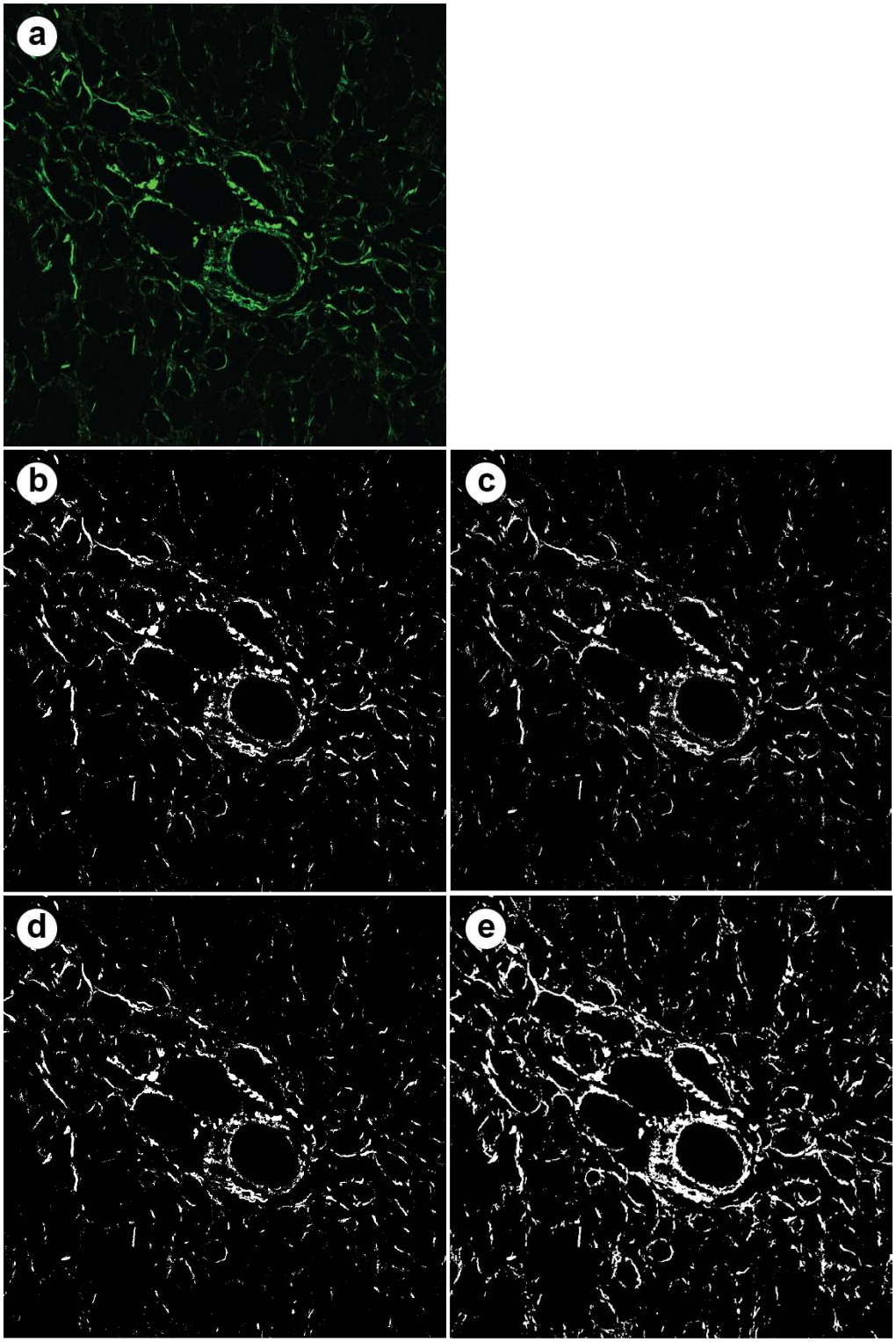

Figure 15. Segmentation results of SHG image using different methods. (a) Original SHG image, (b) segmentation results using Otsu method, (c) K-means clustering method, (d) Fuzzy-C means clustering method and (e) Gaussian mixture modeling.

4.3.7 Image analysis and feature extraction of SHG/TPEF images

To stage liver fibrosis, different features within livers were extracted and quantified accordingly. In the TPEF channel, liver cells were separated into hepatocytes, which were marked as light red color in the image (Figure 16(b)), biliary epithelial cells, the dark red color in the same image. The segmentation of TPEF channel was done by using Fuzzy-C means, which classifies the TPEF image intensity into three different groups, the bright, the dim and the dark. An image mask was created on both the bright and the dim intensity category, which represents the hepatocytes (not shown) and bile duct area (Figure 16(d)) respectively. The goodness of this segmentation method was verified by pathologist-assisted color segmentation performed on Masson's Trichrom stained tissues, the detail of which is shown in the next point. After segmentation of both SHG and TPEF channel images, the biliary epithelial cell content (Figure 16(d)) was then quantified as percentage of the total area in the images, marked as bile duct area. Total collagen in the images was quantified as the percentage of the collagen in the area (Figure 16(c)), also as collagen percentage in the bile duct area (Figure 16(e)). Some hepatocytes in the tissue were further quantified as percentage of remnant hepatocytes (Figure 16(f)) defined as small clusters of hepatocytes that were surrounded by the bile duct cells. In all, 4 types of features were extracted from each image taken from liver tissue: total collagen content in the tissue; bile duct area; collagen content in the bile duct area, representing the abnormal and destructive ECM distribution in the BDL disease model; and finally, the remnant hepatocytes, representing the potential necrotic and apoptotic hepatocytes that were caused by the disease progression.

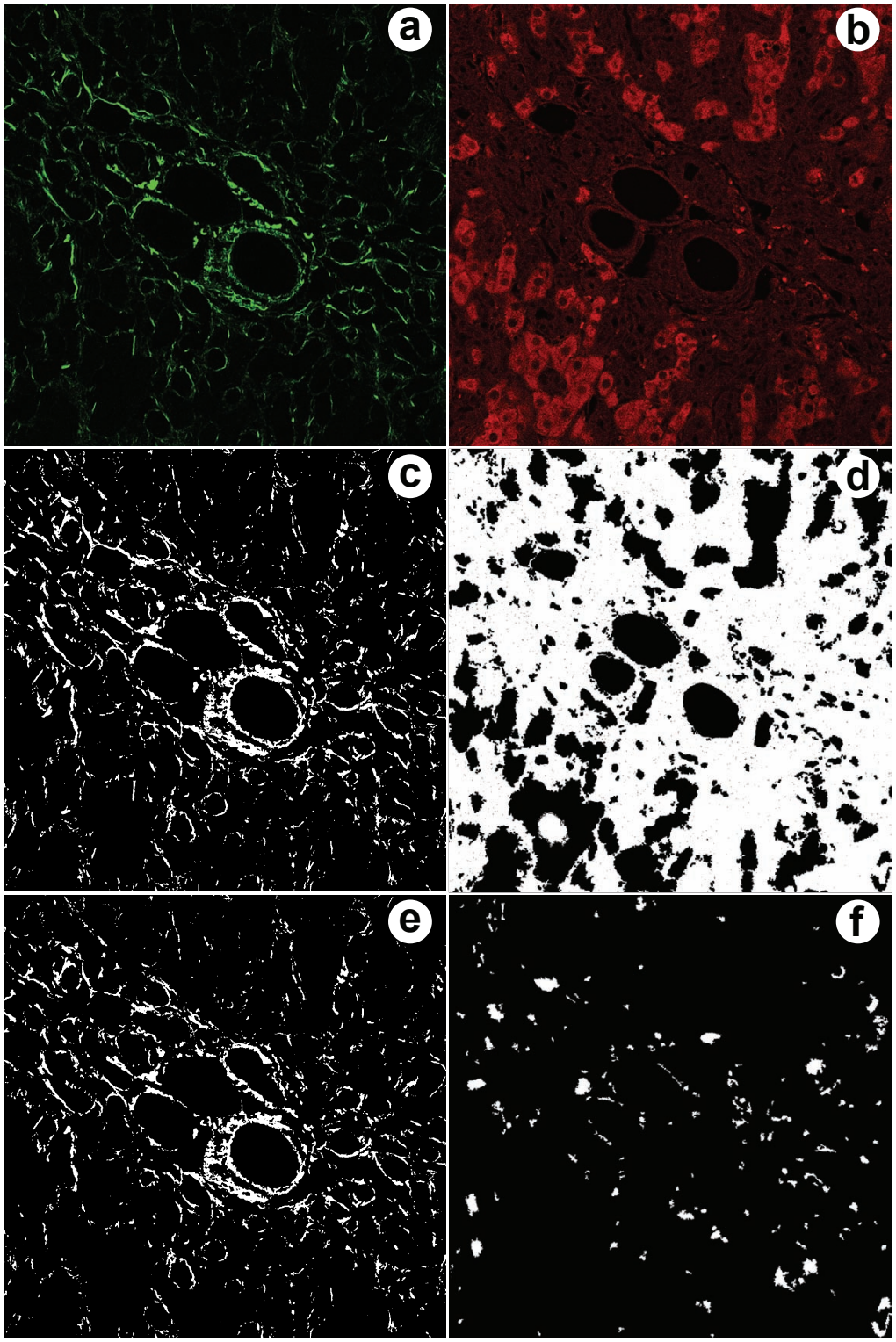

Figure 16. Process of feature extraction from SHG/TPEF images. Images from SHG (a) and TPEF (b) channels were separated from the same combined image. After segmentation of both channel images, collagen content in the whole area (c) and bile duct areas (d) corresponding to the dark red region in (a) was quantified. Collagen content in the bile duct area (e) was also quantified as the abnormal, destructive ECM in the region. Remnant hepatocytes (f), defined as small clusters of hepatocytes that

were surrounded by the bile duct cells, were also quantified as potential necrotic and apoptotic hepatocytes.

4.3.8 Validation of feature extraction of SHG/TPEF images

To validate the goodness of the image segmentation performed, the segmentation results are compared to the semi-automatic segmentation performed on the Masson' Trichrome stained tissues, in which color segmentation were performed, and verified and hand corrected by pathologist.

Masson' Trichrome stains collagen blue, cytoplasm red and cell nuclei dark brown. Based on this color information, we segmented the MT stained tissue into two channels as shown in Figure 17, one containing blue collagen (Figure 17(b)), and the other containing red cellular information (Figure 17(c)). In the cellular channel, we further segment the cell types based on the color difference, with hepatocytes stained in dark red and bile duct cells in light red. Depends on the precision of staining process, the color difference between different cell types might not be clear enough for the automatic color segmentation. Hence, after segmentation of the image based on pixel color information, we consulted the pathologist, and did a second round of manual segmentation to ensure the accuracy of the results. Since manual reading of the histopathological staining tissue is still the gold standard in current clinical practice [3], this manual segmentation is a critical step for conventional fibrosis assessment.

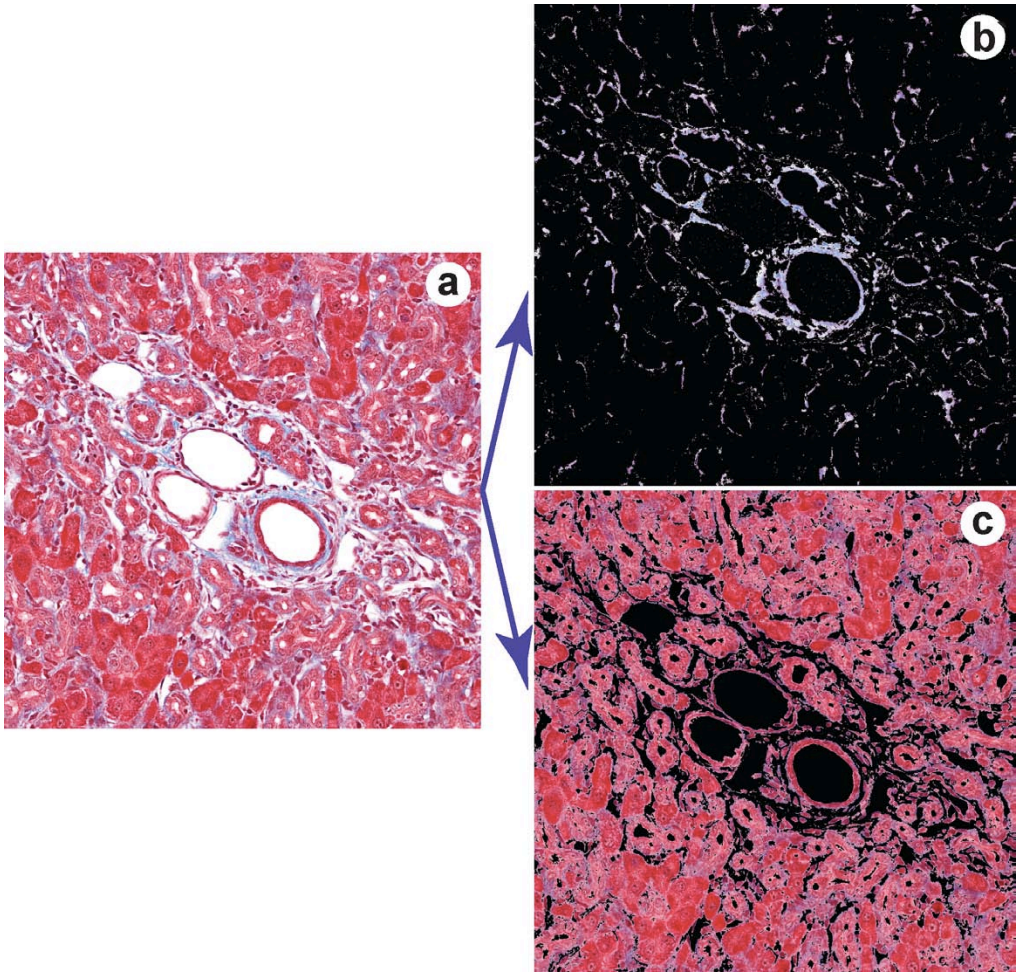

Figure 17. Masson's Trichrome image segmentation. Masson's Trichrome image (a) taken from a white light microscope is segmented based on color information into two channels. Blue color in the image representing collagen is segmented into channel (b), while red color representing all the cell types is segmented into channel (c).

To validate the accuracy of the segmentation methods we employed in this thesis study, segmentation of both MT image and SHG/TPEF image was compared for the same tissue sample for respective features shown in Figure 18. Figure 18(c, e, g) shows the pathologist-assisted segmentation of collagen, hepatocytes and bile duct cells respectively done on the MT image (Figure 18(a)), while the corresponding SHG/TPEF image segmentation is shown in Figure 18(d, f, h). Judging from the images shown, our automated image segmentation simulate very closely on the pathologist-assisted method. And to prove this in a quantitative manner, same 100 random regions with size 1/100

of the image displayed in the corresponding segmented images were chosen. Percentage of the segmented features were calculated, and compared between two different segmentation methods. The results are shown in Figure 19. Scatter plot indicates that among three features we segmented, they all have close correlation with the pathologist-assisted results. Correlation coefficient R calculated in the Figure 19 also suggests that this correlation is statistically significant ($p<0.01$), and that we can proceed with the feature quantification based on these segmentation methods we employed.

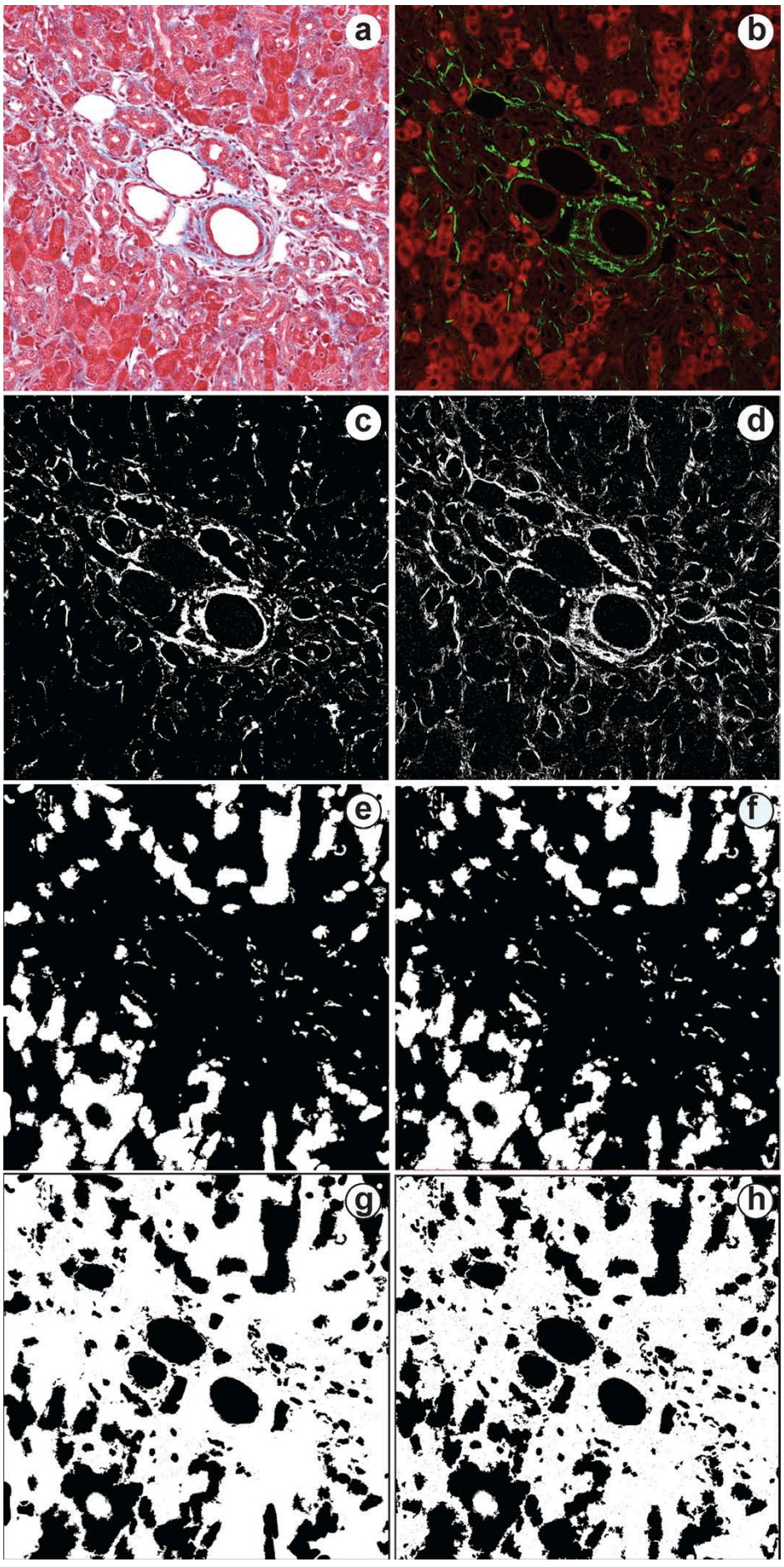
a
b
c
d
e
f
g
h

Figure 18. Masson's Trichrome and SHG/TPEF image features segmentation comparison. Masson's Trichrome image (a) and SHG/TPEF image (b) from the same tissue sample are obtained and segmented based on pathology-assisted color segmentation and automated segmentation respectively. (c), (e), (g) represent collagen, hepatocytes and bile duct segmentation from MT image (a), while (d), (f), (h) represent the same features from SHG/TPEF image (b).

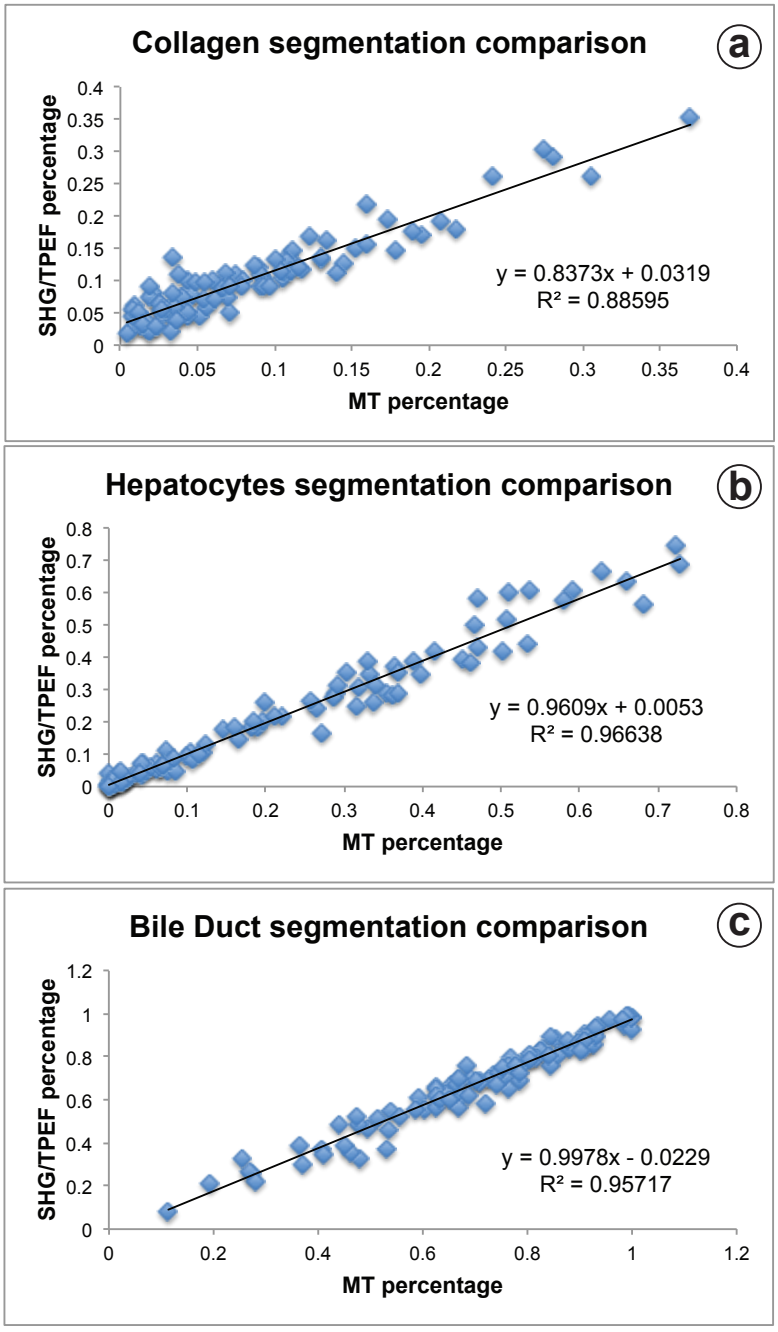

Figure 19. Segmentation results comparison. Based on the feature percentage calculated from the 100 random regions in the image, scatter plots of the same feature between two different segmentation methods are shown. (a), (b), (c) show the plot of collagen, hepatocytes and bile duct segmentation respectively. Correlation coefficient of the linear relationship between these two segmentation methods are indicated in the plots, suggesting statistical significance of the segmentation results similarity.

4.3.9 Quantification analysis of liver fibrosis

Based on the features extracted on SHG/TPEF images, each feature was quantified as the area percentage of such feature presented the images. X-axis represents time after bile duct ligation, which is the time course of fibrosis progression, with week 0 representing the normal liver tissues. As shown in the quantification results below, with the increase of liver fibrosis progression, there is an increasing amount of collagen in the liver tissue. With the tremendous increase of bile duct area in the liver tissue, collagen distribution in the bile duct region (abnormal collagen) also increased. All these three features show significant difference among different time points after Bile Duct Ligation ($p<0.01$). Potentially remnant hepatocytes also increased in percentage in the liver tissue. However, although significant difference ($p<0.01$) showed in early development of fibrosis progression (among week 0, 2, 4), increase between week 4 to week 6 is not statistical significant. It could mean that at the late stage of fibrosis progression, since mass necrosis and apoptosis occur in the liver, the potentially remnant hepatocytes are not increasing as much as in the early stages. Also the difference between total collagen in the tissue and the collagen distributed in the bile duct areas (abnormal collagen) remains stable across all time points, suggesting that the fibrosis progression has not much influence on the distribution of normal collagen in the tissue.

In all, based on the four features extracted, we can quantitatively monitor the fibrosis progression in time. Each feature can be used separately as the clear indicator of the disease progression.

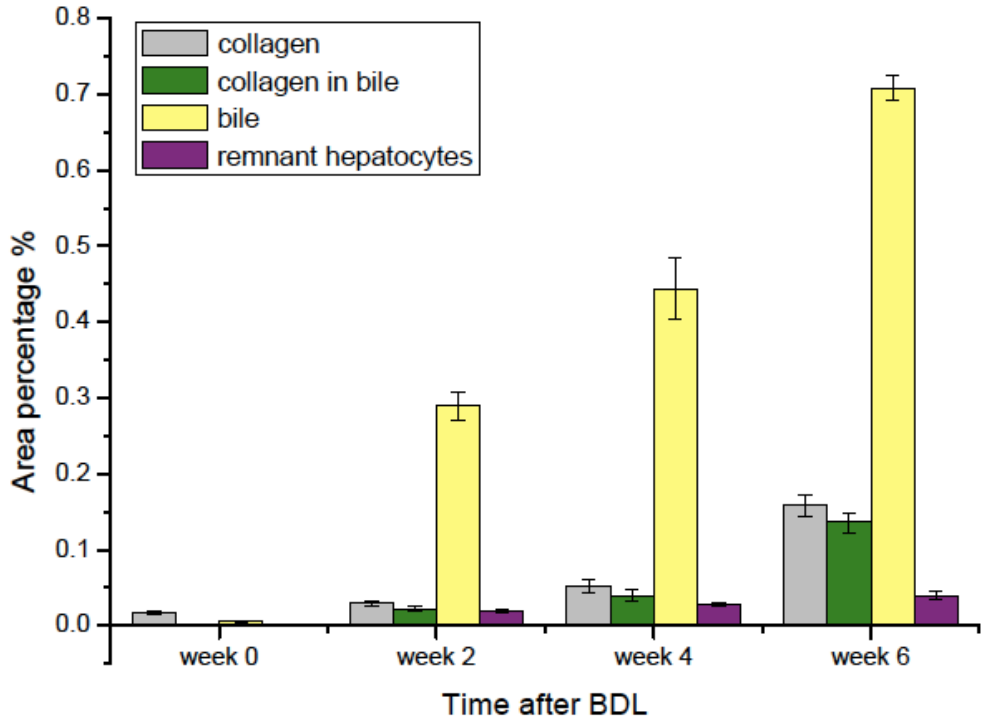

Figure 20. Quantitative analysis results of features extracted in SHG/TPEF images. Four features, collagen: collagen content in the tissue, collagen in bile: collagen content in the bile duct region, bile: bile duct region percentage in the tissue, remnant hepatocytes: potentially remnant hepatocytes content in the liver tissue were quantified as percentage of such features in the liver tissue in the images. At different time points after bile duct ligation, all features showed a trend of area percentage increase in the images with significant significance ($p<0.01$) among all time points except for remnant hepatocytes between week 4 and week 6.

In order to see if such quantitative assessment agrees with the traditional qualitative histopathology staging, we prepared samples in Masson's Trichrome staining and asked a pathologist to give each of those tissue samples a numerical score based on the severity of fibrosis (Metavir scoring system, 0 represents no fibrosis, 4 represents Cirrhosis), known as the 'gold standard' for liver fibrosis staging. Since both left and right lobes were extracted from the same rat, and each lobe is prepared into one tissue sample for the pathologist's staging, and four rats in each time group, the final histopathology score of each time point is an average score of all the tissues staged. As shown in Figure 21, using the same x-axis as in Figure 20, with the progression of

liver fibrosis in time, the severity of the disease progresses, with the same increasing trend of all the quantitative features we extracted early on. Therefore, we confirmed that the quantitative assessment of liver fibrosis based on the information from SHG/TPEF images could represent the real disease progression in sample, with a quantitative nature.

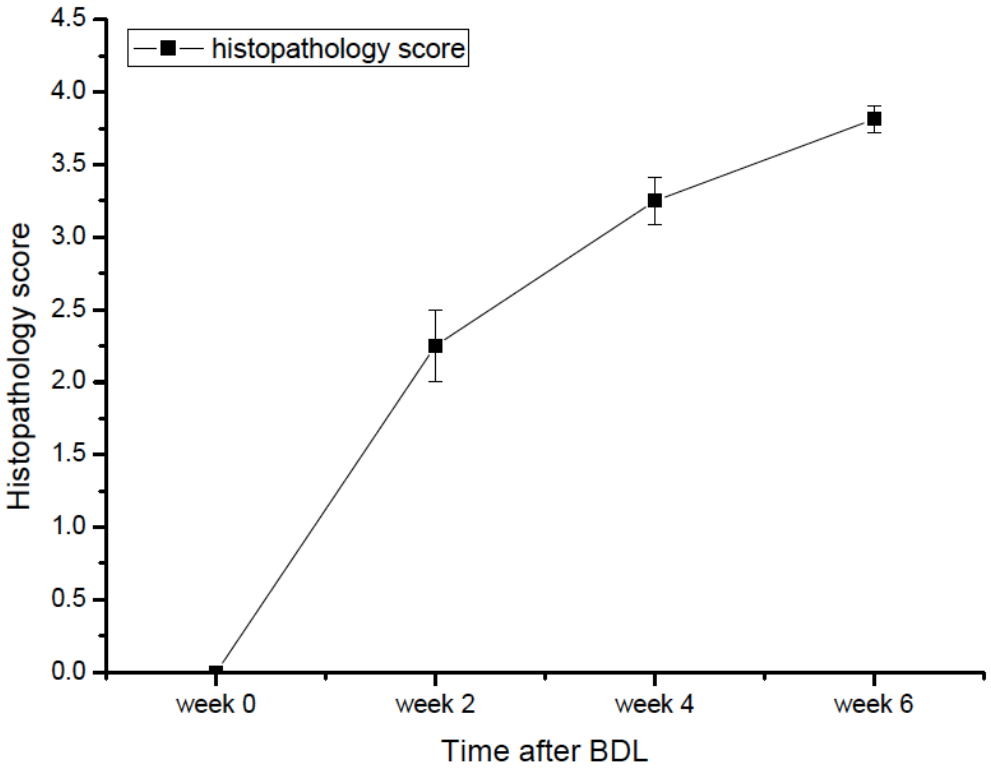

Figure 21. Histopathology scoring results of liver tissues. At different time points after performing bile duct ligation, liver tissues were scoring based on Metavir scoring system, with numerical results of 0, 1, 2, 3, 4 only. Values shown are averaged over all tissue samples at the given time point, showing liver fibrosis severity increase over 6 weeks. ($p<0.01$ among all time points)

4.4 Conclusion

We have established a reliable rat bile duct ligation (BDL) model for liver fibrosis study, in which liver fibrosis progress with time after the induction of the disease. With the digitized images we took from SHG/TPEF microscopes, four morphological features were extracted from liver tissues, allowing for quantitative assessment of the features. We therefore developed and validated a standardized quantification system in liver fibrosis assessment based on the features extracted. We further demonstrated the feasibility of our SHG/TPEF microscopes in monitoring liver fibrosis progression with the BDL animal model by comparing with the conventional 'gold standard' histopathological scoring system. With the fast tissue preparation process compared with the traditional staining preparation, and the quantitative and standardization nature of the SHG/TPEF imaging modalities, our assessment system allows for future application of SHG/TPEF microscopies in diagnosis and prognostication of disease complications. By incorporating the morphological features with strong biological meanings in the tissue samples for quantification, we can also minimize the intra- and interobserver discrepancies by providing standardized features that are widely accepted by pathologist for staging.

Chapter 5 Towards Surface Quantification of Liver Fibrosis Progression

5.1 Introduction

Liver fibrosis is a wound healing process in response to various toxic injuries, and associated with almost all chronic liver diseases [1, 2, 24]. Inflammatory responses and excessive deposition of extracellular Matrix (ECM) are often observed with cirrhosis marking the end stage of fibrosis that represents the major causes of morbidity and mortality worldwide. There is increasing evidence that fibrosis is treatable and reversible in its early stages [144-147]; and even cirrhosis can regress in some clinical studies [148]. Therefore, accurate staging of liver fibrosis is of paramount importance to determine the state of disease progression, responses to therapy and optimization of treatment to direct disease management [44].

Currently, researchers have reported many noninvasive methods to assess liver fibrosis. Putative serum markers of fibrosis have been evaluated for the assessment, with indirect markers including serum aminotransferase levels [149, 150], presence of coagulopathy and platelet counts [151-153] that reflect alterations in hepatic functions; and markers including laminin [154], cytokines [155], collagens [156], matrix metalloproteinase and tissue inhibitors of metalloproteinases [157, 158] that reflect serum ECM deposition and turnover. Although some serum assays have been developed to diagnose significant fibrosis and cirrhosis with accuracies [159-161], none of them has been validated as a surrogate marker to stage fibrosis due to low sensitivity or non-specificity

[56]. Radiological imaging and novel imaging modalities such as ultrasonography [162], transient elastography [163] and magnetic resonance elastography (MRE) [60, 164] that based on liver stiffness measurements (LSM) have been shown to be reliable tools to assess liver fibrosis with quick and good reproducibility, but the sensitivity is also less satisfactory with current studies.

Percutaneous liver biopsy still represents the gold standard for the diagnosis and assessment of liver fibrosis. However, the potential complications following liver biopsy, and inherent drawbacks such as the invasive nature of the procedure, sampling error and inter- and intraobserver variability in the interpretation of the needle biopsy results have discouraged routine practice [4, 5, 48-50]. In addition, it is impractical to perform serial liver biopsies to accurately determine the changes of disease progression or to monitor the treatment effects.

To specifically and accurately monitor liver fibrosis in a quantitative manner, information extracted has to be directly compared to morphological features recognized by histological examination of liver biopsies' samples. Imaging on the liver surface, especially over a large sampling area than from biopsy, would therefore give us the potential to extract enough information over a long period of time, without the complication brought forth by the invasive biopsy. Laparoscopy has been attempted to diagnose cirrhosis by surface scanning to detect presence of nodules and the hardening of the tissue [165, 166]. However, with a thick layer of capsule around liver organ, traditional imaging technology can only focus on the capsule layer without penetration

into the tissue, making it hard for laparoscopy to extract quantitative information based on histological information that is comparable with biopsy samples.

In recent years, SHG microscopy has been increasingly used to measure structural protein such as neuron, muscle and collagen in biological samples with special structural properties [79-81, 167]. As a non-linear optical process, SHG exhibits intrinsic advantages over conventional fluorescence by requiring no fluorophore presence in tissue; therefore signals are not affected by dye concentration and photobleaching. Deeper tissue penetration can also be achieved by using infrared-range excitation source, resulting in less scattering in tissues than that in visible wavelength range [112-114, 116, 168]. SHG has been applied for assessing fibrosis by quantitative measurement of collagen in various organs [13, 81, 115], including livers [82, 118, 119, 169]. The results obtained using SHG/TPEF are standardized, highly reproducible and can monitor the progression and distribution of collagen at all stages of liver fibrosis with agreement with pathological readings [118, 169].

To incorporate such properties of SHG and TPEF imaging modalities for potential liver surface scanning to overcome the current drawbacks from laparoscopy, it is important to assess whether the SHG/TPEF based methods can extract surface information that reflects the whole organ, especially the interior that biopsy samples are usually obtained. The surface distribution of liver fibrosis features also needs to be examined to direct future scanning area on the liver surface. Therefore, fully automated quantification algorithms were developed in this chapter to extract morphology-based features from both liver

surface and the interior of the organ. Analysis of these features was performed to compare with the gold standard (histopathological scorings) to validate features, and then to study the representativeness of surface area to the liver interior. We observed that liver anterior surface on both left and right lobe contain similar information as in the liver interior when imaged and extracted using SHG/TPEF imaging modalities for fibrosis analysis. This establishes the foundation for future development of laparoscopic non-linear optical methods to serially quantify liver fibrosis on liver surfaces to eventually eliminate the need for invasive liver biopsy.

5.2 Materials and Methods

5.2.1 Rat BDL model sample extraction for surface study

Bile duct ligation (BDL) of rats was performed as described in Chapter 4. Cardiac perfusion with 4% paraformaldehyde was performed to flush out blood cells and fix the liver tissue before harvesting. To explore the surface information in the liver, sample extraction from liver tissue was performed so that the surface of the liver is preserved and exposed for imaging. Liver specimens from both the left lateral lobes and right anterior lobes were preserved in paraffin and sectioned with a thickness of 50 μm.

For reflective 3D surface area study, intact liver lobes were preserved in Formaldehyde for further imaging use. The Liver surface is the out layer of the liver lobe, which is exposed for imaging.

5.2.2 Histopathological scoring

Tissue samples were stained with Masson Trichrome (MT) stain kit (ChromaView advanced testing, #87019, Richard-Allan Scientific) and whole tissue slices were imaged (Aperio Digital Pathology Environment). Animal tissue scoring based on whole slice MT images was performed by a pathologist based on blind reading to reduce any bias using modified Ruwart score according to Boigk et al. since there was extensive bile duct proliferation noted [124, 142]. A modified Ishak score [46] was considered and served as a guide to align the animal pathological score with clinical human scoring system.

5.2.3 Modification of non-linear microscopy

Similar to Chapter 4, the non-linear optical microscope was developed based on a confocal imaging system (LSM 510, Carl Zeiss) using an external tunable mode-locked Ti:Sapphire laser (Mai-Tai broadband, Spectra-Physics). System is shown in Figure 22. Reflective SHG is built on the other side of the transmission SHG. Reflective SHG signals were collected along the same optical path as TPEF, but with a different band-pass filter of 390-465nm, before entering PMT (Hamamatsu R6357) for detection.

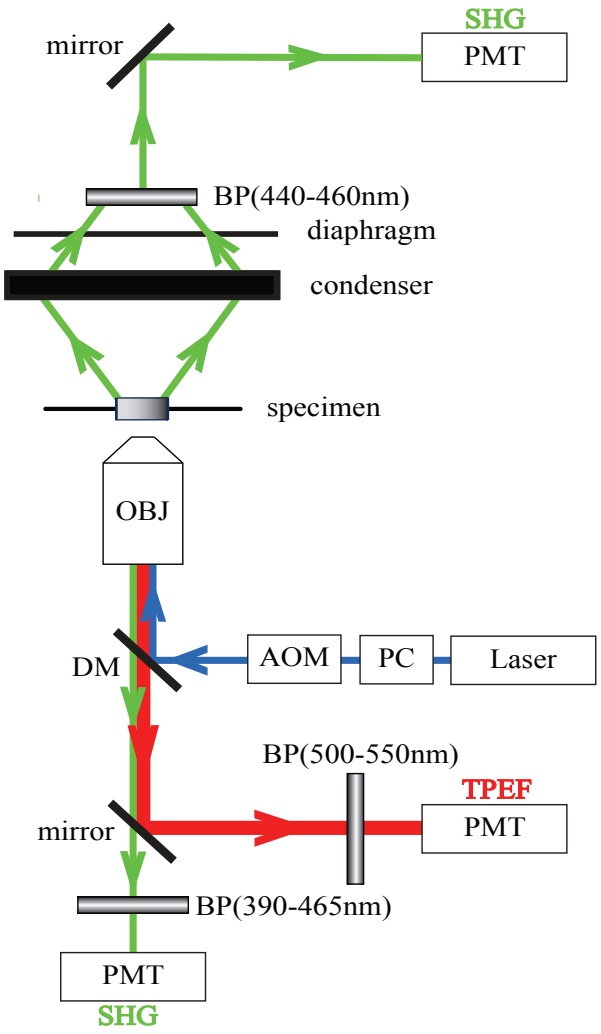

Figure 22. Schematic illustration of the optical configuration. Excitation laser was a tunable mode-locked laser (710 to 990nm set at 900nm) with a pulse compressor (PC) and an acousto-optic modulator (AOM) for power control. The laser went through a dichroic mirror , an objective lens (20X, NA=0.5), and reached tissue specimen. Second harmonic generation (SHG) signal was collected at the opposite side the laser source, in the transmitted mode, by a condenser (NA=0.55), through a field diaphragm, and a 440-460nm bandpass (BP) filter, before being recorded by a photomultiplier tube (PMT). Two-photon excited fluorescence (TPEF) was collected by the objective lens, filtered by a 500-550nm band-pass filter, before being recorded by another PMT. Reflective SHG signal was collected on the same side as TPEF, through the 390-465nm BP filter, and recorded by PMT.

5.2.4 Image acquisition and segmentation

A total of twelve SHG/TPEF images (3072 3072 pixels, ~1.38×1.38 mm) were scanned in transmission mode for each tissue specimen, with four images covering the liver anterior surface area, four images covering the interior re-

gion and four images covering the posterior surface area. Two specimens were extracted from each animal, with one from the left lobe and one from the right lobe of liver. Reflective images were obtained by scanning from the front size of the intact liver lobe. For all images, an image segmentation algorithm based on a mixture Gaussian model was performed to remove background and noise for SHG channel images. It is assumed that the intensity of pixels in the image can be modeled as a mixture of two Gaussian distributions, one representing the collagen area with strong SHG signals and the other representing the background. Using the Expectation-Maximization (EM) algorithm [126], the parameters of the Gaussian distributions which model the peak intensity of pixels in the image were found. A binary image was generated by applying value 1 to all the pixels having intensity that belongs to the Gaussian distribution representing collagen area and value 0 to the rest of the pixels.

5.2.5 Features extraction and quantification

On the liver surface, the tissue edge was detected from TPEF channel image using the Canny method [170], which finds edges by looking for local maxima of the gradient of the image. The percentage of collagen of each line, which is parallel to the edge, is calculated. The width of the capsule, which is the unique feature on surface, is defined as the depth where the percentage of collagen changes most between neighboring lines.

Four common features on both the surface (sub-capsular region) and in the interior of the liver tissues were quantified, namely total collagen area percentage, bile duct proliferation area percentage, collagen in bile duct area per-

centage, and remnant hepatocytes area percentage. Collagen area percentage is defined as the numbers of pixels that belong to collagen in the sub-capsular region divided by the total area of the sub-capsular region. The segmentation of collagen in the SHG channel image is the same as that used for capsule identification. Bile duct proliferation area percentage is defined as the numbers of pixels that belong to bile duct cells in the sub-capsular region divided by the total area of the sub-capsular region. Pixels of the TPEF image were clustered into 3 different groups depending on pixel intensity: completely dark, dim, and bright which represent areas of the vessel or outside-tissue-space, bile duct proliferation area, and hepatocytes respectively. The clustering was performed by a Fuzzy-C means clustering method [127]. A binary image was generated by applying value 1 to all the pixels belonging to the cluster that represents bile duct cell areas and value 0 to the rest of the pixels. The collagen in bile duct area percentage is defined as the number of pixels that are collagen and also in bile duct cells area divided by the total area of the sub-capsular region. The binary image of collagen in the bile duct area is generated by multiplying the binary images of the collagen area and the bile duct cell area. Remnant hepatocytes are defined as those hepatocytes that are surrounded by bile duct cells. Morphological operations such as erosion, dilation and filling holes are performed on the binary image of bile duct cell to identify areas surrounded by bile duct cells. If these areas belong to the cluster that represents hepatocytes, they are recognized as the remnant hepatocytes area. The remnant hepatocytes area percentage is defined as the numbers of pixels that belong to the remnant hepatocytes area divided by total area of sub-capsular region.

All image processing and algorithm computations were carried out in MATLAB (The Math Works, Inc, Natick). Image processing algorithm code is available for readers upon request.

5.3 Results and Discussions

5.3.1 Surface features comparison of SHG/TPEF images and histological images

To explore the surface information in the liver, perfused liver organ was harvested and tissue samples were extracted to expose the liver surface shown in Figure 23(a). Liver samples were then sectioned in the direction perpendicular to the surfaces so as to keep the capsular collagen for imaging purposes as shown in the inset. To validate the use of SHG and TPEF microscopies to quantify morphological changes during fibrosis progression, feature compatibility in both the typical pathological sectors and in SHG/TPEF images was investigated. A pathological tissue section from a fibrotic liver stained with Masson's Trichrome (Figure 23(b)) is compared to a stain-free SHG/TPEF image (Figure 23(c)) from the same location with the pseudo-colors of green representing SHG signals and red representing TPEF signals. When compared with the stained image and with the help from having the major constituents marked out, we can see that both the fibril collagen presented in the internal organ and the capsule collagen in the liver surface can be correctly detected by SHG signals. Due to the presence of intrinsic molecules such as NAD(P)H and flavins that emit substantial fluorescence after excited with femto-pulsed lasers[171], hepatocytes were easily seen as bright red cells in the SHG/TPEF image (Figure 23(c)). Bile duct epithelial cells were shown in Figure 23(c) as the dim red cells due to their lack of fluorescent molecules. The co-localization of these major features proved that the pathological development

of fibrosis on both the surface and in the interior of liver could be well recorded by SHG/TPEF imaging for further quantification.

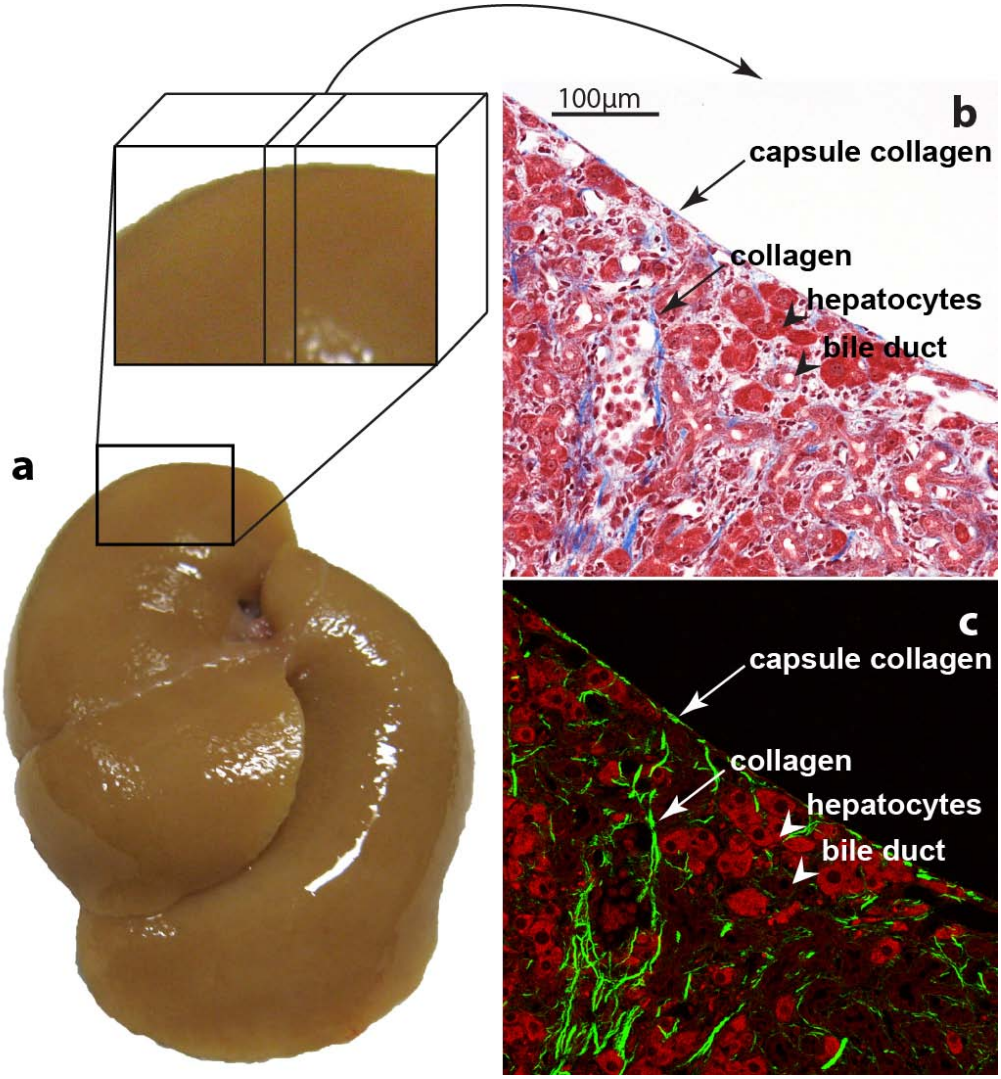

Figure 23. Comparison between histopathological staining and SHG/TPEF images. A perfused fibrotic tissue was extracted (a) and sectioned perpendicular to its surface to expose the liver boundary (inset in (a)). Masson's Trichrome staining for a fibrotic tissue sample by the directed cutting was shown in (b), with collagen stained in blue and cytoplasm in red and cell nuclei in dark brown. The SHG/TPEF image of the same sample was shown in (c) with collagen in pseudo green and cells in pseudo red. Features of capsule collagen, collagen, hepatocytes and bile duct shown in staining image (b) can all be identified in the SHG/TPEF image (c) respectively. Scale bar is 100μm.

5.3.2 Comparison of liver surface among different stages

Using the non-linear microscope, tile scan images of different liver surfaces were taken. As shown in Figure 24, (a) and (b-e) represent normal and stage 1 to stage 4 fibrotic livers. Similar to what we observed in stained histopathological samples, with the progression of liver fibrosis, accumulation of collagen fibrils was evident by stronger and more profound SHG signals detected both in liver interior and near surface region. In both regions, accumulation of bile duct area was also observable marked by the increase of dark red area. The progression of collagen distribution and bile duct proliferation to the surface with the increase of liver fibrosis can be easily observed in the images. Also, the thickening of liver capsule was observable in the fibrotic liver compared with normal liver tissues (Figure 24(a)). With these observations as the basic prove, next step we would quantitatively explore the relationship between liver surface region and the interior and focus on the liver surface region for fibrosis assessment.

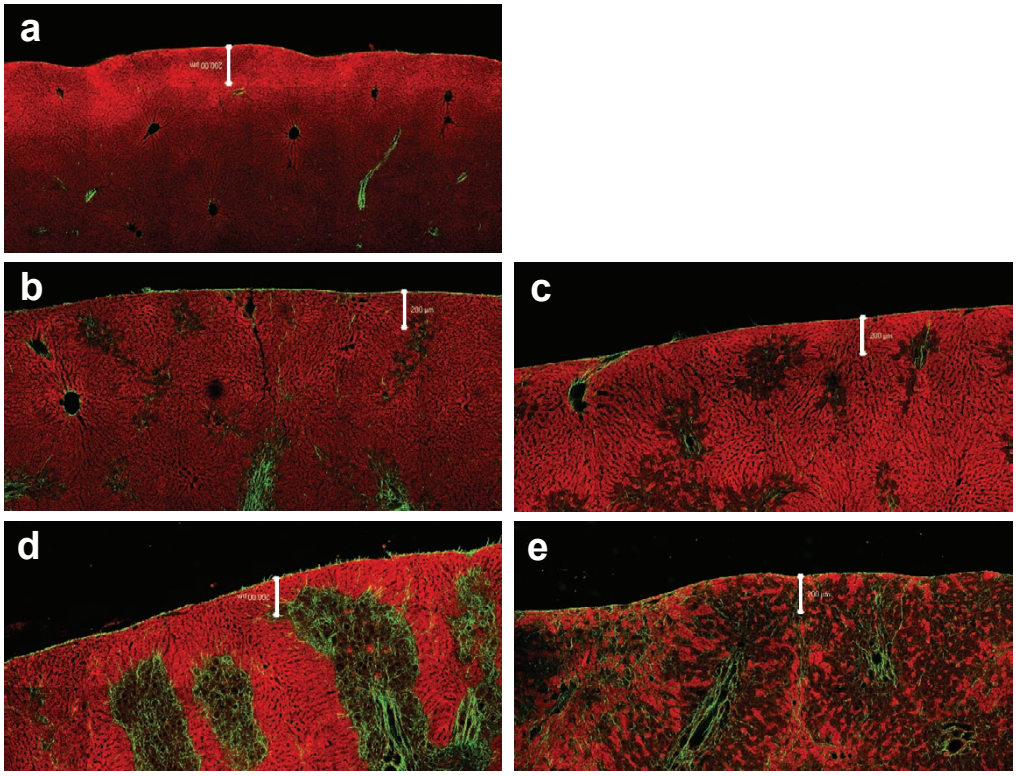

Figure 24. Liver surfaces at different stages of liver fibrosis. Normal (a) and stage1 to stage 4 (b-e) fibrotic livers were imaged using non-linear microscope. With the progression of the disease, collagen (SHG) and bile duct area (TPEF) was accumulated both in liver interior and near liver surface. Surface capsule was thicker in fibrotic liver (b-e) compared to normal liver (a). Scale bar is 200μm.

5.3.3 Liver surface regions definition

In order to perform a quantitative analysis of liver surface features, we need to define liver surface and separate the surface area into regions that show different properties. First, we rotated all images that we obtained into a top empty position, whereby there is no tissue sample from the top edge of the image and the liver surface is exposed on the top. Then combined SHG/TPEF images (Figure 25(a)) were separated into TPEF (Figure 25(b)) and SHG (Figure 25(c)) channels to differentiate the autofluorescence of liver cells from the second harmonic signals of type I collagen. In the TPEF images, the liver boundary was defined as the line boundary between the empty region and the

region where there is autofluorescence, and the liver surface is the area below the boundary. Due to the morphological difference between capsule and other liver cells, we separate the surface area into two regions: the capsule region and the sub-capsule region. The definition of the two was defined in second harmonic images (Figure 25(c)). The SHG image was first converted into a binary image with regions that do not have signals shown as 0 and those with signals as 1. As the line boundary obtained from the red channel were moved pixel by pixel downwards, we observed an increase in the average amount of collagen (line average in Figure 25(d)) through a maxima and back to its initial value. This gave the thickness of the capsule region. The thick white line in Figure 25(c) is the capsule region in that image. Tracing parallel to this line, we went deeper into the tissue until we reached a depth where meaningful features or trends could be observed. This gave a thickness to the sub-capsule region. In this study, we restricted this thickness to 150μm, since for application purposes, SHG/TPEF images have a limit on penetration depth into the tissue.

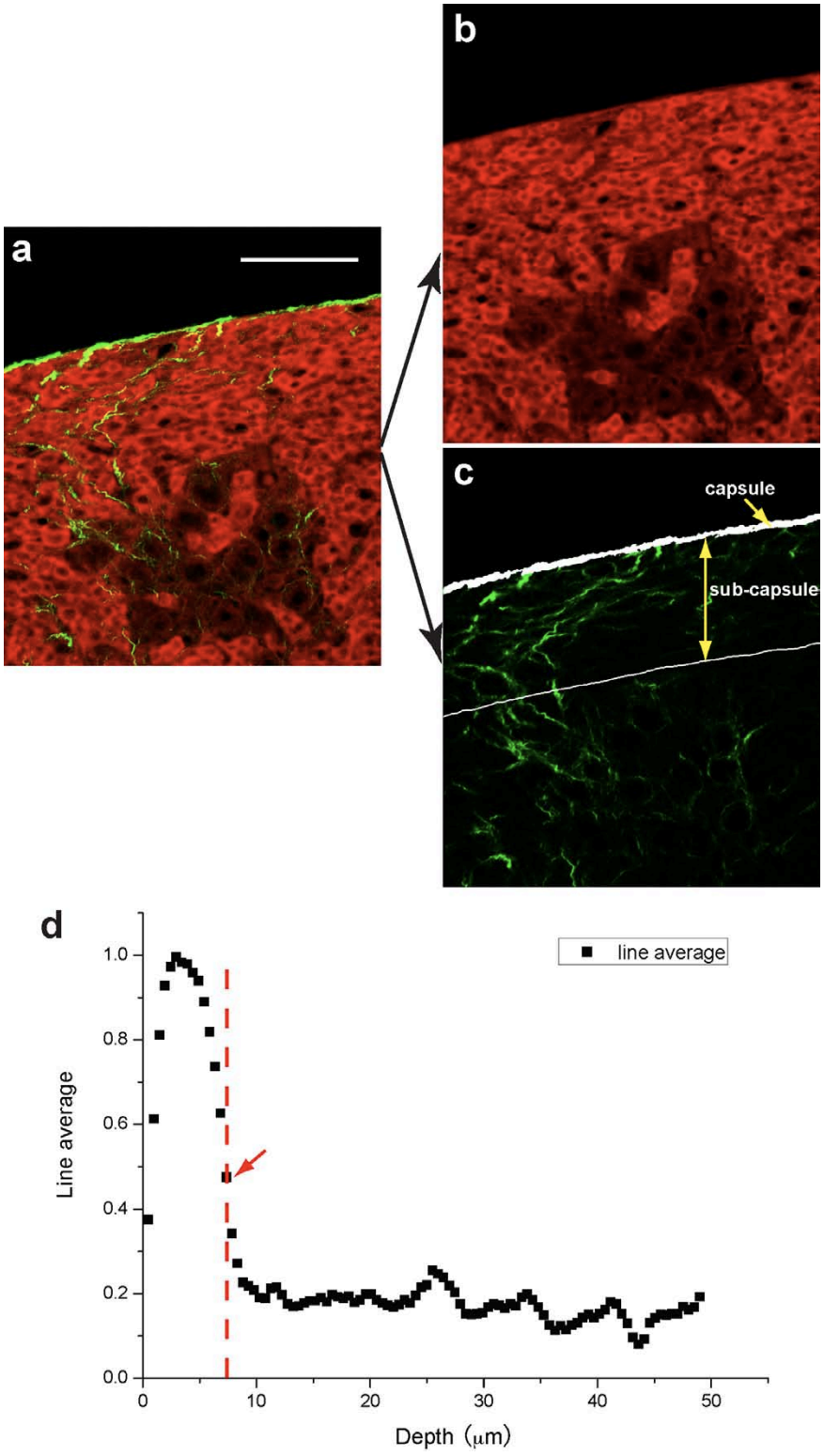

Figure 25. Definitions of capsule and sub-capsule regions in the liver surface. The combined SHG/TPEF image (a) was separated into TPEF (b) and SHG (c) channels. After finding the liver boundary in TPEF image (b), collagen content in the SHG image (c) was calculated with increase of depth into the tissue (d) marked as line average. The depth at which there was a sharp decrease of collagen content (red arrow in (d)) was marked as capsule width (c), sub-capsule region was defined as the region parallel into the tissue. Scale bar is 100μm.

5.3.4 Four features extraction from both surface and interior tissue

With capsule and sub-capsule regions defined, we proceed to extract features from the two regions on the surface together with the liver interior. The defined thickness of the capsule region is a unique feature in the surface area. In the sub-capsule region of the surface area and in the interior, the parameters included in the study were total collagen, collagen in bile duct areas, bile duct proliferation and areas occupied by remnant hepatocytes. The feature extraction methods have been elaborated in methods, and features extracted have been exemplified as binary maps in Figure 26 based on the same sample image in Figure 25. Total collagen (Figure 26(a)) is defined as the percentage of collagen that was presented in SHG images in the sub-capsule and interior area. Bile duct proliferation (Figure 26(b)) was defined as the percentage of areas in either the sub-capsule or the interior that was occupied by bile duct cells. By overlapping Figure 26(a) and Figure 26(b), we obtained Figure 26(c), which is the percentage of abnormal collagen that was distributed in the bile duct area. The area occupied by remnant hepatocytes (Figure 26(d)) is the percentage of areas taken by remnant hepatocytes, defined as small surviving hepatocytes clusters that are surrounded by bile duct cells, in the sub-capsule or interior of liver.

All four features extracted here were based on comparison with original stained tissue samples and are related to pathological readings.

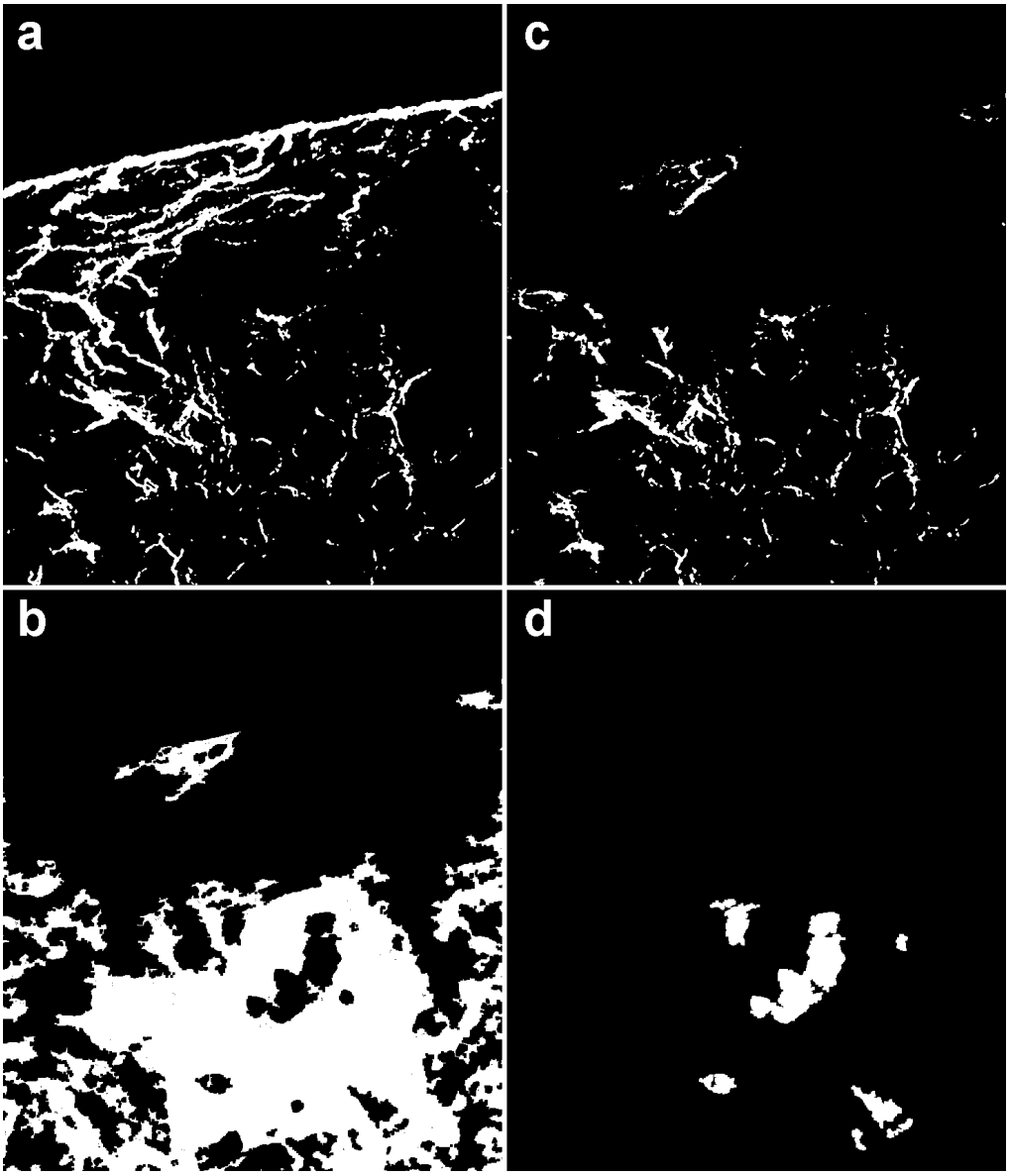

Figure 26. Feature extraction from SHG/TPEF images. Based on the same SHG/TPEF image from Figure 25, the SHG image was segmented into a binary image (a) representing total collagen in both capsule and sub-capsule regions, and liver interior. Bile duct area in the TPEF image was segmented into a bile duct mask (b). Combining the collagen mask and bile duct mask, the feature of collagen in the bile duct area was shown in (c). Hepatocytes clusters that were surrounded by bile ducts were segmented as potential remnant hepatocytes (d).

5.3.5 Correlation between liver surface and interior

To use the features extracted earlier to investigate the relationship between the liver surface and interior during fibrosis progression, we first tested the ap-

plicability of our features in assessing fibrosis in the liver interior where most current studies were focused [118, 169]. Results (Figure 27(a)) showed that, with the natural progression of liver fibrosis indicated by the increasing time points (weeks 0, 2, 4, and 6) after BDL, total collagen, collagen in bile duct areas and bile duct proliferation increased with significance across different time points ($p<0.05$ among all time points in all three features). The dramatic increase of bile duct areas in this case is due to the specific model (bile duct ligation) we chose in this study. However, this feature is still applicable in other models. Comparing the difference of total collagen and collagen in bile duct areas, we can see that there is an almost consistent level of difference between the two, indicating a base level amount of normal collagen in the tissue, which is consistent with pathological findings. This also makes collagen in bile a more sensitive indicator to detect fibrosis in liver. Areas occupied by remnant hepatocytes also increased with fibrosis progression. However, between week 4 and week 6, no significant difference presented for the increase, making this feature only a sensible indicator for early stages of fibrosis.

To verify that the four features we extracted are reasonable parameters to quantify liver fibrosis, the correlation of liver surface and interior was studied based on the features. Since these features were only present in the sub-capsule region, the correlation coefficient between the sub-capsule region and the interior was calculated. Each plot in Figure 27(b) is the result of comparing the same parameter value between that obtained in the surface images to the interior images at a particular depth of sub-capsule region. Three of the parameters studied showed an upward trend in correlation reaching a plateau stage at about 20μm. The parameter of remnant hepatocytes has a lower corre-

lation, making it not a consistent feature for the two areas. Therefore, we define our depth of meaningful correlation between the surface and interior regions as 20μm, beyond which no additional information can be obtained from the system. This would mean that, to monitor fibrosis from the surface of the liver, we would only require the sampling of 20μm beneath the capsular collagen network.

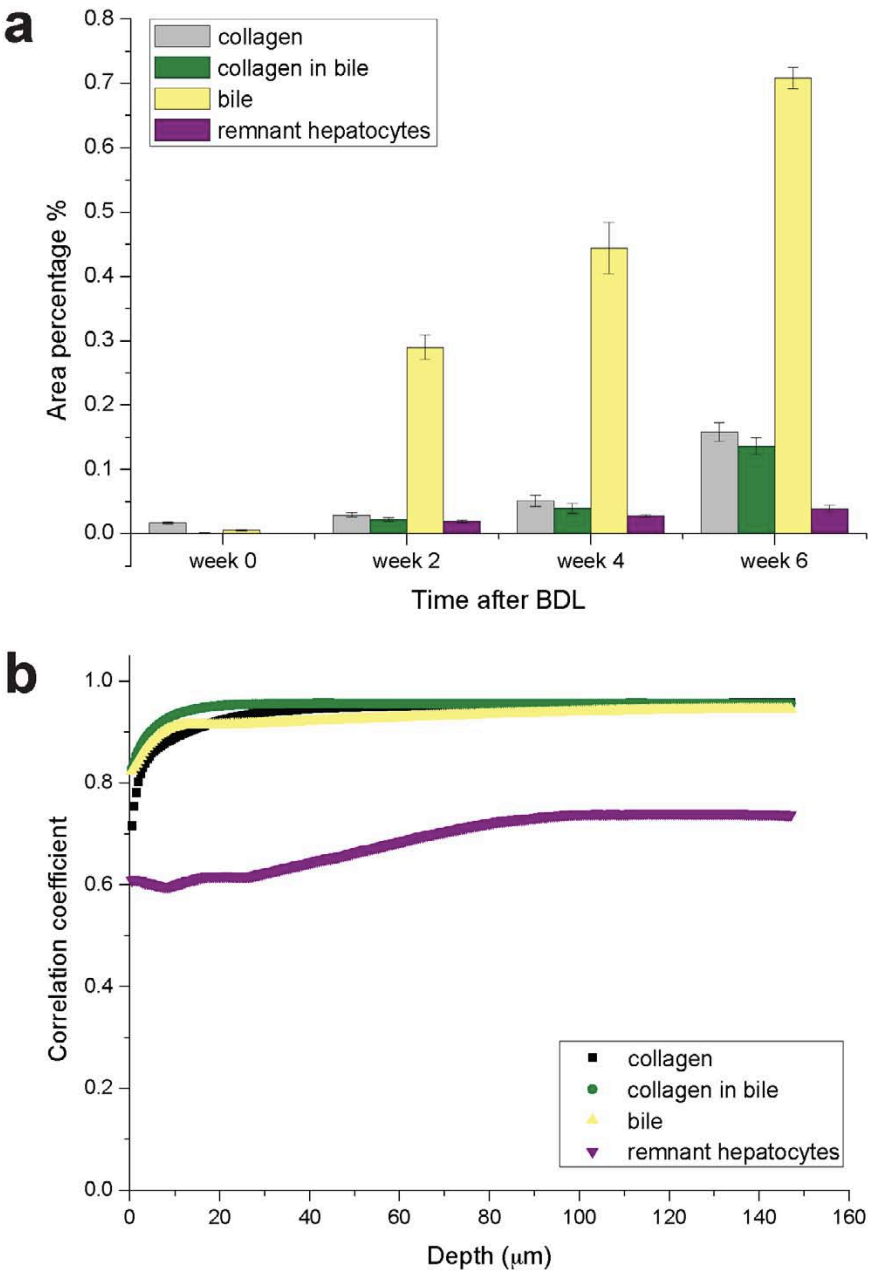

Figure 27. Comparison of liver surface to interior. In the liver interior, the percentage of areas occupied by four different features was shown at different time points after performing bile duct ligation (a). All extracted features show a significant ($p<0.05$) upward trend with the progression of fibrosis among different time points except for remnant hepatocytes between week 4 and week 6. The correlation coefficient of features between the liver interior and the surface is shown in (b). Features of total collagen, collagen in bile duct and bile duct proliferation show an upward trend correlation between surface and interior with the plateau of 20μm depth in the sub-capsule region. Remnant hepatocytes have a lower correlation.

5.3.6 Fibrosis distribution across the anterior liver surface

Studies so far have been performed on the anterior surface of both the left and right lobes of liver tissues. To understand the relationship between different lobes in order to direct future sampling locations, we again calculated the correlation coefficient of two lobes based on the four features at different depths of the sub-capsule region. The results (Figure 28(a)) showed that high feature correlation between the two lobes existed when the sub-capsule region reaches 20μm and above based on three meaningful quantitative features of total collagen, collagen in bile duct areas and bile duct proliferation. Thus, we can confidently monitor the progress of fibrosis with either lobe by scanning across their surfaces with no misrepresentation of the extent of fibrosis.

It is intuitive that the scanning of liver surfaces would be done on the anterior of each lobe. Therefore all the quantitative analysis done so far was based on the anterior surface. However, in order to understand the fibrosis progression from a global perspective, we also investigated the correlation between anterior and posterior liver fibrosis. Figure 28(b) showed that lower correlation existed between the anterior and posterior liver surfaces based on pathological features, also the correlation between posterior and interior is much weaker (data not shown). This indicated that liver fibrosis progresses in a heterogeneous manner toward anterior and posterior surfaces, with anterior surfaces possessing characteristics similar to the interior. Since anterior surface is the main focus for surface scanning purposes, it is less important that there are no highly correlated anterior and posterior surface scans.

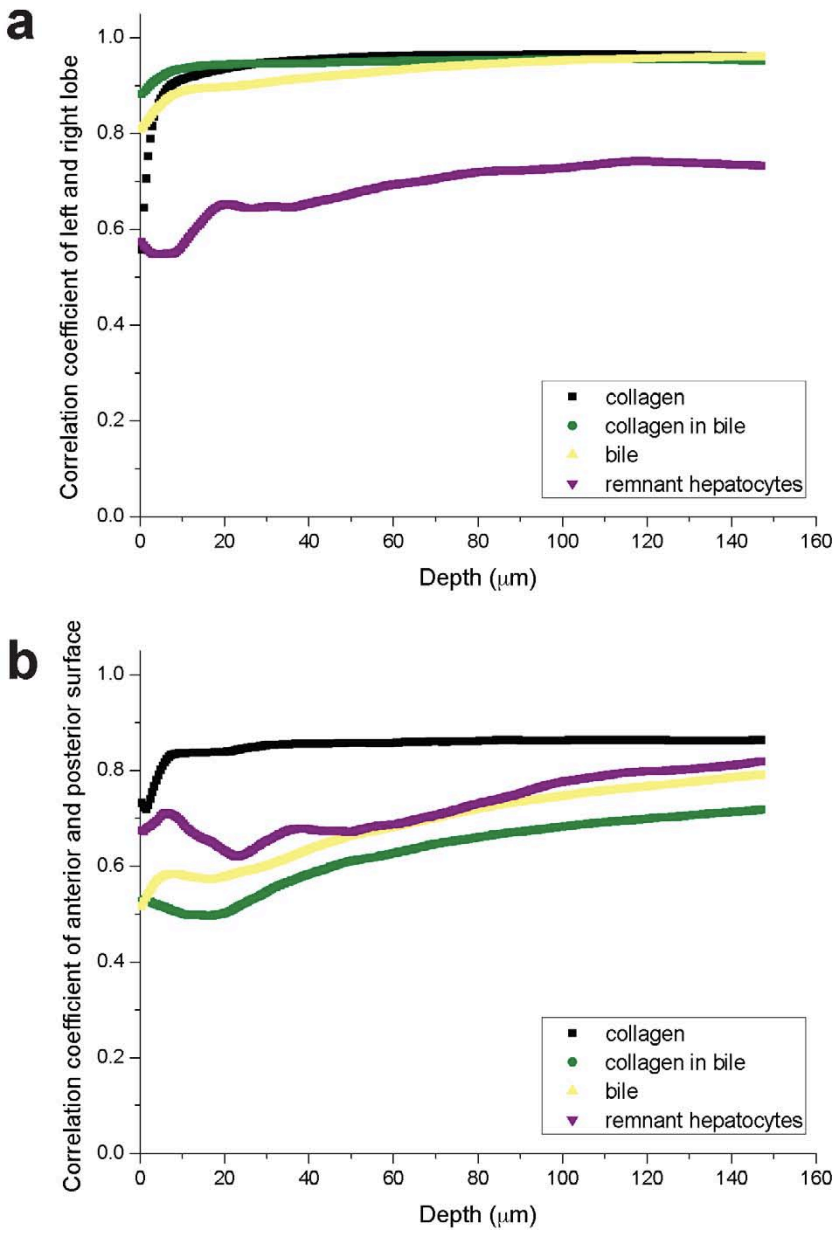

Figure 28. Quantification of the fibrosis distribution on the liver surface. (a) The correlation coefficients of the liver left and right lobe surface features are shown. Except for the feature of remnant hepatocytes which are less correlated, all other surface features have high correlations, and remain constant reaching the sub-capsule depth of 20μm. (b) The correlation coefficient of the anterior and posterior surface features remains at a low level, indicating less correlation between these two surfaces.

5.3.7 Features on liver surface as indication of liver fibrosis

Now that the liver surface is highly correlated with the interior regarding the morphological features stated above, and the fibrosis distribution is uniform

across the liver anterior surface, we focused on the anterior liver surface to quantitatively assess liver fibrosis. A sub-capsule region of 20μm was shown as an example here, since it represents the minimal sampling amount for the meaningful correlation of surface and interior. With 50μm thickness of the tissue slices and the scanning length of 1380μm on the anterior surface, an area of 69000μm^2 on the liver surface was covered by each SHG/TPEF image, which is smaller than the equivalent surface area of 225625μm^2 a non-linear endomicroscopy can scan [172]. The same four features (Figure 29(a)) were extracted in the sub-capsule region, with each quantified at different time points (week 0, 2, 4 and 6 after BDL). Conventional assessment based on the histopathological scoring system [124] was also performed in all tissue samples as a control comparison. Fibrosis was scored in five stages, 0, 1, 2, 3, 4, with stage 0 denoting no fibrosis and stage 4 denoting the most advanced fibrosis or cirrhosis. We found that, in the sub-capsule region (Figure 29(a)), features of total collagen, collagen in bile duct areas and bile duct proliferation have close agreement to that of the histopathological scores. The differences between different time points are also significant ($P<0.05$) except for total collagen in early stages (between week 0 and week 2) due to its higher basal level of normal collagen in the sub-capsule region. Areas occupied by remnant hepatocytes, as a less correlated feature between surface and interior, did not show an observable trend with the progression of fibrosis in the surface; however, as in the interior, remnant hepatocytes on the liver surface are a good indicator for the occurrence of fibrosis.

As suggested by Buschmann, R.J etc [14], capsule collagen width can be used as a measurement of fibrosis, also, as capsule thickening in liver disease is known to occur. Here, we quantified the capsule collagen width based on our capsule definition (Figure 29(b)) as a unique feature in the surface area. The trend of increasing thickness with fibrogenesis in our model confirmed the non-quantitative findings in the previous study [14, 173]. However, even though we can differentiate the early and late stages of BDL, we cannot make clear distinction between each consecutive stage based on this feature. Due to the inappreciable increase in width between each two-week interval, this can hardly be used as a sensitive means to monitor fibrosis in a two-dimensional situation. Potentially with the 3D structure of collagen distribution, we might be able to implement more aspects of capsule feature for detailed quantification. Therefore, quantification of liver fibrosis on the liver surface only works when SHG and TPEF microscopies enable the quantitative imaging of liver surfaces beneath the capsule.

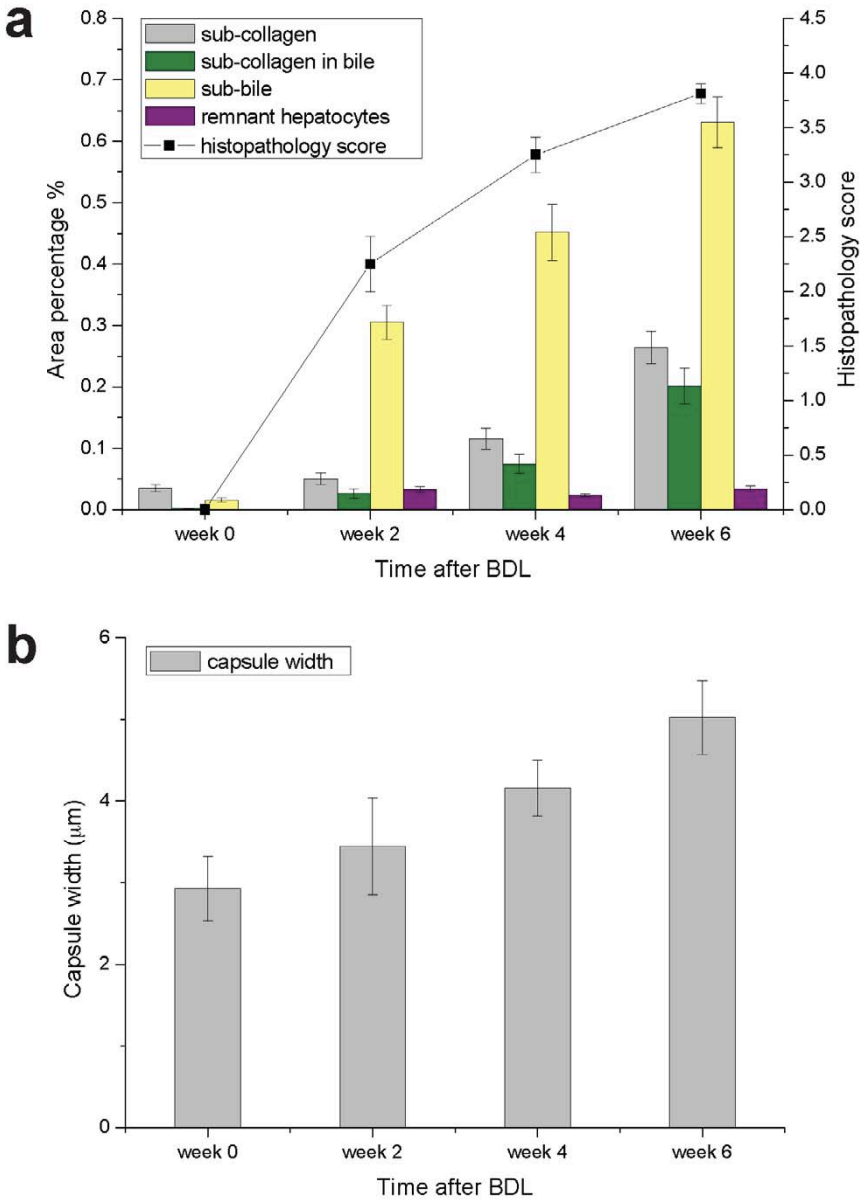

Figure 29. Quantification of liver fibrosis progression on the liver surface. (a) Quantification results of different features extracted from SHG/TPEF images obtained at different time points after BDL showed that there is an upward trend with the progression of fibrosis regarding all features. Significant differences among different time points exist for collagen in the bile duct area and bile duct proliferation in the sub-capsule region. This upward trend also agrees with the histopathology scoring results of the same stained tissue samples. (b) Capsule width in the capsule region also increases with the progression of fibrosis, with more significant increases in the late stage of fibrosis.

5.3.8 Potential application in surface scanning

With the anterior liver surface pertaining the consistent features as in the liver interior, we compared the normal and fibrotic anterior liver surface by scanning on the front size of the perfused liver using reflective mode SHG and TPEF, shown in Figure 30. In the capsule region in normal liver (Figure 30(a)), capsule collagen was condense, and regularly aligned compared with that in fibrotic liver (Figure 30(c)). This lose alignment of capsular collagen in fibrotic tissue could explain our observation of increased capsular width in the tissue slices. In the sub-capsule region, 20μm below the capsule region, normal liver (Figure 30(b)) has well-organized hepatocytes and no clear collagen presence. While in the BDL fibrotic liver (Figure 30(d)), bile duct proliferation is obvious, which destruct the alignment of functional hepatocytes. Abnormal collagen is also present around the bile duct cells, a clear indication of fibrosis. All these features are consistent with the observation in the liver tissue slices, although in the reflective mode images, SHG signals are much weaker, evident by the less amount of collagen presence in the fibrotic liver. With these feature pattern differences between normal and fibrotic liver surface, we are potentially able to quantitatively monitor liver fibrosis progression on the liver surface.

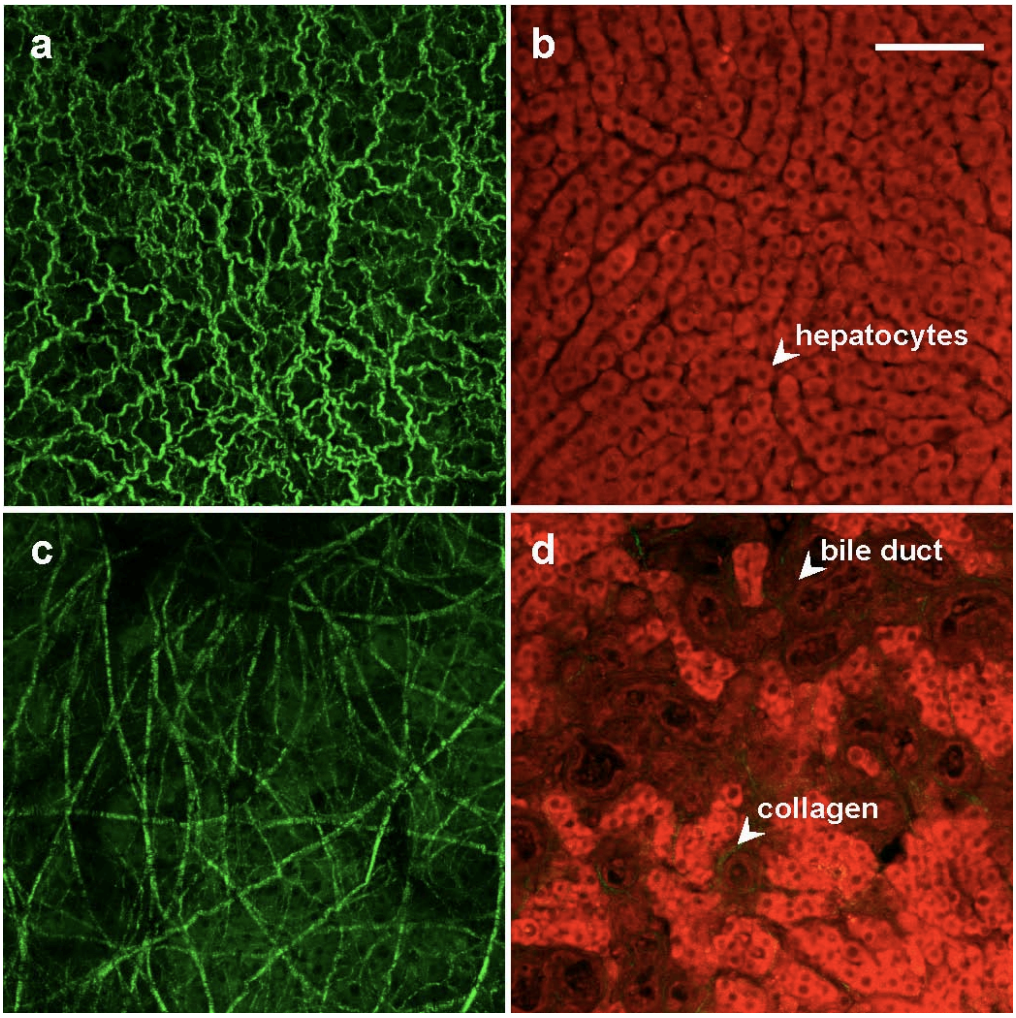

Figure 30. Liver anterior surface scanning. Front size images from liver surfaces were obtained by reflective SHG and TPEF imaging. 3-D projections of capsule regions were shown in both normal (a) and fibrotic liver (c). Irregular and loss alignment of capsule collagen distribution in fibrotic liver is observed compared to normal liver. Sub-capsule region images were obtained 20μm below the capsule region in respective normal (b) and fibrotic (d) liver tissues. Features of bile duct and abnormal collagen proliferations were present in fibrotic liver (d) compared to normal liver (b) where only well-organized hepatocytes present. Scale bar is 100μm.

5.4 Conclusion

We discovered a strong correlation between liver fibrosis progression on the anterior surface and the interior based on quantitative analysis of morphological features in both regions. Using SHG and TPEF microscopes, we demonstrated the feasibility of monitoring liver fibrosis progression on the anterior surface with the BDL animal model by comparing with the conventional histopathological scoring system. We also discovered a uniform distribution of quantitative liver fibrotic features, such as total collagen distribution, bile duct proliferation and collagen in bile duct areas, across two main lobes of the anterior liver surface, which gave us confidence to quantitatively monitor the progress of liver fibrosis on different lobe surfaces. With all this information laid out, we are now one step closer to applying reflective or endoscopic imaging of the liver to diagnose and stage liver fibrosis, which can potentially be used clinically to complement or eventually, avoid the more invasive liver biopsy.

Chapter 6 Liver fibrosis surface assessment and window model establishment

6.1 Introduction

For liver fibrosis diagnosis and assessment, currently, biopsy still represents the gold standard with its known complications and drawbacks [4, 52, 102, 103]. Other non-invasive imaging methods, such as ultrasonography [162], transient elastography [163] and magnetic resonance elastography (MRE) [60, 164] have shown potential for fibrosis assessment and staging. However, they are only based on liver stiffness measurements (LSM), which is not directly comparable with morphological features that biopsy samples obtain. Their sensitivities are also less satisfactory with current studies.

To develop a less invasive imaging methods for fibrosis assessment and to extract comparable morphological features, SHG/TPEF imaging modalities were studies on their application for information extraction and quantification of fibrotic features. Due to their limited penetration property, surface information of liver organ was targeted. To incorporate the findings we have discovered in earlier studies that liver surface has a strong correlation with liver organ fibrosis distribution and that by examining liver surface alone, we can quantify the liver fibrosis degree, we now propose to apply such findings into the live animal imaging to explore the full potential of *in vivo* monitoring fibrosis progression in laparoscopy application.

The first transparent window chamber was developed by Sandison in 1924, implanted in the ear of a rabbit, which allowed continuous, non-invasive,

long-term monitoring of angiogenesis during wound healing [174]. Currently, with the development of multiphoton laser scanning microscopy, application of such three-dimensional high resolution imaging method in the biomedical study triggered more chamber window designs. The design of intravital hepatic imaging chamber especially allowed the investigation of in-vivo dynamics of hepatic activities in rodents without additional treatments [175]. Technically, the chamber can be applied to the animal as long as the animal is alive, and for current design, the animal can be imaged with the chamber for as long as 6 hours.

For live imaging of rat liver surface in our study, an intravital window based imaging chamber was designed to apply on rat abdomen for fibrosis monitoring. Cross modality comparison between SHG/TPEF imaging methods and MRI imaging methods for fibrosis assessment was proposed on the window rat model. Therefore, different chamber materials were searched and tested for compatibility purpose. Different animal fibrosis models were also explored in the study to refine the live imaging quality and to explore the model differences.

6.2 Materials and Methods

6.2.1 Window intravital chamber design

The idea of the liver chamber is to open a window in the abdomen of the rat to obtain *in vivo* images of the liver surface by means of optical microscopy methods. To achieve this, window intravital chamber prototypes were drawn using Solidworks (Dassault Systèmes SolidWorks Corp.), and then sent for fabrication in plastic. After examining the prototypes, improvements were made to the corresponding design, and the final product would be fabricated in titanium due to its good biocompatibility and light weight.

Based on the previous chamber design used on mice by National Taiwan University [175], and with continuous help from Professor Dong's group who designed the chamber, we came up with a few prototypes for the chamber component used for rats. The dimension of the rat liver (Figure 31) limits the maximum radius of the chamber. Due to the asymmetric structure of the rat liver, we proposed to attach window chamber over the left lobe of the liver for the imaging exposure. For flat attachment of the liver to the window chamber, a window diameter of less than 25mm was proposed.

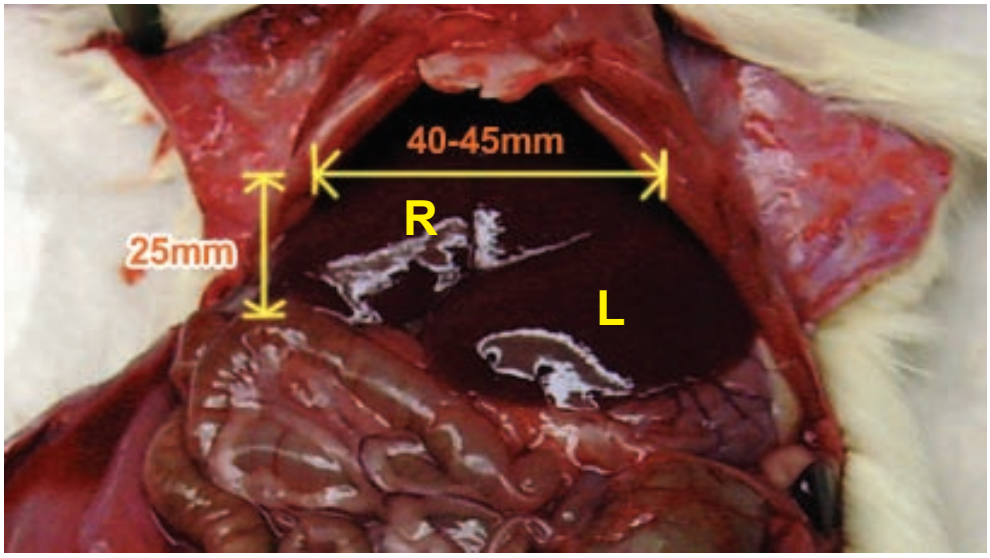

Figure 31. The front view of the abdomen of the rat, demonstrating the area available for the chamber attachment. L, R represents left lobe and right lobe of liver respectively.

6.2.2 Material search for window chamber

In order to apply intravital SHG microscopy and MRI on the same subject in the same period of time, the imaging chamber should be made of MRI artifact-free materials. As apposed to the design employed on mice study [175], we were trying to find a non-glass MRI artifact-free polymer that possess property of biocompatibility, good mechanical strength and good optical properties. Polyethylene terephthalate (PET), with its high transparency and similar magnetic susceptibility with soft tissue, was identified as the potential candidate for replacing glass.

Signal Scattering from Fluorescent Microbeads:

2.5µm diameter microbeads (Inspeck^{TM} Orange (540/560) microscope Image Intensity Calibration kit) with 30% fluorescent intensity were used to study the

degree of signal scattering. 40X images of microbeads kept under glass cover-slip and PET cover-slip were captured using Zeiss LSM 510 Meta.

Resolution study with SHG signal from muscle tissue:

30 μm thickness Rat pectoral muscle tissue was prepared. The images were taken by Zeiss LSM 510 Meta, with Plan-Neofluar 20x lens, The SHG channel with 900nm excitation and 450nm emission was applied, together with autofluorescence channel.

6.2.2.3 Resolution study using cervical cancer cells

HeLa cells labeled with pDsRed in ER was cultured on glass and PET cover slip, and observed under autofluroscence with excitation 543nm and emission bandpass filter 565-615nm. The image was taken using Zeiss LSM 510 Meta with Plan-Neofluar 40x lens.

Spectrogram comparison:

The intensity of light transmitted through different cover slip was recorded. The result was compared to the value with no cover slip in. The transmission spectrum was obtained by dividing the signal with cover slip to that of no cover slip.

6.2.3 Application of window intravital chamber on rats

Pre-surgical preparation:

Surgical instruments were autoclaved at 121°C for 22 mins. Autoclaved items were dated, labelled and used within a week. Surgical space was disinfected with 70% ethanol.

Preparation of animal for surgery:

The male Wistar rats were transported to the preparation room and sedated using ketamine and xylazine (75mg/kg ket/ 10mg/kg xyl I.P). Animals were then shaved on the abdomen and fur was removed with a vacuum evacuator. Operation site was swabbed with 1% cetrmide followed by 0.05% chlorhexidine. The rat were injected with 5ml 0.9% NaCl S.C perioperatively. The abdomen was then draped and finally swabbed with povidone iodine.

Intravital chamber installation:

The incision of the upper abdomen was sutured, leaving a part open to create a circled wound to position the liver window device inside the abdominal wall. Prior to installing the lid, a cover glass / transparent membrane was adhered around the outer rim by a biocompatible tissue adhesive Histoacryl (B. Braun Melsungen AG, Germany). The cover glass / transparent membrane serves as the observation window of intra-vital activities. The lid was then sutured through the small holes on the ring to the skin and peritoneum. To ensure tight contact of the liver surface with the cover glass / transparent membrane and to minimize motional artifacts associated with heartbeat and respiration, tissue adhesive was applied to the edge of the lid to adhere the liver to the imaging chamber. Fluid therapy was given perioperatively with 5 - 7 ml of potassium/sodium chloride premix injection.

6.2.4 Image acquisition from window chamber animal model

Non-linear imaging system set-up is the same as presented in Chapter 5, 5.2.3.

The rat installed with the window intravital chamber was kept in the supine position with the intravital chamber fitted into the U-shaped groove of a steel plane, which is screwed tight to another round steel plane that fits into the microscope stage. The round stage was also screwed to the microscope stage for stability. In this manner, the rat can be firmly attached for live imaging purposes.

Non-linear microscopy set-up was exactly the same as that has been used in Chapter 5 (Figure 22). Reflective mode SHG and TPEF imaging was applied during live imaging of rats.

6.2.5 Rat toxicity model establishment

Male Wistar rats at an average weight of 220g were housed two per cage in Biological Resource Centre (BRC) of Biopolis A*STAR with free access to laboratory chow and water in a 12:12h light/dark schedule. The rats were administrated with intra-peritoneal (ip.) injection of Thioacetomide (TAA) 200mg/kg of body weight with PBS, three times a week.

6.3 Results and Discussions

6.3.1 Window intravital chamber for rat liver live imaging

To achieve the goal of live imaging for rat liver, the window intravital chamber diameter was fixed to the liver exposure size of less than 25mm diameter. The reason for choosing a round shape for the chamber is that the rounded shape is easier to stitch on rats' liver without worrying about the dimension of the shape, and less abrasion will be caused by the edge of the chamber.

After fixing the shape, the first two prototypes (Figure 32) we tested were the ones that were designed by National Taiwan University for mice, with two components design (Figure 32(b)) published in a recent paper [175]. We changed the size of those two designs to fit rats. The one component chamber (Figure 32(a)) was designed to be sutured to the skin through the eight holes along the chamber edge. Round indentation on the surface was designed to connect to glass / polymer cover slip with glue. The liver would be in touch with the cover slip surface through gravity. Since both mouse and rats have two layers of skin, we found it would be more stable if we have two components for the chamber, so that both layers can be sutured to the chamber components. For this reason, we tested two-components chamber design (Figure 32(b)). The inner lid was designed to be sutured and glued to the muscle layer in front of the peritoneum. A round cover slip would be glued onto the indentation of the inner lid on the bottom. The outer lid would be screwed into the inner lid to clamp the tissue layers from liver to skin. It would then be sutured to the skin.

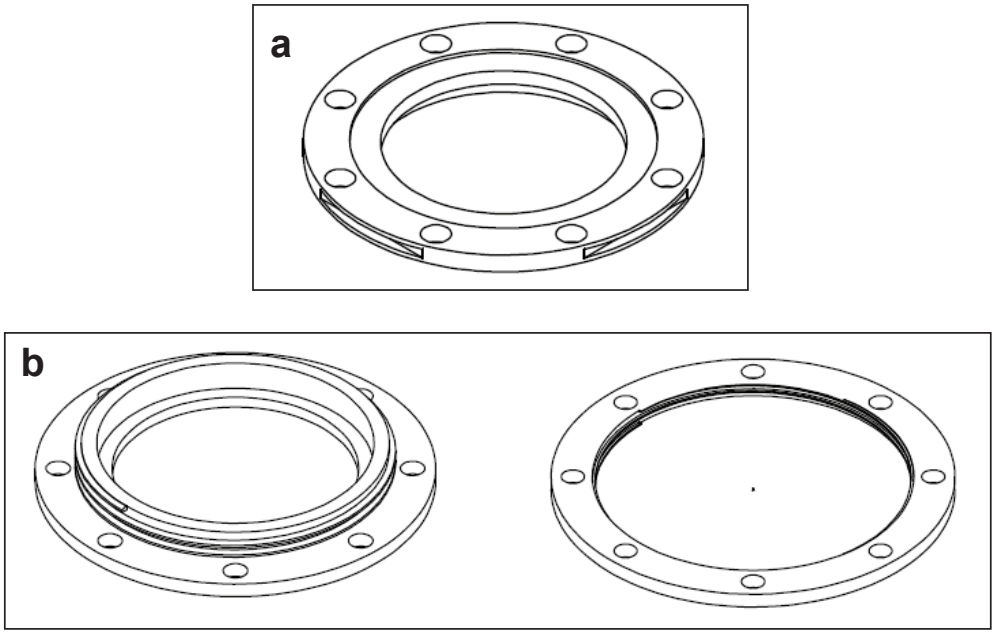

Figure 32. Two original prototypes of window intravital chamber designs. Prototype (a) has one component, was designed to be sutured to the rat skin and glued to the liver surface with cover slip glued on the top. Prototype (b) has two components, with inner lid (left) sutured to the muscle layer with cover slip glued to the bottom of the chamber, and outer lid (right) screwed the inner lid and sutured to the tissue layer of the skin.

The two-components design has the advantage of stability. To improve on the quality of the images and to prevent the scratches on the cover slip from the rats, we further designed three novel prototypes of the intravital chamber. As shown in Figure 33(a), a screwing cover (right) was introduced in the original two-components design, with the whole compartment made of light material. For the potential application on MRI imaging, the cover slip was proposed to be removed during imaging to reduce the artifacts caused by glass material. Therefore, another designed was introduced (Figure 33(b)) to include a removable part (right) that attached to the glass cover slip. This also solves the problem of scratching by the rats. Glass window can be easily plugged in for optical microscopy and taken out and replaced by other materials for the remaining time. In order to reduce the size of the chamber into two components,

we further removed the screwing part of the removable window. Instead, a small protrusion on both sides of the chamber was introduced for window plug-in. Making use of the elastic property of the material, when the window plug-in was pushed into the frame, the protrusion would then slip into the small hole in the frame. To remove the window plug-in, forceps would be used to hole the ends with the protrusion and to pull it out. To still maintain the stability of the intravital chamber, double layer stitching was introduced during surgery. Therefore, only one stitching chamber would be needed for the design.

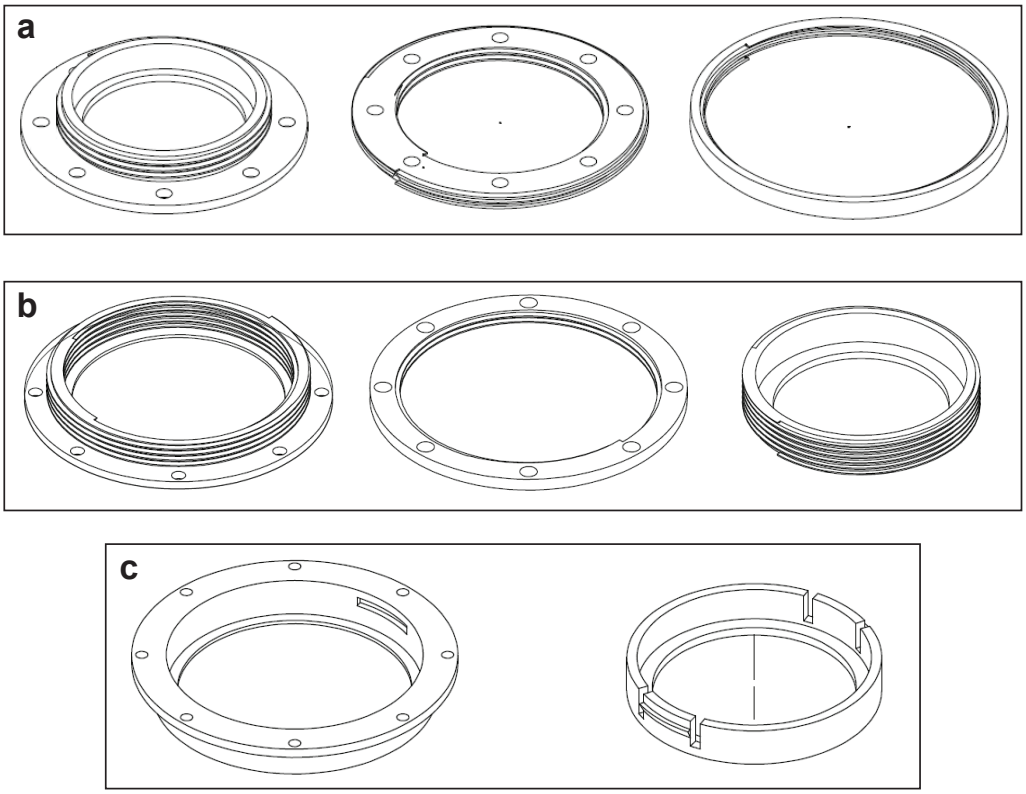

Figure 33. Three novel prototypes of window intravital chamber designs. Prototype (a) has three components, with inner lid (left) and outer lid (middle) securing the chamber on the rat abdomen and screwing cover (right) applied to the outer lid to protect the cover slip. Prototype (b) has three components, with inner lid (left) and outer lid (middle) same as prototype (a) and window screw-in (right) glued to the cover slip at the indentation on the bottom. The window with cover slip can be screwed in and out to inner lid upon different usage. Prototype (c) has two components, with chamber frame (left) sutured to the skin and window plug-in (right) glued

to the cover slip on the bottom. It can also be plugged in and out from the window frame upon different usage.

All the prototypes designed so far can meet the requirement of stability and easy handling. However, since the position of the cover slip on the two- and three-components designs was at the bottom of the intravital chamber, the movement of the objective lenses on the viewing window was restricted by the radius of the chambers. After researching the objective dimensions of the lenses in the lab (Table 4) and considering the optimal viewing size of the rat liver (less than 25mm), we discovered that, based on the current design, the objective lenses cannot cover a large enough surface area for fibrosis assessment. Considering this, we proposed modifying the original one component design to allow flat viewing surface, so that the object lenses can move freely on the window chamber, allowing larger coverage of the liver surface for imaging.

Table 4. Dimensions of various objectives available in the laboratory.

Objective class	Diameter (mm)	Working distance (mm)
Olympus UPLASPO 20X	24.0	0.60
Olympus LCACHN 20XPHP	24.0	3.20
Zeiss Plan-Apochromat 10X / 0.45	22.5	0.193
Zeiss Plan-Apochromat 63X / 1.40 Oil DIC	22.5	2.06

To increase the viewing size of the liver surface and take advantage of standard glass cover slip shape, we designed the new one-component window chamber with a square compartment for holding cover slip (Figure 34). This would also benefit the stability of glass cover slip on the chamber, as a larger glue area can be applied between cover slip and the chamber ring. Double stitches of the two skin layers were applied during the installation of the chamber to secure the chamber. The final available viewing size was fixed to diameter of 23.5mm and can be reached by all sized objective lens freely.

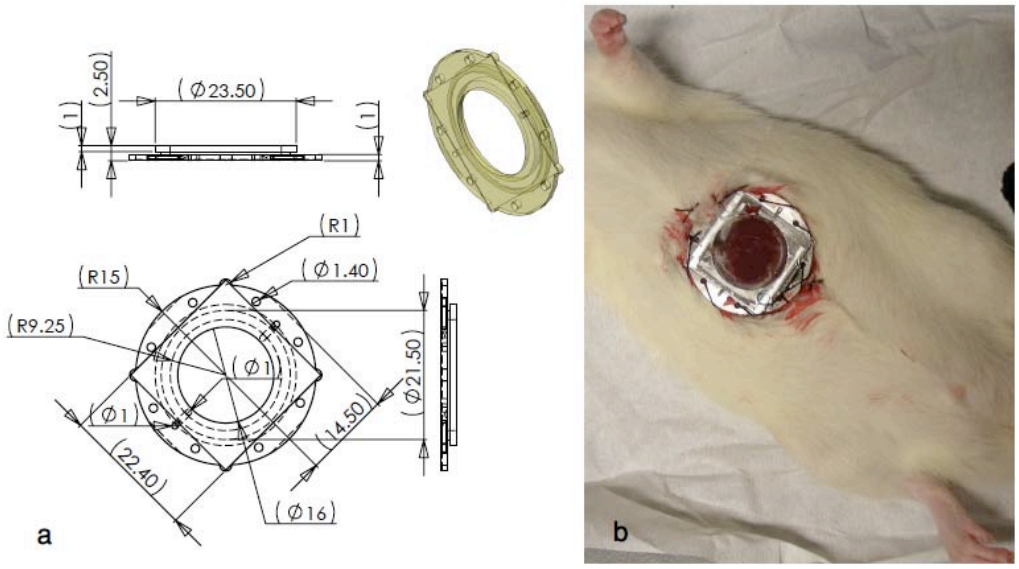

Figure 34. Window intravital chamber design and application on rats. (a) Design of the one component intravital chamber with square indentation on the surface for cover slip attachment. The dimensions were marked with millimeter. (b) Installation of titanium chamber on rat's abdomen, stitches and glues were employed to stabilize the chamber, lower left lobe liver was exposed.

6.3.2 Material for window intravital chamber cover slip

With the intension of building a live imaging animal model for fibrosis surface assessment, and the potential for cross-modality comparison with Magnetic Resonance Imaging (MRI), we researched on the alternative MRI artifact-free

materials to allow Apparent Diffusion Coefficient (ADCs) measurement at the same time with optical imaging for liver fibrosis. Polymer PET was suggested for this purpose due its biocompatibility [176] and its transparent property. Possessing similar susceptibility to soft tissue, PET has also been suggested to have no magnetic field interactions [177]. Its optical properties were further studied.

Autofluorescence signals were first tested with fluorescent microbeads. Signal scattering (Table 5) of fluorescent microbeads and images of fluorescent microbeads (Figure 35) under both glass cover slip and PET cover slip were compared. Signal scattering was estimated by: Scattering Ratio= $\frac{\text{sum of signal intensity in } 2.5\mu\text{m} \text{ diameter circular area with maximum signal}}{\text{the sum of total intensity around the bead}}$.

As indicated by the table, glass has much better signal intensity compared to PET, with much less scattering. This was also shown in the Figure 35. Using the same microbeads, microbeads signals under glass cover slip (Figure 35(a, d)) was much stronger than under PET cover slip (Figure 35(b, e)), with the beads' round shape easily identifiable. To improve the signal intensity, image set-up for optimal images under PET cover slip was employed by increasing the detector gain. Although signals were much stronger (Figure 35(c, f)) compared with earlier set-up, the scattering also increased at the same time, shown by the drop in ratio from 43.2% to 12% in Table 5.

Table 5. Scattering Ratio from beads under glass and PET cover clip.

	Ratio	SD
Glass	77.90%	0.019
PET - Same parameter with glass	43.20%	0.056
PET- optimized parameter for PET	12.00%	0.037

SD = Standard Deviation

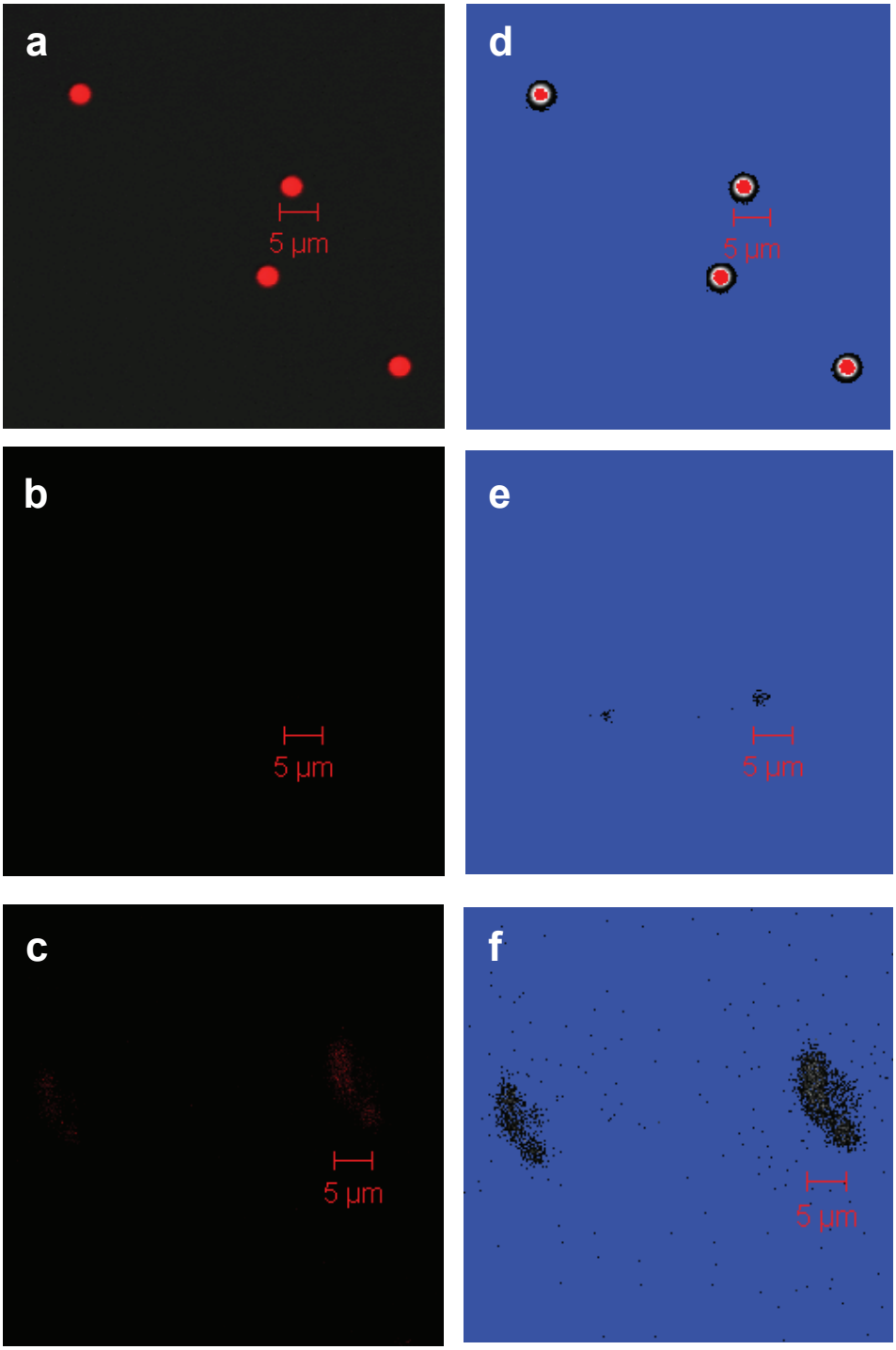

Figure 35. Fluorescent images of 100% microbeads under both glass and PET cover slips. Images of microbeads under glass cover slip (a) and under PET cover slip (b) with the same image set-up and parameters. Image of microbeads under PET cover slip with optimized parameter for PET. (d), (e) and (f) are the range indicator of the same image as (a), (b) and (c) respectively. Background was shown as blue, weak signal was shown as black, strong signal was shown as white and saturated signal was shown as red. Scale bar is 5µm.

Next, we tested the SHG signals from muscle tissues coming through both glass and TEP cover slips. For liver fibrosis assessment, SHG signals are very important, as they are the most important indicator for fibrosis occurrence shown in the earlier study. Under glass cover slip (Figure 36(a)), the SHG channel has high resolution and the muscle fiber striation with band width approximately 2μm can be identified clearly. Under the same detector gain, muscle tissue under PET (Figure 36(b)) had a weaker signal, although the muscle striation can still be seen. By optimizing the gain parameter in the microscope, the intensity of SHG signal increased and the striation can be easily spotted (Figure 36(c)). Based on the observation, SHG signals have a better presentation under the PET cover slips than the autofluorescence signals. However, the signal intensity is still much weaker than under glass cover slip.

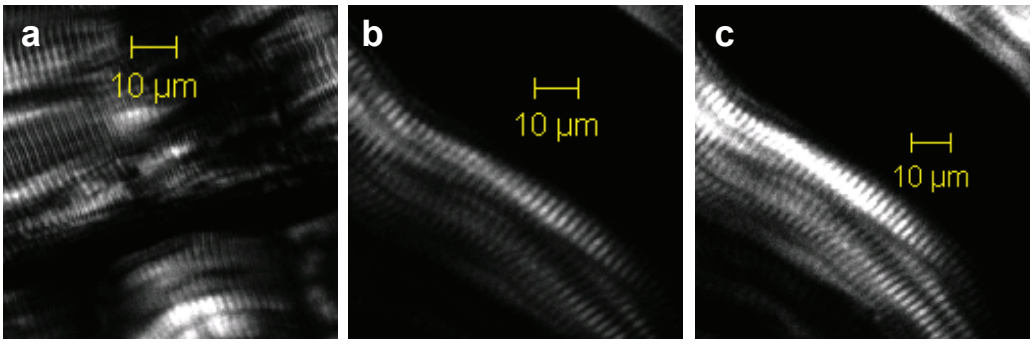

Figure 36. SHG images of muscle tissue striation under both glass and PET cover slips. (a) SHG signal under glass cover slip. (b) SHG signal under PET cover slip, with the same parameter as that under glass. (c) SHG signal under PET cover slip, with increased gain. Scale bar is 10μm.

To investigate the cellular level signal resolution under both glass and PET cover slips, stained cervical cancer cells were tested in both situations. The pDsRed labeled endoplasmic reticulum (ER) of HeLa cells was observed under different cover slips with Plan-Neofluar 40x lens. As shown in Figure

37(a), The ER can be distinguished in the cells under a glass cover slip. However, with the same imaging set-up, no cell can be observed under PET cover slip (image not shown). By increasing the detector gain of the microscope, the ER structure of the cells can be observed (Figure 37(b)), although the image was much more blurry compared with that under glass cover slip. A spot-like artifact with size of approximately 2μm diameter was also observed under PET cover slip (Figure 37(b) with arrow). It was suspected that due to the holes and chains configuration of PET polymer, the holes in PET might give rise to the dot artifact. This artifact would compromise the later fibrosis quantification, especially under live imaging, the artifact would be even more prominent.

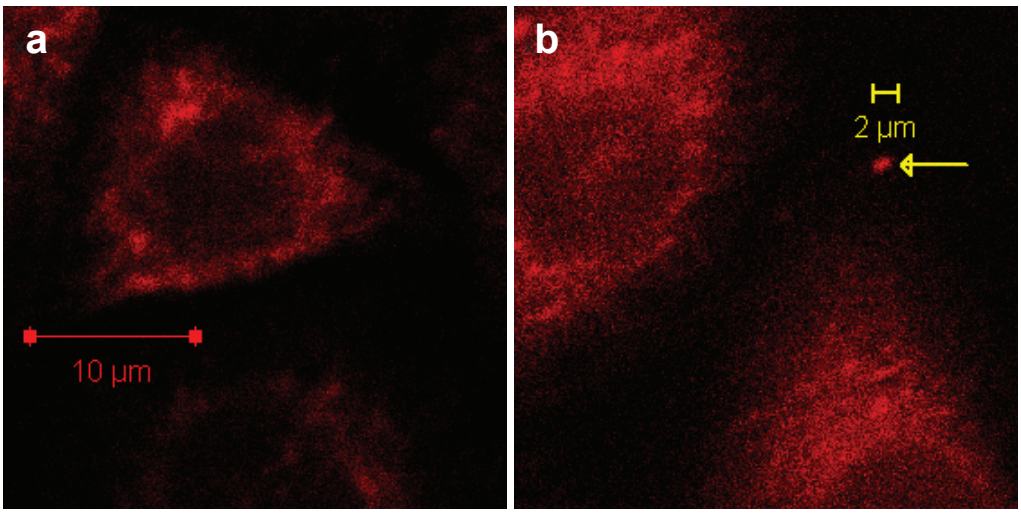

Figure 37. Imaging of cervical cancer cell with pDsRed labeled endoplasmic reticulum under both glass and PET cover slips. (a) Image taken under glass cover slip. (b) Image taken under PET cover slip with arrow pointing to the spot like artifact. Scale bar is 10μm in (a) and 2μm in (b).

Finally, the transmission spectrum of glass and PET was compared. As shown in Table 6, the transmission percentage of PET is on average about 10% lower than glass under all wavelengths tested. This loss of signal during imaging

would compromise the images taken from liver tissue, and possibly make it hard for feature extraction in both SHG and TPEF channels. With the weakening of signal from reflective imaging compared to transmission imaging, this loss of signal would exacerbate in liver surface assessment.

Table 6. Transmission percentage of glass and PET at specific wavelength

Applied signal and Wavelength (nm)	*Glass*		PET		Difference in Mean
	Mean	SD	Mean	SD	
Flurescence Green (500 – 550)	90.6%	0.047	79.6%	0.081	11.0%
Flurescence Red (550 – 630)	90.0%	0.056	79.0%	0.086	11.0%
SHG (440-460)	92.6%	0.033	81.2%	0.084	11.4%
SHG (890- 910)	92.5%	0.022	82.7%	0.084	9.8%

In conclusion, based on the comparison of glass and PET cover slip optical properties so far, we found it is to our benefit to stick with glass cover slip design. Since the optical property delivered by PET was sub-optimal, it would deteriorate the final purpose of liver surface fibrosis assessment. Therefore, the final intravital chamber was designed in one component with square glass cover slip as the viewing media.

6.3.3 Window intravital chamber installation on rats

After deciding on the one-component design with glass cover slip and titanium for the intravital chamber material, the whole imaging stage was redesigned in

stainless steel to hold the chamber and to fit on the LSM 510, Carl Zeiss microscope. As shown in Figure 38, the imaging stage was made of three components. The U-shape steel plate (Figure 38(a)) would secure the intravital chamber attached to the rat skin, and screwed tight to the ring holder. With them fastened together, the ring holder would be placed on steel stage (Figure em(b)), and be screwed tight from the front end of the steel stage. The fully assembled imaging stage was presented as in Figure em(c). It would be directly placed on the Carl Zeiss microscope to expose the middle part for imaging.

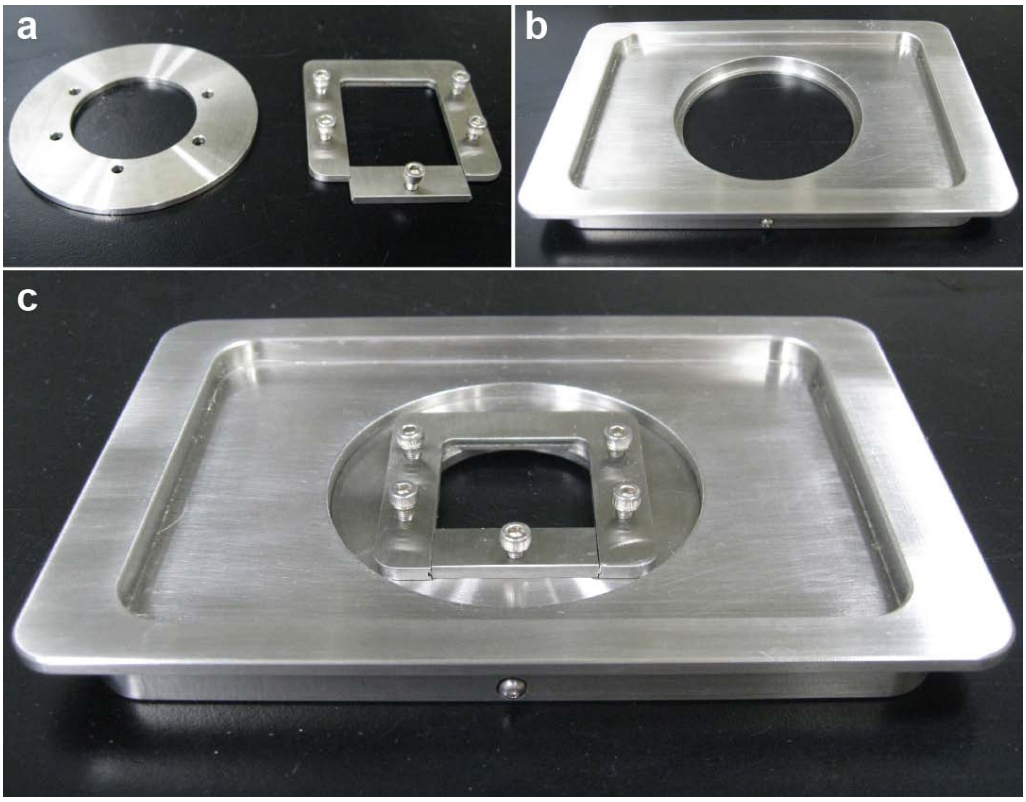

Figure 38. Imaging stage customized for window intravital chamber live imaging. Components designed to secure intravital chamber is shown in (a) with U-shape holding the chamber and screwed to the ring holder on the left. Steel stage (b) is used to secure the ring holder and the assembled stage is shown in (c).

To apply the window intravital chamber and to eventually put rat on imaging stage ready for live imaging, a few steps were taken. As described previously

in materials and methods, to optimize the liver exposure size for live imaging, lower left lobe of liver was targeted for exposure. The rat was put in a supine position after anesthesia on the operational stage. A small incision on the lower left abdomen was firstly made to exposure the area (Figure 39(a)), and then window intravital chamber with glass cover slip attached was double layer stitched to the open abdomen. Liver surface was exposed through glass cover slip. U-shape steel plate and ring holder were then screwed tightly to the intravital chamber (Figure 39(b)), and lastly placed on the imaging steel stage (Figure 39(d)). After fastening the ring holder to the imaging stage, the rat with the stage was placed in microscope for imaging.

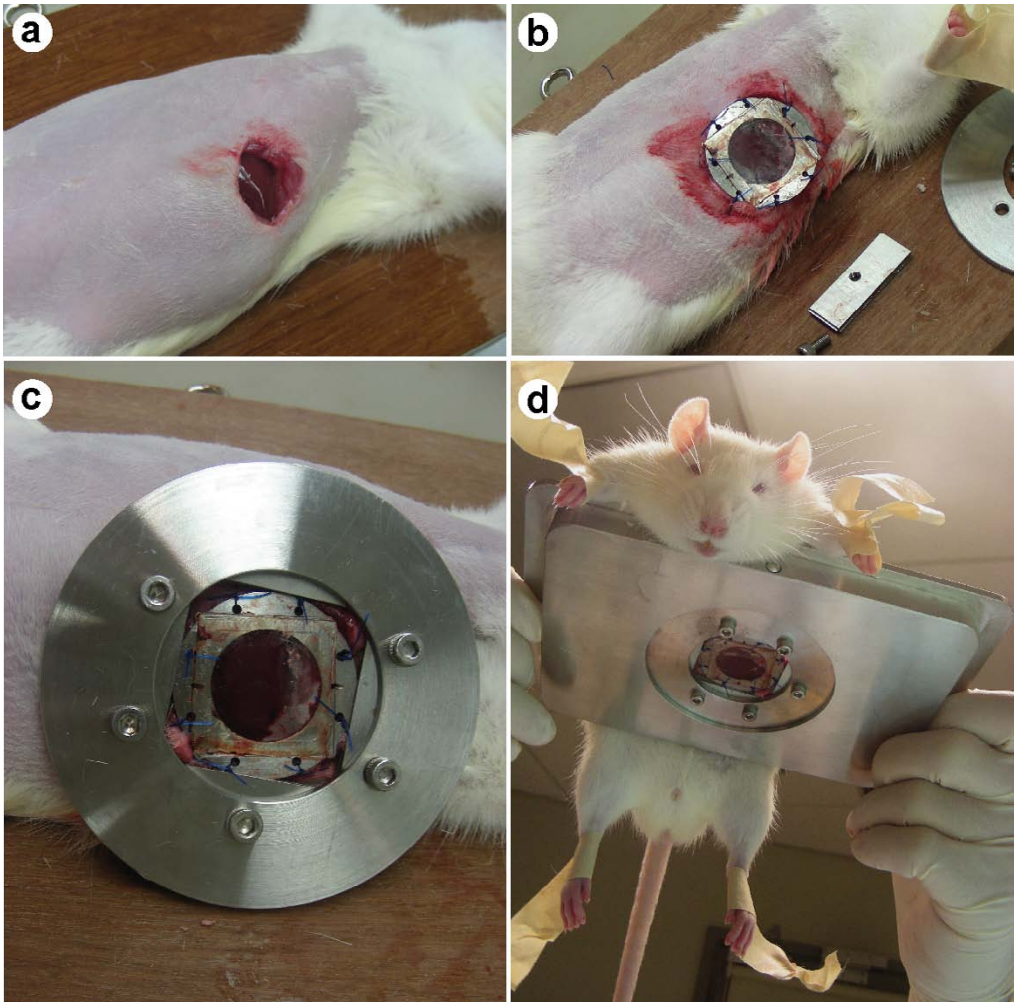

Figure 39. Accommodation of window intravital model rat on imaging stage. Liver was exposed (a) on the lower left abdomen, and then sutured to window intravital chamber (b). After tightly immobilized on U-shape plate and ring holder (c), rat with intravital chamber was placed on the imaging stage (d), ready for live imaging.

6.3.4 Live imaging of window model rat

Following the previous study of BDL rat fibrosis assessment, we proceeded with the intravital window model application on BDL rat model. After bile duct ligation operation was carried out, intravital window chambers were installed on rats' abdomen different weeks after the operation. However, from two to three weeks after bile duct ligation operation, ascitics in the peritoneal cavity began to accumulate in the operated rats, causing the difficulty in the

chamber installation. Meanwhile, the ascitics also created a gap between the chamber viewing window and the liver tissue. The mis-attachment eventually impaired the imaging quality of the liver tissue, making this live imaging model ineffective.

To solve this problem and to introduce a viable animal model for liver fibrosis live imaging, we proposed a liver toxicity model as apposed to bile duct proliferation model to induce liver fibrosis. Thioacetamide (TAA) induced liver fibrosis model was then established on rats as described in methods to incorporate into the live imaging project.

Liver fibrosis features of the toxicity model were first observed in fixed tissue reflective images, where liver surfaces of fixed samples of normal (Figure 40(a,c)) and fibrotic livers (Figure 40(b,d)) were compared. As shown in the figure, with the progression of liver fibrosis, capsule collagen in fibrotic liver (Figure 40(b)) increases drastically compared to normal liver (Figure 40(a)). Almost no collagen in sub-capsule region could be identified in normal liver (Figure 40(c)), while abundance of fibril collagen was present in fibrotic liver tissue (Figure 40(d)). The sub-capsule tissue structure of normal liver was tightly aligned and sinusoids were easily identifiable, while in the fibrotic liver, the alignment of hepatocytes were much loser and a loss of autofluorescence signal was observed, especially surrounding collagen proliferation area. This could due to the block of autofluorescence signals reflection from thick layer of capsule collagen in fibrotic tissue. With these observations in tissue imaging, live images were further generated and compared.

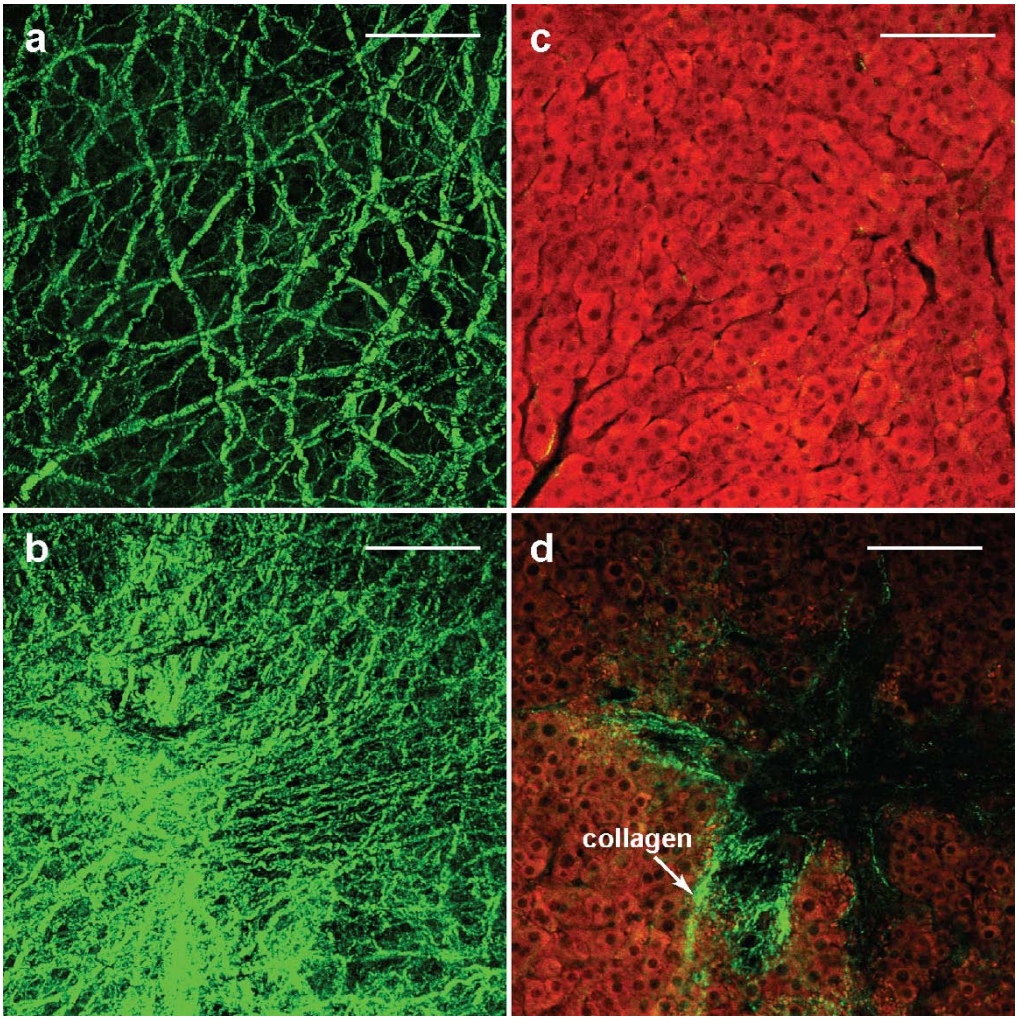

Figure 40. Surface scanning of TAA model liver tissues. Reflective SHG and TPEF images of liver surfaces were obtained from both normal (a,c) and fibrotic (b,d) liver tissues. 3D projection of capsule collagen of both normal (a) and fibrotic (b) liver surface were shown, and increase of collagen in fibrotic liver were evident. Sub-capsule region images were obtained respectively. Presence of significant amount of collagen and loss of tissue structure can be observed in fibrotic tissue (d) compared to normal liver (c). Scale bar is 100μm.

Rats of different weeks after TAA injection were installed with intravital window based imaging chamber for live imaging. Here, live imaging results of three time points and three different rats after fibrosis induction were shown. 3D projection of normal rat liver capsule (Figure 41(a)) and sub-capsule tissue image (Figure 41(b)) were compared with that from fibrotic livers both 10 weeks after TAA treatment (Figure 41(c) and Figure 41(d)) and 14 weeks after TAA treatment (Figure 41(e) and Figure 41(f)). An increase of capsule colla-

gen distribution on the liver surface was evident by the increasing amount and the intensity of SHG signals from collagen. The increasing presence of sub-capsule collagen (Figure 41 (d,e,f)) was also in agreement of fibrosis progression, even though the amount of collagen seen in live images were less thank in fixed tissue images. Meanwhile, with the increase of liver fibrosis, tissue structure in the sub-capsule region was getting less distinguishable, and signals from liver cells was much weaker. In very late stage of fibrosis or cirrhosis (Figure 41(f)), cellular structure was hardly identifiable compared to well aligned hepatocytes in normal healthy rat liver (Figure 41(d)). The loss of TPEF signals and the disruption of cellular structure in fibrotic liver could be caused by apoptosis and necrosis of hepatocytes, as they are the main source of autofluorescence in liver tissue. With the fibrosis progression, the hardening of liver could also put more pressure on the blood flow, which interrupted the signals of hepatocytes autofluorescence. The less and weaker SHG signal collected in live imaging (Figure 41(f)) compared to signals from fixed tissue (Figure 40(d)) could also be contributed to the interference of blood flow and animal breathing during live imaging.

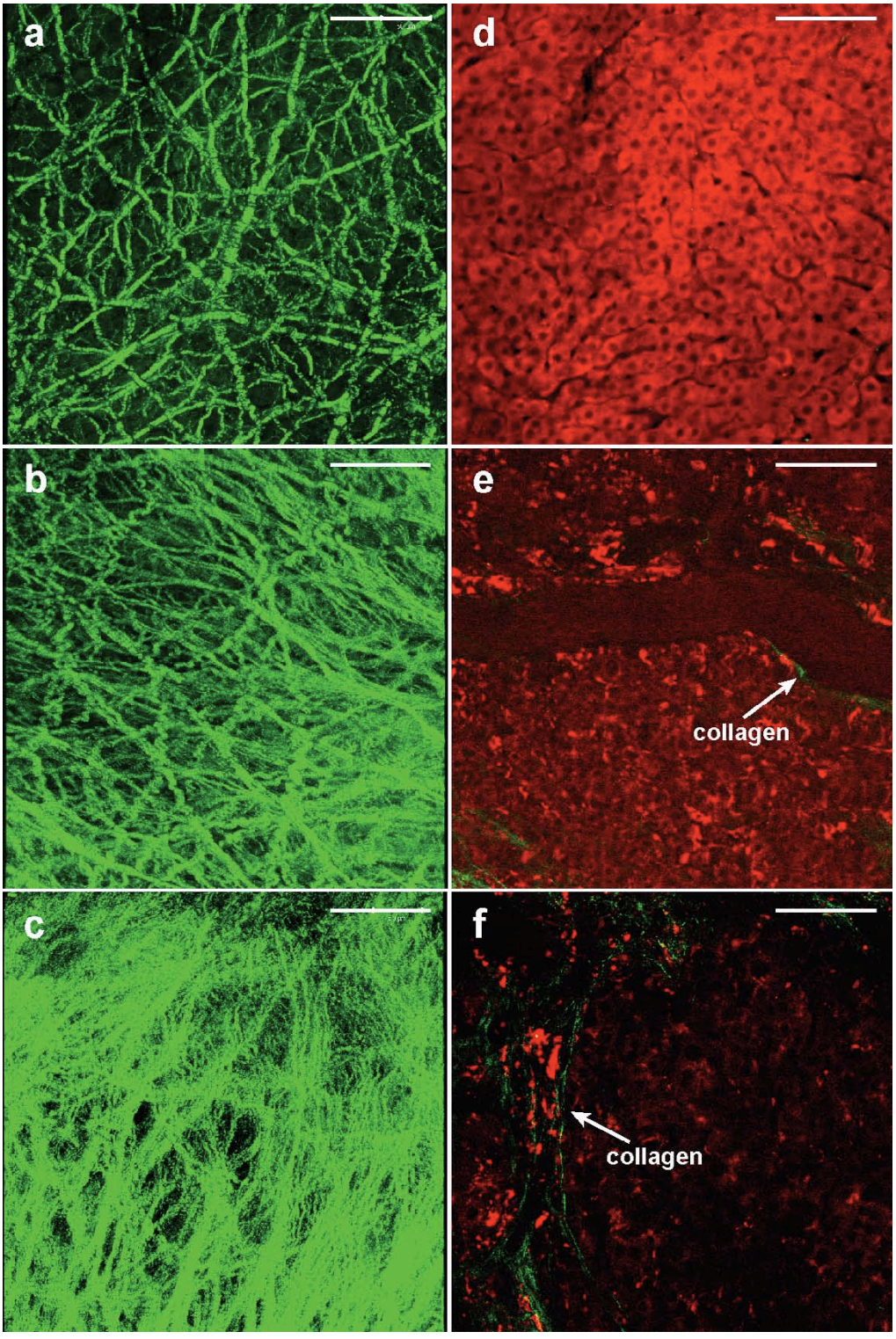

Figure 41. Live imaging of window model rats. Normal rat (a,d), rats of 10 weeks (b,e) and 14 weeks after TAA injection (c,f) were installed with intravital imaging chamber and placed on microscope for live imaging. 3D projections of capsule collagen (a,b,c) were recorded together with sub-capsule imaging (d,e,f) of both collagen and tissue. Increase of collagen distribution in both capsule and sub-capsule regions was evident by the increasing amount of SHG signals. Tissue structure was less aligned and signals were dropping with the increase of fibrosis. Scale bar is 100μm.

6.4 Conclusion

Based on the results from previous study that fibrosis distribution on liver surface is similar to that of the liver interior, we focused on the application of such discovery in live imaging in this chapter. Intravital imaging based liver chamber was designed and developed for live rat imaging purpose, and has been applied on both normal and fibrotic rats for *in vivo* liver fibrosis monitoring. Toxicity induced liver fibrosis model was developed as opposed to previously used Bile Duct Ligation model for the ease of chamber installation and imaging quality control. With the observation of live images, we discovered similar fibrosis features to what we observed in both transmission and reflective tissue imaging, including increase of capsule collagen distribution on liver surface, increase of sub-capsule fibril collagen deposition within the liver tissue and disruption of tissue structure with the fibrosis progression. With these features present in both animal models and the ability of detection of features in live imaging, we are currently able to monitor fibrosis based on this window animal model.

Chapter 7 Conclusion

This thesis documented the study of liver fibrosis using non-linear optics microscopy. Rat fibrosis models were established as animal study platform, and tissue level imaging was applied. To use non-linear optics methods to study liver fibrosis, images of unstained liver tissues taken were compared to conventional histological stained slice tissues. Four morphological features from digitized Second Harmonic Generation (SHG) / Two Photon Excitation Fluorescence (TPEF) images were extracted from tissues, and a standardized quantification system in liver fibrosis assessment was developed based on those features. After comparing with the conventional 'gold standard' histopathological scoring system, we demonstrated the feasibility of SHG/TPEF microscopes in monitoring liver fibrosis progression by the quantitative assessment we developed. The quantitative and standardization nature of the SHG/TPEF imaging modalities allows for future application in diagnosis and prognostication of disease complications and to assist biopsy reading by minimizing the intra- and interobserver discrepancies through standardized features quantification that is widely accepted by pathologist for staging. The non-staining requirement of such imaging methods also gave the potential for *in vivo* fibrosis assessment given its ability to extract cellular level features.

To achieve the goal of *in vivo* fibrosis assessment, we focused on the liver surface, where the imaging scanning would be performed. Due to the limited intrinsic penetration depth of SHG/TPEF imaging modalities in opaque liver tissue, liver surface features were studies and compared to the general features we extracted in interior liver. In Chapter 5, we discovered a strong correlation

between liver fibrosis progression on the anterior surface and the interior based on quantitative analysis of morphological features in both regions. By comparing with the conventional histopathological scoring system, we demonstrated the feasibility of monitoring liver fibrosis progression on the anterior liver surface. A uniform distribution of quantitative liver fibrotic features, such as total collagen distribution, bile duct proliferation and collagen in bile duct areas, was also discovered across two main lobes of the anterior liver surface, which gave us confidence to quantitatively monitor the progress of liver fibrosis on different lobe surfaces.

Following the discovery that fibrosis distribution on liver surface is similar to that of the liver interior, application of such discovery was explored in live imaging in Chapter 6. Intravital imaging based liver chamber was designed and developed for live rat imaging purpose, and has been applied on both normal and fibrotic rats for *in vivo* liver fibrosis monitoring. Toxicity-induced liver fibrosis model was developed as opposed to previously used Bile Duct Ligation model, for ease of chamber installation and imaging quality control. In live imaging of rat liver through window chamber, we discovered similar fibrosis features to those we observed in both transmission and reflective tissue imaging, including increase of capsule collagen distribution on liver surface, increase of sub-capsule fibril collagen deposition within the liver tissue and disruption of tissue structure with the fibrosis progression. With these features present in animal fibrosis models and the ability of detection of features in live imaging, we are currently able to monitor fibrosis based on this window animal model.

Chapter 8 Recommendations for Future Research

8.1 Antifibrotic drug effect monitoring using window based rat model

The search for antifibrotic drug has been ongoing, and pre-clinical trial on small animals has been an important step for drug discovery and development [178]. It is generally accepted that the use of sufficient numbers of animals (n=8-15 per group depending on the model) is critical to overcome the individual heterogeneity in fibrosis progression. However, it is costly to have a large sample size of animal and to sacrifice animals at different time points after the treatment would further complicate the analysis. Based on the intravital window based imaging chamber development in Chapter 6, and the future complete and extensive fibrosis assessment in different stages, a window based rat model could be used for live fibrosis staging and monitoring. A fully automated index for fibrosis could be generated based on the toxicity model fibrosis assessment, and applied in the antifibrotic effect monitoring. Using this model, drug effects study would be directly monitored on an individual rat, saving the cost of conducting different time points on different animal in each group. The results would also be better represented for drug effect study, and the effect on different individual can be studied in detail.

8.2 In vivo study of bone marrow derived Mesenchymal stem cells (MSCs)'s function in liver fibrosis

Bone marrow derived cells have been shown to contribute to fibrosis in different organs [179-181]. However, the function of Mesenchymal stem cells derived from bone marrow in liver fibrosis has been disputable, with some study

claiming it to have antifibrotic effect [182] while others claiming it to have contributed to the proliferation of hepatic stellate cells, which further exacerbate fibrosis [183]. To truly understand the effect of MSCs in the fibrotic liver, *in vivo* monitoring of fibrosis progression after the injection of BM or MSCs would be desirable. Using our window based rat model, liver fibrosis can be directly monitored on a continuous basis before and after the treatment, therefore, would help to solve the dispute of the arguments. Using contract enhanced dyes or genetic modified MSCs cells for the treatment, we can even locate the cells and trace the real-time cell migration and differentiation of MSCs in the fibrotic liver. This would provide strong argument for the real function of this cell type, and possibly direct future fibrosis treatment.

8.3 Virtual biopsy based on liver surface information extracted through non-linear optical endoscope

With the current development of non-linear endomicroscope [172, 184] with SHG and TPEF modalities build in, the application of surface scanning can be directly tested with the device. Instead of using a window-based rat model, rat liver fibrosis can be directly monitored using a non-linear endoscope for liver surface scanning. This would also allow access to larger liver area and assessment of different lobes. For repeated scanning, a device similar to a vascular shunt port can be implanted in rat abdomen for easy access and to relief the pain and damage to the skin. Cross modality comparison would also be made possible through this approach. This study would shed light on the future application of such device in clinical long-term follow up on liver fibrosis treatment to replace more invasive and damaging liver biopsy.

BIBLIOGRAPHY

1. Friedman, S.L., *Seminars in medicine of the Beth Israel Hospital, Boston. The cellular basis of hepatic fibrosis. Mechanisms and treatment strategies.* N Engl J Med, 1993. **328**(25): p. 1828-35.
2. Friedman, S.L., *Molecular regulation of hepatic fibrosis, an integrated cellular response to tissue injury.* J Biol Chem, 2000. **275**(4): p. 2247-50.
3. Afdhal, N.H. and D. Nunes, *Evaluation of liver fibrosis: a concise review.* Am J Gastroenterol, 2004. **99**(6): p. 1160-74.
4. Perrault, J., et al., *Liver biopsy: complications in 1000 inpatients and outpatients.* Gastroenterology, 1978. **74**(1): p. 103-6.
5. Torok, N.J., *Recent advances in the pathogenesis and diagnosis of liver fibrosis.* J Gastroenterol, 2008. **43**(5): p. 315-21.
6. Regev, A., et al., *Sampling error and intraobserver variation in liver biopsy in patients with chronic HCV infection.* Am J Gastroenterol, 2002. **97**(10): p. 2614-8.
7. Lee, H.S., et al., *Optical biopsy of liver fibrosis by use of multiphoton microscopy.* Opt Lett, 2004. **29**(22): p. 2614-6.
8. Williams, R.M., W.R. Zipfel, and W.W. Webb, *Interpreting second-harmonic generation images of collagen I fibrils.* Biophys J, 2005. **88**(2): p. 1377-86.
9. Denk, W., J.H. Strickler, and W.W. Webb, *Two-photon laser scanning fluorescence microscopy.* Science, 1990. **248**(4951): p. 73-6.
10. Masters, B.R. and M. Bohnke, *Three-dimensional confocal microscopy of the human cornea in vivo.* Ophthalmic Res, 2001. **33**(3): p. 125-35.
11. Rice, W.L., D.L. Kaplan, and I. Georgakoudi, *Quantitative biomarkers of stem cell differentiation based on intrinsic two-photon excited fluorescence.* J Biomed Opt, 2007. **12**(6): p. 060504.
12. Benyon, R.C. and M.J. Arthur, *Mechanisms of hepatic fibrosis.* J Pediatr Gastroenterol Nutr, 1998. **27**(1): p. 75-85.
13. Strupler, M., *Second harmonic imaging and scoring of collagen in fibrotic tissues.* OPTICS EXPRESS, 2007. **15**(7): p. 4054-4065.
14. Buschmann, R.J. and J.W. Ryoo, *Hepatic structural correlates of liver fibrosis: a morphometric analysis.* Exp Mol Pathol, 1989. **50**(1): p. 114-24.
15. *Human Biology and Health*1993: Englewood Cliffs, New Jersey, USA: Prentice Hall.
16. Lin, D.W., S. Johnson, and C.A. Hunt, *Modeling liver physiology: combining fractals, imaging and animation.* Conf Proc IEEE Eng Med Biol Soc, 2004. **5**: p. 3120-3.
17. Gines, P., et al., *Management of cirrhosis and ascites.* N Engl J Med, 2004. **350**(16): p. 1646-54.
18. Poynard, T., et al., *Natural history of HCV infection.* Baillieres Best Pract Res Clin Gastroenterol, 2000. **14**(2): p. 211-28.
19. Davis, G.L., et al., *Projecting future complications of chronic hepatitis C in the United States.* Liver Transpl, 2003. **9**(4): p. 331-8.

20. Griffiths, C., C. Rooney, and A. Brock, *Leading causes of death in England and Wales--how should we group causes?* Health Stat Q, 2005(28): p. 6-17.
21. Bosetti, C., et al., *Worldwide mortality from cirrhosis: an update to 2002.* J Hepatol, 2007. **46**(5): p. 827-39.
22. Berenguer, M., et al., *Severe recurrent hepatitis C after liver retransplantation for hepatitis C virus-related graft cirrhosis.* Liver Transpl, 2003. **9**(3): p. 228-35.
23. Bataller, R. and D.A. Brenner, *Liver fibrosis.* J Clin Invest, 2005. **115**(2): p. 209-18.
24. Friedman, S.L., *Liver fibrosis -- from bench to bedside.* J Hepatol, 2003. **38 Suppl 1**: p. S38-53.
25. Pinzani, M., *Liver fibrosis.* Springer Semin Immunopathol, 1999. **21**(4): p. 475-90.
26. Burt, A.D., *C. L. Oakley Lecture (1993). Cellular and molecular aspects of hepatic fibrosis.* J Pathol, 1993. **170**(2): p. 105-14.
27. Milani, S., et al., *Procollagen expression by nonparenchymal rat liver cells in experimental biliary fibrosis.* Gastroenterology, 1990. **98**(1): p. 175-84.
28. Marra, F., *Hepatic stellate cells and the regulation of liver inflammation.* J Hepatol, 1999. **31**(6): p. 1120-30.
29. Tuchweber, B., et al., *Proliferation and phenotypic modulation of portal fibroblasts in the early stages of cholestatic fibrosis in the rat.* Lab Invest, 1996. **74**(1): p. 265-78.
30. Knittel, T., et al., *Rat liver myofibroblasts and hepatic stellate cells: different cell populations of the fibroblast lineage with fibrogenic potential.* Gastroenterology, 1999. **117**(5): p. 1205-21.
31. Kisseleva, T., et al., *Bone marrow-derived fibrocytes participate in pathogenesis of liver fibrosis.* J Hepatol, 2006. **45**(3): p. 429-38.
32. Forbes, S.J., et al., *A significant proportion of myofibroblasts are of bone marrow origin in human liver fibrosis.* Gastroenterology, 2004. **126**(4): p. 955-63.
33. Zeisberg, M., et al., *Fibroblasts derive from hepatocytes in liver fibrosis via epithelial to mesenchymal transition.* J Biol Chem, 2007. **282**(32): p. 23337-47.
34. Lindquist, J.N., W.F. Marzluff, and B. Stefanovic, *Fibrogenesis. III. Posttranscriptional regulation of type I collagen.* Am J Physiol Gastrointest Liver Physiol, 2000. **279**(3): p. G471-6.
35. Yang, C., et al., *Liver fibrosis: insights into migration of hepatic stellate cells in response to extracellular matrix and growth factors.* Gastroenterology, 2003. **124**(1): p. 147-59.
36. Schuppan, D., et al., *Collagens in the liver extracellular matrix bind hepatocyte growth factor.* Gastroenterology, 1998. **114**(1): p. 139-52.
37. Schuppan, D., et al., *Matrix as a modulator of hepatic fibrogenesis.* Semin Liver Dis, 2001. **21**(3): p. 351-72.
38. Wells, R.G., *The role of matrix stiffness in regulating cell behavior.* Hepatology, 2008. **47**(4): p. 1394-400.
39. Burt, A.D., et al., *Ultrastructural localization of extracellular matrix proteins in liver biopsies using ultracryomicrotomy and immuno-gold labelling.* Histopathology, 1990. **16**(1): p. 53-8.

40. Hahn, E., et al., *Distribution of basement membrane proteins in normal and fibrotic human liver: collagen type IV, laminin, and fibronectin.* Gut, 1980. **21**(1): p. 63-71.
41. Rojkind, M., M.A. Giambrone, and L. Biempica, *Collagen types in normal and cirrhotic liver.* Gastroenterology, 1979. **76**(4): p. 710-9.
42. Seyer, J.M., E.T. Hutcheson, and A.H. Kang, *Collagen polymorphism in normal and cirrhotic human liver.* J Clin Invest, 1977. **59**(2): p. 241-8.
43. Tsukada, S., C.J. Parsons, and R.A. Rippe, *Mechanisms of liver fibrosis.* Clin Chim Acta, 2006. **364**(1-2): p. 33-60.
44. Goodman, Z.D., *Grading and staging systems for inflammation and fibrosis in chronic liver diseases.* J Hepatol, 2007. **47**(4): p. 598-607.
45. Bedossa, P. and T. Poynard, *An algorithm for the grading of activity in chronic hepatitis C. The METAVIR Cooperative Study Group.* Hepatology, 1996. **24**(2): p. 289-93.
46. Ishak, K., et al., *Histological grading and staging of chronic hepatitis.* J Hepatol, 1995. **22**(6): p. 696-9.
47. Thampanitchawong, P. and T. Piratvisuth, *Liver biopsy:complications and risk factors.* World J Gastroenterol, 1999. **5**(4): p. 301-304.
48. Poniachik, J., et al., *The role of laparoscopy in the diagnosis of cirrhosis.* Gastrointest Endosc, 1996. **43**(6): p. 568-71.
49. Pagliaro, L., et al., *Percutaneous blind biopsy versus laparoscopy with guided biopsy in diagnosis of cirrhosis. A prospective, randomized trial.* Dig Dis Sci, 1983. **28**(1): p. 39-43.
50. Maharaj, B., et al., *Sampling variability and its influence on the diagnostic yield of percutaneous needle biopsy of the liver.* Lancet, 1986. **1**(8480): p. 523-5.
51. Schlichting, P., B. Holund, and H. Poulsen, *Liver biopsy in chronic aggressive hepatitis. Diagnostic reproducibility in relation to size of specimen.* Scand J Gastroenterol, 1983. **18**(1): p. 27-32.
52. Holund, B., H. Poulsen, and P. Schlichting, *Reproducibility of liver biopsy diagnosis in relation to the size of the specimen.* Scand J Gastroenterol, 1980. **15**(3): p. 329-35.
53. Imbert-Bismut, F., et al., *Biochemical markers of liver fibrosis in patients with hepatitis C virus infection: a prospective study.* Lancet, 2001. **357**(9262): p. 1069-75.
54. Forns, X., et al., *Identification of chronic hepatitis C patients without hepatic fibrosis by a simple predictive model.* Hepatology, 2002. **36**(4 Pt 1): p. 986-92.
55. Fontana, R.J. and A.S. Lok, *Noninvasive monitoring of patients with chronic hepatitis C.* Hepatology, 2002. **36**(5 Suppl 1): p. S57-64.
56. Manning, D.S. and N.H. Afdhal, *Diagnosis and quantitation of fibrosis.* Gastroenterology, 2008. **134**(6): p. 1670-81.
57. Castera, L., et al., *Prospective comparison of transient elastography, Fibrotest, APRI, and liver biopsy for the assessment of fibrosis in chronic hepatitis C.* Gastroenterology, 2005. **128**(2): p. 343-50.
58. Sagir, A., et al., *Transient elastography is unreliable for detection of cirrhosis in patients with acute liver damage.* Hepatology, 2008. **47**(2): p. 592-5.

59. Solga, S.F., et al., *Hepatic 31P magnetic resonance spectroscopy: a hepatologist's user guide.* Liver Int, 2005. **25**(3): p. 490-500.
60. Yin, M., et al., *Assessment of hepatic fibrosis with magnetic resonance elastography.* Clin Gastroenterol Hepatol, 2007. **5**(10): p. 1207-1213 e2.
61. Bataller, R. and D.A. Brenner, *Hepatic stellate cells as a target for the treatment of liver fibrosis.* Semin Liver Dis, 2001. **21**(3): p. 437-51.
62. Masters, B.R. and P.T. So, *Antecedents of two-photon excitation laser scanning microscopy.* Microsc Res Tech, 2004. **63**(1): p. 3-11.
63. Guo, Y., et al., *Second-harmonic tomography of tissues.* Opt Lett, 1997. **22**(17): p. 1323-5.
64. Yelin, D. and Y. Silberberg, *Laser scanning third-harmonic-generation microscopy in biology.* Opt Express, 1999. **5**(8): p. 169-75.
65. Kano, H. and H.O. Hamaguchi, *Three-dimensional vibrational imaging of a microcrystalline J-aggregate using supercontinuum-based ultra-broadband multiplex coherent anti-stokes Raman scattering microscopy.* J Phys Chem B, 2006. **110**(7): p. 3120-6.
66. Freudiger, C.W., et al., *Label-free biomedical imaging with high sensitivity by stimulated Raman scattering microscopy.* Science, 2008. **322**(5909): p. 1857-61.
67. Göppert-Mayer, M., *Über Elementarake mit zwei Quantensprungen*, in *Ann. Phys. (Leipzig)*1931.
68. Garret, W.K.a.C.G.B., *Two-photon excitation in CaF2:Eu2+*. Phys. Rev. Lett., 1961. **7**(229).
69. P. T. C. So, C.Y.D.a.B.R.M., *Two-photon excitation fluorescence microscopy*. Vol. Chapter 11. 2003: CRC Press LLC.
70. So, B.R.M.a.P.T.C., *Handbook of biomedical nonlinear optical microscopy*. Vol. Chapter 6. 2008: Oxford University Press.
71. Centonze, V.E. and J.G. White, *Multiphoton excitation provides optical sections from deeper within scattering specimens than confocal imaging.* Biophys J, 1998. **75**(4): p. 2015-24.
72. Araya, R., K.B. Eisenthal, and R. Yuste, *Dendritic spines linearize the summation of excitatory potentials.* Proc Natl Acad Sci U S A, 2006. **103**(49): p. 18799-804.
73. Araya, R., et al., *The spine neck filters membrane potentials.* Proc Natl Acad Sci U S A, 2006. **103**(47): p. 17961-6.
74. Nishimura, N., et al., *Targeted insult to subsurface cortical blood vessels using ultrashort laser pulses: three models of stroke.* Nat Methods, 2006. **3**(2): p. 99-108.
75. Shakhar, G., et al., *Stable T cell-dendritic cell interactions precede the development of both tolerance and immunity in vivo.* Nat Immunol, 2005. **6**(7): p. 707-14.
76. Cavanagh, L.L., et al., *Activation of bone marrow-resident memory T cells by circulating, antigen-bearing dendritic cells.* Nat Immunol, 2005. **6**(10): p. 1029-37.
77. Boissonnas, A., et al., *In vivo imaging of cytotoxic T cell infiltration and elimination of a solid tumor.* J Exp Med, 2007. **204**(2): p. 345-56.
78. Brown, E.B., et al., *In vivo measurement of gene expression, angiogenesis and physiological function in tumors using multiphoton laser scanning microscopy.* Nat Med, 2001. **7**(7): p. 864-8.

79. Han, X., et al., *Second harmonic properties of tumor collagen: determining the structural relationship between reactive stroma and healthy stroma.* Opt. Express, 2008. **16**(3): p. 1846-1859.
80. Nemet, B.A., V. Nikolenko, and R. Yuste, *Second harmonic imaging of membrane potential of neurons with retinal.* J Biomed Opt, 2004. **9**(5): p. 873-81.
81. Theodossiou, T.A., et al., *Second harmonic generation confocal microscopy of collagen type I from rat tendon cryosections.* Biophys J, 2006. **91**(12): p. 4665-77.
82. Cox, G., et al., *3-dimensional imaging of collagen using second harmonic generation.* J Struct Biol, 2003. **141**(1): p. 53-62.
83. Rosenfeld, A., *Image Processing and Recognition*, in *Advances in Computers*, C.Y. Marshall, Editor 1979, Elsevier. p. 1-57.
84. Nakagawa, Y. and A. Rosenfeld, *Some experiments on variable thresholding.* Pattern Recognition, 1979. **11**(3): p. 191-204.
85. Yanowitz, S.D. and A.M. Bruckstein, *A new method for image segmentation.* Computer Vision, Graphics, and Image Processing, 1989. **46**(1): p. 82-95.
86. Otsu, N., *A threshold selection method from gray level histograms.* IEEE Trans. System, Man and Cybernetics, 1979. **9**: p. 62-66.
87. Ohlander, R., K. Price, and D.R. Reddy, *Picture segmentation using a recursive region splitting method.* Computer Graphics and Image Processing, 1978. **8**(3): p. 313-333.
88. Celenk, M., *A color clustering technique for image segmentation.* Computer Vision, Graphics, and Image Processing, 1990. **52**(2): p. 145-170.
89. Pal, N.R. and S.K. Pal, *A review on image segmentation techniques.* Pattern Recognition, 1993. **26**(9): p. 1277-1294.
90. Fu, K.S. and J.K. Mui, *A survey on image segmentation.* Pattern Recognition, 1981. **13**(1): p. 3-16.
91. Huntsherger, T.L., C.L. Jacobs, and R.L. Cannon, *Iterative fuzzy image segmentation.* Pattern Recognition, 1985. **18**(2): p. 131-138.
92. Bezdek, J.C., *Pattern Recognition with Fuzzy Objective Function Algorithms*1981: Kluwer Academic Publishers. 256.
93. Weigend, A.S., *Introduction to the theory of neural computation : John A. Hertz, Anders S. Krogh and Richard G. Palmer.* Artificial Intelligence, 1993. **62**(1): p. 93-111.
94. Manry, M.T., *Adaptive pattern recognition and neural networks: By Yoh-Han Pao, Addison-Wesley Publishing Company, Inc., New York: 1989, $40.76, 309 pp. ISBN 0-201-12584-6.* Neural Networks, 1991. **4**(1): p. 124-126.
95. Brunt, E.M., *Grading and staging the histopathological lesions of chronic hepatitis: the Knodell histology activity index and beyond.* Hepatology, 2000. **31**(1): p. 241-6.
96. Desmet, V.J., et al., *Classification of chronic hepatitis: diagnosis, grading and staging.* Hepatology, 1994. **19**(6): p. 1513-20.
97. Knodell, R.G., et al., *Formulation and application of a numerical scoring system for assessing histological activity in asymptomatic chronic active hepatitis.* Hepatology, 1981. **1**(5): p. 431-5.

98. *Intraobserver and interobserver variations in liver biopsy interpretation in patients with chronic hepatitis C. The French METAVIR Cooperative Study Group.* Hepatology, 1994. **20**(1 Pt 1): p. 15-20.
99. Bedossa, P., D. Dargere, and V. Paradis, *Sampling variability of liver fibrosis in chronic hepatitis C.* Hepatology, 2003. **38**(6): p. 1449-57.
100. Hui, A.Y., et al., *Quantitative assessment of fibrosis in liver biopsies from patients with chronic hepatitis B.* Liver Int, 2004. **24**(6): p. 611-8.
101. Masseroli, M., et al., *Automatic quantification of liver fibrosis: design and validation of a new image analysis method: comparison with semi-quantitative indexes of fibrosis.* J Hepatol, 2000. **32**(3): p. 453-64.
102. Soloway, R.D., et al., *Observer error and sampling variability tested in evaluation of hepatitis and cirrhosis by liver biopsy.* Am J Dig Dis, 1971. **16**(12): p. 1082-6.
103. Theodossi, A., et al., *Observer variation in assessment of liver biopsies including analysis by kappa statistics.* Gastroenterology, 1980. **79**(2): p. 232-41.
104. Westin, J., et al., *Interobserver study of liver histopathology using the Ishak score in patients with chronic hepatitis C virus infection.* Liver, 1999. **19**(3): p. 183-7.
105. Theodossi, A., et al., *Observer variation and discriminatory value of biopsy features in inflammatory bowel disease.* Gut, 1994. **35**(7): p. 961-8.
106. Gronbaek, K., et al., *Interobserver variation in interpretation of serial liver biopsies from patients with chronic hepatitis C.* J Viral Hepat, 2002. **9**(6): p. 443-9.
107. Gamal, M.D., et al., *Digital quantification of fibrosis in liver biopsy sections: Description of a new method by Photoshop software.* Journal of Gastroenterology and Hepatology, 2004. **19**(1): p. 78-85.
108. Wright, M., et al., *Quantitative versus morphological assessment of liver fibrosis: semi-quantitative scores are more robust than digital image fibrosis area estimation.* Liver Int, 2003. **23**(1): p. 28-34.
109. Friedenberg, M.A., et al., *Simplified method of hepatic fibrosis quantification: design of a new morphometric analysis application.* Liver Int, 2005. **25**(6): p. 1156-61.
110. Matalka, II, O.M. Al-Jarrah, and T.M. Manasrah, *Quantitative assessment of liver fibrosis: a novel automated image analysis method.* Liver Int, 2006. **26**(9): p. 1054-64.
111. Chen, M.H., et al., *Multiphoton autofluorescence and second-harmonic generation imaging of the tooth.* J Biomed Opt, 2007. **12**(6): p. 064018.
112. Gong, B., et al., *Nonlinear imaging study of extracellular matrix in chemical-induced, developmental dissecting aortic aneurysm: evidence for defective collagen type III.* Birth Defects Res A Clin Mol Teratol, 2008. **82**(1): p. 16-24.
113. Lyubovitsky, J.G., et al., *In situ multiphoton optical tomography of hair follicles in mice.* J Biomed Opt, 2007. **12**(4): p. 044003.
114. Gualda, E.J., et al., *In vivo imaging of cellular structures in Caenorhabditis elegans by combined TPEF, SHG and THG microscopy.* J Microsc, 2008. **229**(Pt 1): p. 141-50.

115. Odin, C., et al., *Orientation fields of nonlinear biological fibrils by second harmonic generation microscopy.* J Microsc, 2008. **229**(Pt 1): p. 32-8.
116. Teisseyre, T.Z., et al., *Nonlinear optical potentiometric dyes optimized for imaging with 1064-nm light.* J Biomed Opt, 2007. **12**(4): p. 044001.
117. Yasui, T., Y. Tohno, and T. Araki, *Characterization of collagen orientation in human dermis by two-dimensional second-harmonic-generation polarimetry.* J Biomed Opt, 2004. **9**(2): p. 259-64.
118. Sun, W., et al., *Nonlinear optical microscopy: use of second harmonic generation and two-photon microscopy for automated quantitative liver fibrosis studies.* J Biomed Opt, 2008. **13**(6): p. 064010.
119. Gorrell, M.D., et al., *Intrahepatic expression of collagen and fibroblast activation protein (FAP) in hepatitis C virus infection.* Adv Exp Med Biol, 2003. **524**: p. 235-43.
120. van Eeden, F.J., et al., *Developmental mutant screens in the zebrafish.* Methods Cell Biol, 1999. **60**: p. 21-41.
121. PJ, M., *Trichrome stainings and their preliminary techniques.* J Tech Met., 1929(12:75).
122. Junqueira, L.C., G. Bignolas, and R.R. Brentani, *Picrosirius staining plus polarization microscopy, a specific method for collagen detection in tissue sections.* Histochem J, 1979. **11**(4): p. 447-55.
123. Puchtler, H., F.S. Waldrop, and L.S. Valentine, *Polarization microscopic studies of connective tissue stained with picro-sirius red FBA.* Beitr Pathol, 1973. **150**(2): p. 174-87.
124. Ruwart, M.J., et al., *The integrated value of serum procollagen III peptide over time predicts hepatic hydroxyproline content and stainable collagen in a model of dietary cirrhosis in the rat.* Hepatology, 1989. **10**(5): p. 801-6.
125. Lloyd, S.P., *Least-Squares Quantization in Pcm.* Ieee Transactions on Information Theory, 1982. **28**(2): p. 129-137.
126. Dempster, A.P., N.M. Laird, and D.B. Rubin, *MAXIMUM LIKELIHOOD FROM INCOMPLETE DATA VIA EM ALGORITHM.* Journal of the Royal Statistical Society Series B-Methodological, 1977. **39**(1): p. 1-38.
127. Wang, P.H., *PATTERN-RECOGNITION WITH FUZZY OBJECTIVE FUNCTION ALGORITHMS - BEZDEK,JC.* Siam Review, 1983. **25**(3): p. 442-442.
128. Driever, W., et al., *A genetic screen for mutations affecting embryogenesis in zebrafish.* Development, 1996. **123**: p. 37-46.
129. Haffter, P., et al., *The identification of genes with unique and essential functions in the development of the zebrafish, Danio rerio.* Development, 1996. **123**: p. 1-36.
130. Colbert, T., et al., *High-throughput screening for induced point mutations.* Plant Physiol, 2001. **126**(2): p. 480-4.
131. Cheng, W., et al., *HNF factors form a network to regulate liver-enriched genes in zebrafish.* Dev Biol, 2006. **294**(2): p. 482-96.
132. Lokker, N.A., et al., *Structure-function analysis of hepatocyte growth factor: identification of variants that lack mitogenic activity yet retain high affinity receptor binding.* EMBO J, 1992. **11**(7): p. 2503-10.

133. Berezikov, E., R.H. Plasterk, and E. Cuppen, *GENOTRACE: cDNA-based local GENOme assembly from TRACE archives.* Bioinformatics, 2002. **18**(10): p. 1396-7.
134. Wienholds, E., et al., *Target-selected inactivation of the zebrafish rag1 gene.* Science, 2002. **297**(5578): p. 99-102.
135. Cuppen, E., et al., *Efficient target-selected mutagenesis in Caenorhabditis elegans: toward a knockout for every gene.* Genome Res, 2007. **17**(5): p. 649-58.
136. Ezure, T., et al., *The development and compensation of biliary cirrhosis in interleukin-6-deficient mice.* Am J Pathol, 2000. **156**(5): p. 1627-39.
137. Lunz, J.G., 3rd, et al., *Replicative senescence of biliary epithelial cells precedes bile duct loss in chronic liver allograft rejection: increased expression of p21(WAF1/Cip1) as a disease marker and the influence of immunosuppressive drugs.* Am J Pathol, 2001. **158**(4): p. 1379-90.
138. Locke, G.R., 3rd, et al., *Time course of histological progression in primary biliary cirrhosis.* Hepatology, 1996. **23**(1): p. 52-6.
139. Gilsanz Garcia, V., *[Primary biliary cirrhosis].* An R Acad Nac Med (Madr), 1990. **107**(2): p. 387-408.
140. Otte, J.B., et al., *Sequential treatment of biliary atresia with Kasai portoenterostomy and liver transplantation: a review.* Hepatology, 1994. **20**(1 Pt 2): p. 41S-48S.
141. Balistreri, W.F., et al., *Biliary atresia: current concepts and research directions. Summary of a symposium.* Hepatology, 1996. **23**(6): p. 1682-92.
142. Boigk, G., et al., *Silymarin retards collagen accumulation in early and advanced biliary fibrosis secondary to complete bile duct obliteration in rats.* Hepatology, 1997. **26**(3): p. 643-9.
143. Tretheway, D., et al., *Should trichrome stain be used on all post-liver transplant biopsies with hepatitis C virus infection to estimate the fibrosis score?* Liver Transpl, 2008. **14**(5): p. 695-700.
144. Dixon, J.B., et al., *Nonalcoholic fatty liver disease: Improvement in liver histological analysis with weight loss.* Hepatology, 2004. **39**(6): p. 1647-54.
145. Farci, P., et al., *Long-term benefit of interferon alpha therapy of chronic hepatitis D: regression of advanced hepatic fibrosis.* Gastroenterology, 2004. **126**(7): p. 1740-9.
146. Fowell, A.J. and J.P. Iredale, *Emerging therapies for liver fibrosis.* Dig Dis, 2006. **24**(1-2): p. 174-83.
147. Friedman, S.L. and M.B. Bansal, *Reversal of hepatic fibrosis -- fact or fantasy?* Hepatology, 2006. **43**(2 Suppl 1): p. S82-8.
148. Arthur, M.J., *Reversibility of liver fibrosis and cirrhosis following treatment for hepatitis C.* Gastroenterology, 2002. **122**(5): p. 1525-8.
149. Assy, N. and G.Y. Minuk, *Serum aspartate but not alanine aminotransferase levels help to predict the histological features of chronic hepatitis C viral infections in adults.* Am J Gastroenterol, 2000. **95**(6): p. 1545-50.
150. Anderson, F.H., et al., *An assessment of the clinical utility of serum ALT and AST in chronic hepatitis C.* Hepatol Res, 2000. **18**(1): p. 63-71.

151. Wai, C.T., et al., *A simple noninvasive index can predict both significant fibrosis and cirrhosis in patients with chronic hepatitis C.* Hepatology, 2003. **38**(2): p. 518-26.
152. Chrysanthos, N.V., et al., *Aspartate aminotransferase to platelet ratio index for fibrosis evaluation in chronic viral hepatitis.* Eur J Gastroenterol Hepatol, 2006. **18**(4): p. 389-96.
153. Shaheen, A.A. and R.P. Myers, *Diagnostic accuracy of the aspartate aminotransferase-to-platelet ratio index for the prediction of hepatitis C-related fibrosis: a systematic review.* Hepatology, 2007. **46**(3): p. 912-21.
154. Walsh, K.M., et al., *Basement membrane peptides as markers of liver disease in chronic hepatitis C.* J Hepatol, 2000. **32**(2): p. 325-30.
155. Kanzler, S., et al., *Prediction of progressive liver fibrosis in hepatitis C infection by serum and tissue levels of transforming growth factor-beta.* J Viral Hepat, 2001. **8**(6): p. 430-7.
156. George, D.K., et al., *Elevated serum type IV collagen: a sensitive indicator of the presence of cirrhosis in haemochromatosis.* J Hepatol, 1999. **31**(1): p. 47-52.
157. Fabris, P., et al., *Fibrogenesis serum markers in patients with chronic hepatitis C treated with alpha-IFN.* J Gastroenterol, 1999. **34**(3): p. 345-50.
158. Larrousse, M., et al., *Noninvasive diagnosis of hepatic fibrosis in HIV/HCV-coinfected patients.* J Acquir Immune Defic Syndr, 2007. **46**(3): p. 304-11.
159. McHutchison, J.G., et al., *Measurement of serum hyaluronic acid in patients with chronic hepatitis C and its relationship to liver histology. Consensus Interferon Study Group.* J Gastroenterol Hepatol, 2000. **15**(8): p. 945-51.
160. Trinchet, J.C., *Clinical use of serum markers of fibrosis in chronic hepatitis.* J Hepatol, 1995. **22**(2 Suppl): p. 89-95.
161. Thabut, D., et al., *Noninvasive prediction of fibrosis in patients with chronic hepatitis C.* Hepatology, 2003. **37**(5): p. 1220-1; author reply 1221.
162. Aube, C., et al., *Ultrasonographic diagnosis of hepatic fibrosis or cirrhosis.* J Hepatol, 1999. **30**(3): p. 472-8.
163. Fraquelli, M., et al., *Reproducibility of transient elastography in the evaluation of liver fibrosis in patients with chronic liver disease.* Gut, 2007. **56**(7): p. 968-73.
164. Salameh, N., et al., *Hepatic viscoelastic parameters measured with MR elastography: correlations with quantitative analysis of liver fibrosis in the rat.* J Magn Reson Imaging, 2007. **26**(4): p. 956-62.
165. Jalan, R., et al., *LAPAROSCOPY AND HISTOLOGY IN THE DIAGNOSIS OF CHRONIC LIVER-DISEASE.* Qjm-Monthly Journal of the Association of Physicians, 1995. **88**(8): p. 559-564.
166. Poniachik, J., et al., *The role of laparoscopy in the diagnosis of cirrhosis.* Gastrointestinal Endoscopy, 1996. **43**(6): p. 568-571.
167. Lin, S.-J., et al., *Evaluating cutaneous photoaging by use of multiphoton fluorescence and second-harmonic generation microscopy.* Opt. Lett., 2005. **30**(17): p. 2275-2277.

168. Teng, S.W., et al., *Multiphoton fluorescence and second-harmonic-generation microscopy for imaging structural alterations in corneal scar tissue in penetrating full-thickness wound.* Arch Ophthalmol, 2007. **125**(7): p. 977-8.
169. Tai, D.C., et al., *Fibro-C-Index: comprehensive, morphology-based quantification of liver fibrosis using second harmonic generation and two-photon microscopy.* J Biomed Opt, 2009. **14**(4): p. 044013.
170. Canny, J., *A COMPUTATIONAL APPROACH TO EDGE-DETECTION.* Ieee Transactions on Pattern Analysis and Machine Intelligence, 1986. **8**(6): p. 679-698.
171. Zipfel, W.R., et al., *Live tissue intrinsic emission microscopy using multiphoton-excited native fluorescence and second harmonic generation.* Proceedings of the National Academy of Sciences of the United States of America, 2003. **100**(12): p. 7075-7080.
172. Bao, H., et al., *Second harmonic generation imaging via nonlinear endomicroscopy.* Opt Express, 2009. **18**(2): p. 1255-60.
173. Ryoo, J.W. and R.J. Buschmann, *Comparison of intralobar non-parenchyma, subcapsular non-parenchyma, and liver capsule thickness.* J Clin Pathol, 1989. **42**(7): p. 740-4.
174. Buckley, I.K. and J. Semkiw, *A high frequency pulse generator for injuring tissue within the Sandison-Clark rabbit ear chamber.* Aust J Exp Biol Med Sci, 1959. **37**: p. 593-9.
175. Liu, Y., et al., *Visualization of hepatobiliary excretory function by intravital multiphoton microscopy.* J Biomed Opt, 2007. **12**(1): p. 014014.
176. Seitz, H., et al., *Biocompatibility of polyethylene terephthalate (Trevira hochfest) augmentation device in repair of the anterior cruciate ligament.* Biomaterials, 1998. **19**(1-3): p. 189-96.
177. Shellock, F.G., *Biomedical implants and devices: assessment of magnetic field interactions with a 3.0-Tesla MR system.* J Magn Reson Imaging, 2002. **16**(6): p. 721-32.
178. Popov, Y. and D. Schuppan, *Targeting liver fibrosis: strategies for development and validation of antifibrotic therapies.* Hepatology, 2009. **50**(4): p. 1294-306.
179. Lama, V.N. and S.H. Phan, *The extrapulmonary origin of fibroblasts: stem/progenitor cells and beyond.* Proc Am Thorac Soc, 2006. **3**(4): p. 373-6.
180. Hinz, B., et al., *The myofibroblast: one function, multiple origins.* Am J Pathol, 2007. **170**(6): p. 1807-16.
181. Phan, S.H., *The myofibroblast in pulmonary fibrosis.* Chest, 2002. **122**(6 Suppl): p. 286S-289S.
182. Oyagi, S., et al., *Therapeutic effect of transplanting HGF-treated bone marrow mesenchymal cells into CCl4-injured rats.* J Hepatol, 2006. **44**(4): p. 742-8.
183. Parekkadan, B., et al., *Immunomodulation of activated hepatic stellate cells by mesenchymal stem cells.* Biochem Biophys Res Commun, 2007. **363**(2): p. 247-52.
184. Wu, Y., et al., *Scanning all-fiber-optic endomicroscopy system for 3D nonlinear optical imaging of biological tissues.* Opt Express, 2009. **17**(10): p. 7907-15.

LIST OF PUBLICATIONS

Yuting He, Chiang Huen Kang, Shuoyu Xu, Xiaoye Tuo, Scott Trasti, Dean C. S. Tai, Anju Mythreyi Raja, Qiwen Peng, Peter T. C. So, Jagath C. Rajapakse, Roy Welsch and Hanry Yu, *Toward surface quantification of liver fibrosis progression*, J. Biomed. Opt. 15, 056007 (Sep 24, 2010); doi:10.1117/1.3490414

PATENT

Yuting He, Shuoyu Xu, Dean C.S. Tai, Hanry Yu *Instantaneous Virtual Biopsy for Liver Fibrosis Staging using Second Harmonic Generation Microscopy.*
Application No.: 61/319,673
Filing date: 31 March 2010

Yuting He, Shuoyu Xu, Dean C.S. Tai, Hanry Yu *A Method and System for Determining a Stage of Fibrosis in a Liver*
Application No.: PCT/SG2011/000133
Filing Date: 31 March 2011